DYNAMIC INTERACION OF VEHICLE AND BRIDGE SUBJECTED TO PRESTRESS FORCE LOSS AND FOUNDATION SETTLEMENT

A Dissertation
Submitted to the Graduate Faculty
of the
North Dakota State University
of Agriculture and Applied Science

By

Hai Zhong

In Partial Fulfillment of the Requirements
for the Degree of
DOCTOR OF PHILOSOPHY

Major Department:
Civil and Environmental Engineering

May 2016

Fargo, North Dakota

North Dakota State University
Graduate School

Title

DYNAMIC INTERACION OF VEHICLE AND BRIDGE SUBJECTED TO PRESTRESS FORCE LOSS AND FOUNDATION SETTLEMENT

By

Hai Zhong

The Supervisory Committee certifies that this ***disquisition*** complies with North Dakota State University's regulations and meets the accepted standards for the degree of

DOCTOR OF PHILOSOPHY

SUPERVISORY COMMITTEE:

Dr. Mijia Yang
Chair

Dr. Sivapalan Gajan

Dr. Ying Huang

Dr. Ghodrat Karami

Dr. Xiangqing (Annie) Tangpong

Approved:

May 24th, 2016 — Date

Dr. Dinesh Katti — Department Chair

ABSTRACT

Plenty of bridges in U.S. are suffering from prestress force loss and foundation settlements. The loss of prestress force in bridge load-carrying members such as girders may lead to the malfunction and even failure of the prestressed bridges that comprises more than 55% of all new and replaced bridges built in US between the year 2000 and 2012. Settlement of foundations supporting the bridge piers and abutments impairs the superstructure integrity and serviceability of the bridge, or even collapses the bridge if the settlement is over a certain limit.

In present study, the dynamic interaction between vehicles and the bridges subjected to prestress force loss and foundation settlement has been investigated. Based on modal superposition technique and principal of virtual works, new bridge-vehicle interaction models have been created to take the effects of prestress and foundation settlement on dynamic bridge and vehicle responses into account. With the developed models, numerical simulations have been performed to show that the prestress force makes the distribution of impact factors along the bridge unbalanced and the existence of foundation settlement may couple with road surface roughness of the bridge deck to possess an aggregated overall effect amplifying the bridge responses. In general, the vehicle responses are vulnerable to the prestress force loss and foundation settlement, which harms the riding comfort of passengers.

The existed direct and indirect methods used for prestress loss identification are all based on the measurement collected from sensors deployed on the outside or inside of the bridge, which is not only costly but also inconvenient. The current study proposes to detect the prestress force loss of the bridge through the analysis of vehicle responses. Through simulations, it is found that light, low-frequency vehicles moving at low speeds have a better performance in detecting the bridge prestress loss than the heavy, high-frequency vehicles with high speeds. The

advantage of the proposed method is that it only needs a few sensors installed on the vehicle, and works without interrupting the ongoing traffic, which is efficient and cost-effective.

ACKNOWLEDGEMENTS

First and foremost, I would like to express my sincere gratitude and appreciation to my advisor, Dr. Mijia Yang, for his continuous support and guidance during my study at NDSU. His invaluable advice and encouragement make the completion of the dissertation work possible. Not only the knowledge have I learned from him, but also the way of independent thinking and research, which will benefit my entire life. I also want to thank all the committee members, Dr. Sivapalan Gajan, Dr. Ying Huang, Dr. Ghodrat Karami and Dr. Xiangqing Tangpong, for their suggestion and help during the dissertation research. Thanks to Department of Civil and Environmental Engineering, North Dakota State University, the staff and all my friends. Last, but not the least, I would like to thank my parents, sisters and all the other family members for their unwavering support and love.

TABLE OF CONTENTS

LIST OF TABLES

LIST OF FIGURES

CHAPTER 1. INTRODUCTION

This chapter provides a general introduction to the prestress force loss and foundation settlement of bridges, as well as summary of current status on the bridge vehicle interaction analysis. Both prestress loss and foundation settlement lead to the change of bridge profile and thus affect the interaction between the vehicles and bridge, which is the subject of the dissertation. Statement of the problem, research objectives, and organization of this dissertation are also presented.

1.1. Prestressed Bridge and Its Prestress Loss

Prestressed bridges have prestressed concrete beams or girders as their main load-carrying members. Concrete is weak in tension and strong in compression. The basic principal behind prestressed concrete is to introduce the compressive stress in advance at the part of concrete that would be subjected to tension under the external or service loads. In other words, the pre-applied compressive stress is employed to balance or counteract the tensile stress induced by external loads during service, which avoids the tension cracks in concrete and thus significantly improves its serviceability, as shown in Fig. 1.1.

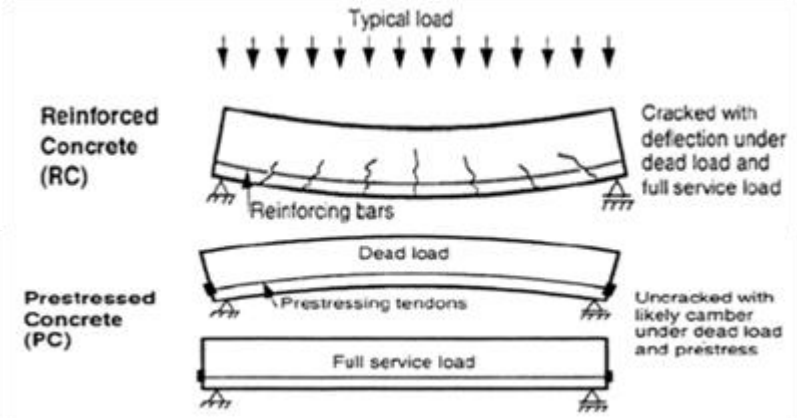

Fig. 1.1. Comparison of reinforced concrete and prestressed concrete

Prestressing can be implemented through the tension of high strength steel tendons before or after the concrete is cast, which produces the so-called ‘pre-tensioned’ and ‘post-tensioned’ concrete. In addition, based on the bonding between the concrete and prestressing tendons, post-tensioned concrete can be categorized into ‘bonded’ or ‘unbonded’.

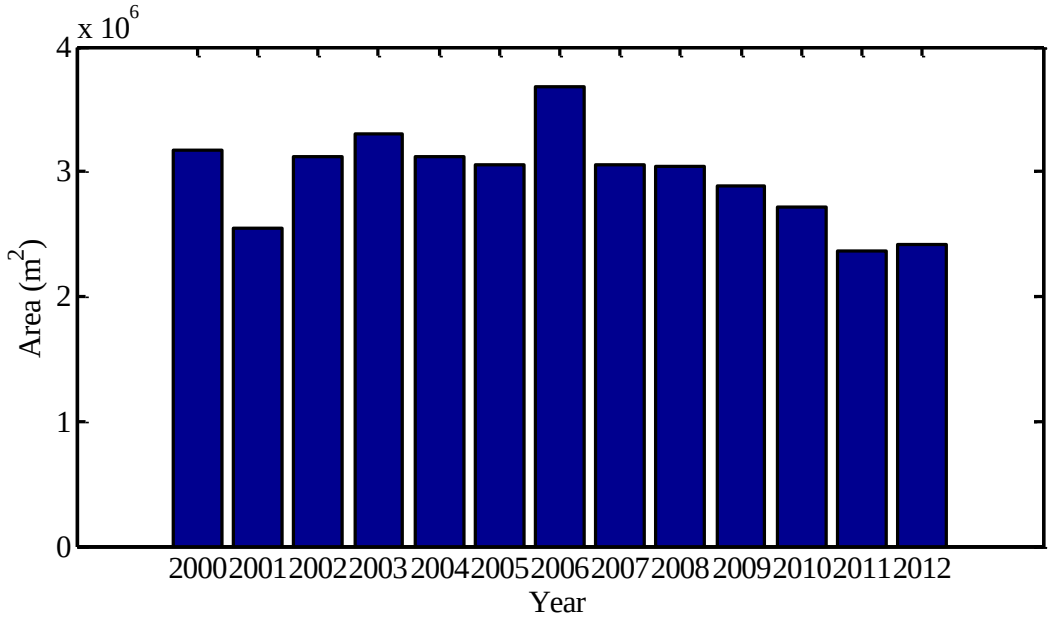

Fig. 1.2. Area of annual new and replaced PSC bridges in US (m^2) [1]

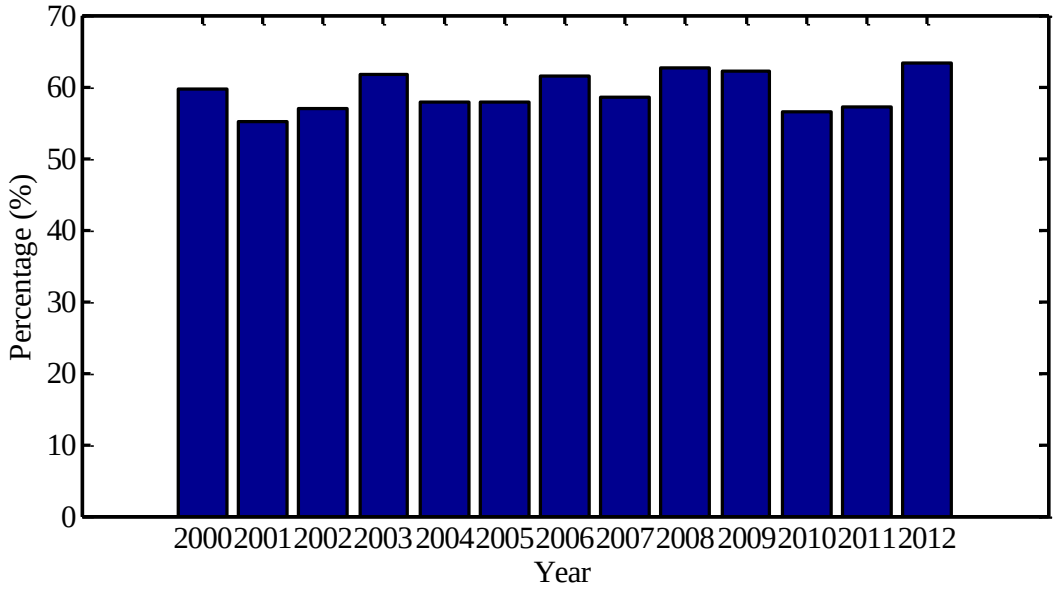

Fig. 1.3. Percentage of annual new and replaced PSC bridges in US [1]

It is not surprising to see the popularity of prestressed concrete in the construction of bridges in recent decades considering its high strength, stiffness and crack resistance. Based on the data from US Department of Transportation [1], from the year 2000 to 2012, each year more than 2 million square meters of prestressed concrete (PSC) bridges were built in US and they took up above 55% of all the new and replaced bridges, which are shown in Fig. 1.2 and Fig. 1.3 respectively. Therefore, it is extremely important and necessary to study the dynamic interaction between prestressed bridges and vehicles for better and safer bridge design and riders' comfort.

During service, loss of prestress force inevitably happens on prestressed bridges, either immediate or time dependent, as can be seen in Fig. 1.4. The reason for that can be the elastic shortening or relaxation of prestressing steel tendons, creep or shrinkage of concrete, friction between the tendons and surrounding concrete, and the slip of prestressing tendon anchorage. Prestress force is essential to a prestressed bridge and its loss severely impairs the capacity and serviceability of the bridge.

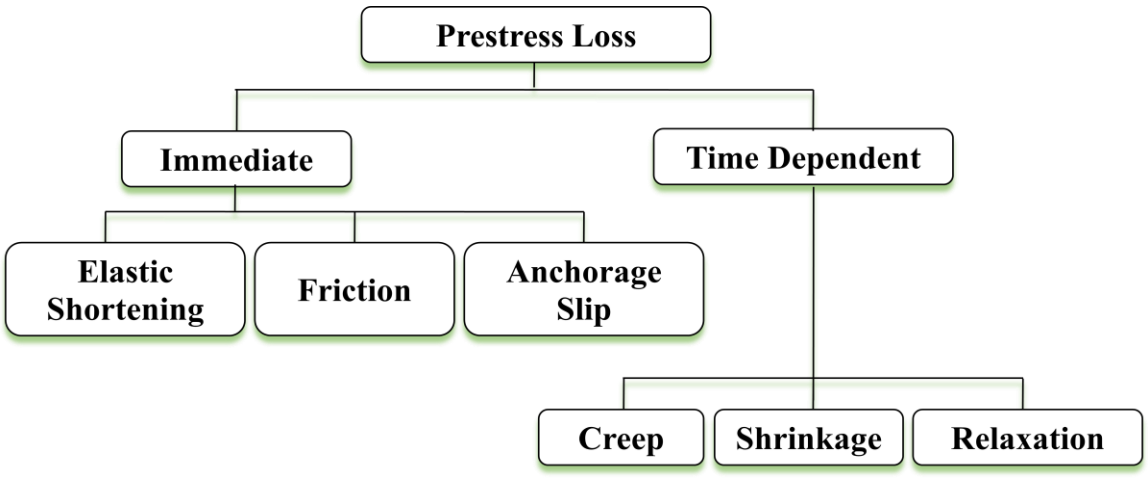

Fig. 1.4. Reasons for loss of prestress force

1.2. Foundation Settlement of Bridges

Foundations locate at the bottom of a bridge to take the bridge self-weight and service loads acting on the superstructure, as shown in Fig. 1.5. It is very common for them to settle down. Based on the surveys conducted by Grover [2] and Moulton [3], more than 70% of the bridges they investigated in US and Canada experienced settlement of foundations; abutments and piers resting on spread footings have a higher chance to settle down than those on pile foundations. Compression or consolidation of the underlying soil is the main reason for the settlement. Some other causes include scour, poor design, construction sequence, yielding of adjacent excavations and earthquakes. Fig. 1.6 shows pier foundation settlement of Juan Pablo II bridge in Chili due to earthquake-induced soil liquefaction. Settlement of foundations results in the displacement of all the members it supports and consequently may cause severe damage to bearings, decks and parapets. Besides, the interaction between the bridge and vehicles can be adversely affected and needs to be analyzed.

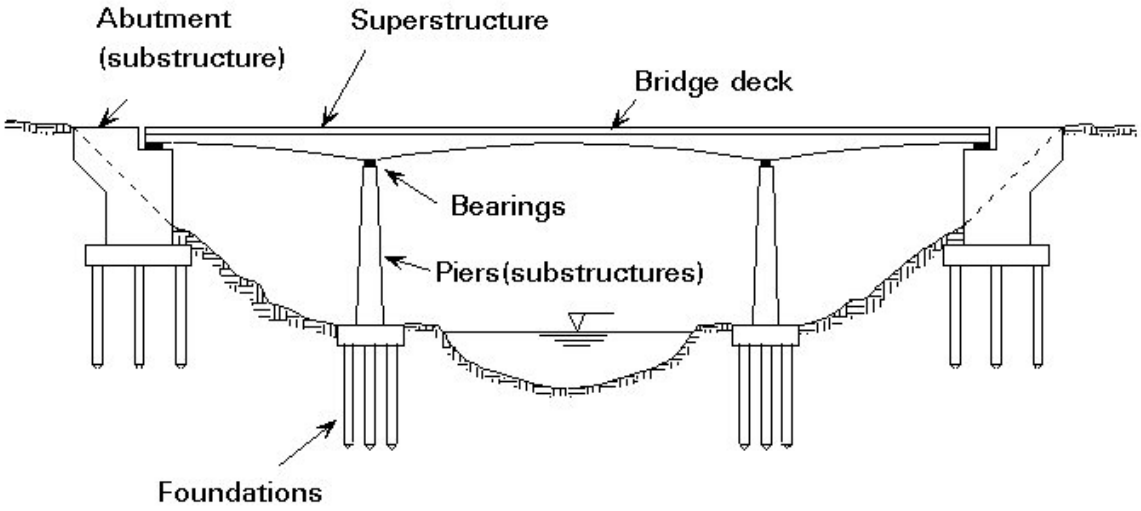

Fig. 1.5. Basic components of a bridge structure

Fig. 1.6. Liquefaction-induced settlement of pier foundations for Juan Pablo II bridge [4]

1.3. Bridge Vehicle Interaction Analysis

Bridge vehicle interaction is a classical topic in the field of civil engineering and has been studied for decades and by many researchers. However, the significance and intensity of the study on this topic keeps raising large interest and attention among researchers, due to rapid increase of the traffic volumes and aging of the nation's bridge. The initial or main purpose of bridge vehicle interaction analysis is to have a safe bridge design by investigating the dynamic behavior of a bridge under the heavy truck [5-12] or train loading [13-15] so that the resonance or excessive displacement of the bridge can be avoided. One of the most important factors in bridge design and analysis is the dynamic amplification factor or impact factor, describing the magnification effect of dynamic loading over the equivalent static load. Besides the main purpose, recently, some researchers proposed to identify vehicle parameters based on dynamic bridge responses [16, 17], or in opposite to conduct fast bridge condition assessment through the vehicle responses [18-22]. The following subsections introduce some basic information or knowledge involved in bridge vehicle interaction analysis.

1.3.1. Bridge and Vehicle Model

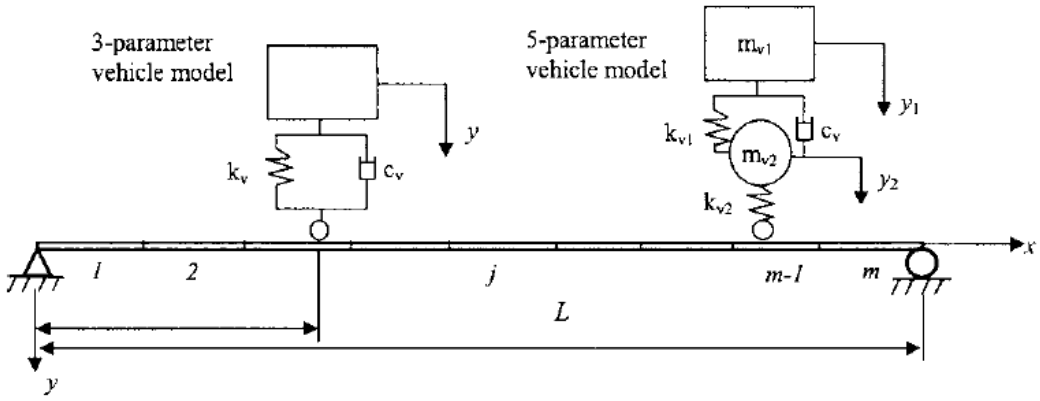

Fig. 1.7. Beam model of a bridge and quarter-vehicle models [18]

Fig. 1.7 shows two quarter-vehicle models traveling on a bridge beam model. In bridge vehicle interaction analysis, a bridge is commonly modeled as a beam [5-9] or plate [10-12, 15]. Recently, three-dimensional (3D) bridge model has been developed by researchers using finite element software [16]. Those bridge models can either be discretized into finite elements [7, 18] or acts as a whole body in model shapes [8-12]. Accordingly, the governing equation of motion of the bridge can be derived based on the finite element theory by assembling the local mass, damping and stiffness matrices of the elements to global matrices [7], or calculated through modal shape functions using modal superposition technique and energy principle [9]. The general form of the bridge vibration equation can be written as follows:

$$\boldsymbol{M_b\ddot{D}_b + C_b\dot{D}_b + K_bD_b = F_b} \tag{1.1}$$

where $\boldsymbol{M_b}$, $\boldsymbol{C_b}$ and $\boldsymbol{K_b}$ are the mass, damping and stiffness matrices of the bridge, respectively; $\boldsymbol{D_b}$ is the displacement vector of the bridge; $\boldsymbol{\dot{D}_b}$, $\boldsymbol{\ddot{D}_b}$ are the first and second derivatives of $\boldsymbol{D_b}$ with respect to time *t*; $\boldsymbol{F_b}$ is a vector of all external forces acting on the bridge.

Depending on the bridge models used and the need of the study, various vehicle models with different configurations and degrees of freedom can be adopted. In general, these models

can be classified into three categories: quarter-vehicle [5], half-vehicle [6-8], and full-vehicle [9-12]. Vehicles traveling on a bridge normally have three movement patterns: bounce (up-and-down motion), pitch (rotation about the lateral axis), and roll (rotation about longitudinal axis). Quarter-vehicle model only considers the bounce movement; half-vehicle model can describe both bounce and pitch movements but ignores the roll movement. Full-vehicle model takes bounce, pitch and roll movements all into account.

Using the Lagrange method or force equilibrium, the equation of motion for the vehicle can be derived and expressed in a general form as following:

$$\boldsymbol{M_v}\ddot{\boldsymbol{D}}_{\boldsymbol{v}} + \boldsymbol{C_v}\dot{\boldsymbol{D}}_{\boldsymbol{v}} + \boldsymbol{K_v}\boldsymbol{D_v} = \boldsymbol{F_v} \tag{1.2}$$

where $\boldsymbol{M_v}$, $\boldsymbol{C_v}$ and $\boldsymbol{K_v}$ are the mass, damping, and stiffness matrices of the vehicle, respectively; $\boldsymbol{D_v}$ is the displacement vector of the vehicle; $\dot{\boldsymbol{D}}_{\boldsymbol{v}}$, $\ddot{\boldsymbol{D}}_{\boldsymbol{v}}$ are the first and second derivatives of $\boldsymbol{D_v}$ with respect to time *t*; $\boldsymbol{F_v}$ is the vector of all external forces acting on the vehicle.

1.3.2. Modal Coupled and Uncoupled Method

With the governing equations for the vibration of the bridge and vehicle developed, there are two methods commonly used to solve for the dynamic bridge and vehicle responses: modal coupled and uncoupled methods, as shown in Fig. 1.8. Uncoupled method [6-8] calculates the bridge and vehicle responses separately using the corresponding individual models, and communicates with each other through the interaction forces between the bridge surface and vehicle tires. In each time step, an iterative process is continued until stable responses are reached or in other words the equilibrium between the bridge and vehicle is found. As for coupled method [11, 16, 18], it unites the bridge and vehicle models into one system through the interaction forces, thus, no iterations are required in each time step. However, to maintain the same accuracy as the uncoupled method, coupled method needs a smaller time step.

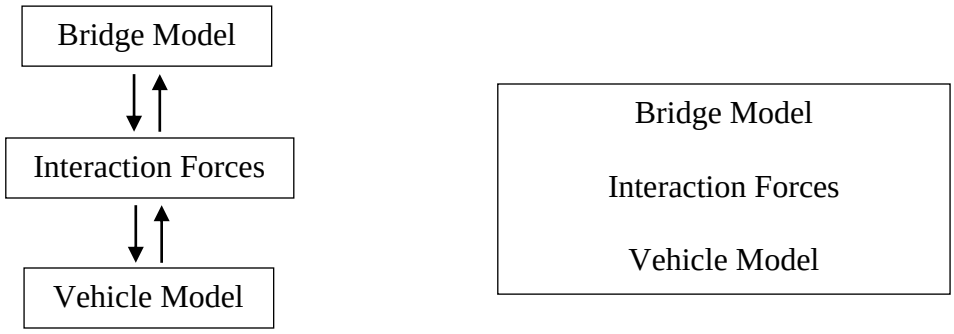

Fig. 1.8. Modal uncoupled (a) and coupled method (b)

1.3.3. Numerical Algorithms

There are several numerical algorithms, either explicit or implicit, widely used to compute the dynamic behavior of the bridge and vehicle, including state space method [18,23], Newmark-beta method [6-8,10,12] and Runge–Kutta method [11,16]. Among them, Newmark-beta method gains the most popularity. For more details, please see the corresponding references.

1.4. Statement of the Problem

1.4.1. Dynamic Behavior of Prestressed Bridges

Prestressed bridges have gained widespread popularity in recent decades due to high strength and excellent crack resistance. Some research has been conducted on dynamic characteristics or vibration of prestressed bridges. Saiidi et al. [24] studied the effect of prestress force on natural frequencies of concrete bridges and found that the bridge frequency increases with the applied force. Kocatürk and Şimşek [25-27] investigated the vibration of simply-supported viscoelastic Timoshenko beams under an eccentric compressive force and a concentrated moving harmonic force, without interaction between the beam and applied forces. Khang et al. [28] simulated the transverse vibration of prestressed continuous beams on rigid supports subjected to moving single degree of freedom bodies, neglecting the eccentricity of the

prestress. So far, the vibration of prestressed bridges under the action of moving vehicular loads with consideration of the prestress eccentricity has not been analyzed in previous works.

1.4.2. Effect of Foundation Settlement on Bridges

Foundation settlement as a common phenomenon has been noticed and studied by researchers. Moulton [3] surveyed the bridges in US and Canada and concluded that the bridges undergoing settlement less than 0.4% of their span lengths remained structurally sound, which has been accepted and suggested by AASHTO [29]. Wang et al. [30] simulated different types of real continuous bridges and found that the maximum moment and shear force ratios between the cases with/without considering settlement effects can reach 4 and 1.8, respectively. Most literatures focus on the static effect of foundation settlement on superstructure integrity and serviceability of the bridge, however, the effect of bridge settlement on dynamic behaviors of the bridge and vehicles travelling over it has not been investigated yet.

1.4.3. Prestress Loss Identification

Loss of prestress can lead to malfunction and even failure of the prestressed bridges. Therefore, it is crucial to monitor the prestress loss of the bridge under service. Many approaches have been developed to conduct the monitoring and assessment. Generally, these methods can be categorized into two types: direct and indirect. Direct methods install various sensors or gauges directly on the prestressed steel brands to identify the prestress-loss in prestressed concrete (PSC) beams or girders. Electrical-resistance strain gauges [31], vibrating-wire strain gauges [32], shaped memory alloy (SMA) sensors [33], fiber optic sensors [34-39] have been used. Indirect methods measure some other signals outside the concrete member to inversely analyze the prestress force rather than conduct direct measurements on the prestressed strands. In other words, the detection of the prestress loss is performed in an indirect way. Some examples include

ultrasonic-wave-based methods [40-43] and vibration-based methods [44-46]. Both direct and indirect methods mentioned above are based on the measurement of responses of the bridge that requires the installment of sensors on bridges, which is not only costly but also inconvenient.

Recently, indirect bridge health monitoring through vehicle responses has gained increasing attention. At the first, Yang et al. [19, 20] proposed to extract natural frequencies of a bridge through FFT analysis of the time history of a passing vehicle and verified the feasibility of this method in practice through a field experiment. Following Yang's work, identification of damping and mode shapes of a bridge through measurement of the vehicle response was completed by Gonzalez et al. [21] and Malekjafarian et al. [22], respectively. Bu et al. [18] developed an innovative identification algorithm to detect the bridge damages based on the sensitivity analysis of dynamic vehicle response. Zhang et al. made use of the mode shape squares [47] and operating deflection shape curvature [48] extracted from the acceleration of a passing vehicle under a tapping force to conduct damage detection of a bridge. The aforementioned research work opened a new door to bridge health monitoring - identifying the condition of bridges through dynamic response of an instrumented passing vehicle, which is not only efficient but also cost-effective. This provides a possibility for vehicle-response-based prestress loss identification.

1.5. Research Objectives

The study of the dissertation focuses on the dynamic interaction between vehicles and bridges subjected to prestress force loss and foundation settlement. There are three main objectives of the research:

- To develop a bridge vehicle interaction model with consideration of the prestress force and parametrically study the effect of prestress on dynamic responses of bridges and vehicles;
- To model the interaction between the vehicle and bridges subjected to foundation settlement and analyze the dynamic effect of foundation settlement on the performance of bridge and vehicle;
- To investigate the possibility of prestress loss identification through dynamic vehicle responses and vehicle parameters optimization.

1.6. Organization of the Dissertation

This dissertation consists of five chapters. Chapter 1 is a general introduction to the subject as well as statement of the problem and research objectives. Chapters 2-4 each cover one topic and are written in a paper style, self-contained with the individual abstract, introduction, main contents, and conclusions. Chapter 2 presents the developed prestressed bridge vehicle interaction model and numerical simulations to study the effects of the prestress force, eccentricity, span number, span length, and the presence of multiple vehicles on dynamic bridge and vehicle responses. Chapter 3 investigates the influence of foundation settlement on dynamic bridge and vehicle interaction with consideration of settlement modes, vehicle speeds, road surface roughness, and support conditions. Chapter 4 proposes to detect prestress loss of the bridge through dynamic vehicle responses and performs simulations to optimize the vehicle parameters for the purpose of prestress loss identification. Chapter 5 summarizes the major findings of the dissertation research.

1.7. References

[1] US Department of Transportation, Federal Highway Administration, Bridges by Year Built, Year Reconstructed and Material Type 2013, National Bridge Inventory (NBI), http://www.fhwa.dot.gov/bridge/nbi/no10/yrblt_yrreconst13.cfm#b.

[2] Grover, R. A. (1978). Movements of bridge abutments and settlements of approach pavements in Ohio. Transportation Research Record No. 678, Transportation Research Board, Washington, D.C., 12-17.

[3] Moulton, L. K., GangaRao, H. V., & Halvorsen, G. T. (1985). Tolerable movement criteria for highway bridges. Federal Highway Administration (Report No. FHWA/RD-85-107), Washington.

[4] US Department of Transportation, Federal Highway Administration, Post-Earthquake Reconnaissance Report on Transportation Infrastructure: Impact of the February 27, 2010, Offshore Maule Earthquake in Chile, http://www.fhwa.dot.gov/publications/research/infrastructure/structures/11030/005.cfm

[5] Green, M. F., & Cebon, D. (1997). Dynamic interaction between heavy vehicles and highway bridges. *Computers & structures*, *62*(2), 253-264.

[6] Law, S. S., & Zhu, X. Q. (2005). Bridge dynamic responses due to road surface roughness and braking of vehicle. *Journal of Sound and Vibration*, *282*(3), 805-830.

[7] Yang, Y. B., & Wu, Y. S. (2001). A versatile element for analyzing vehicle–bridge interaction response. *Engineering structures*, *23*(5), 452-469.

[8] Zhong, H., Yang, M., & Gao, Z. J. (2015). Dynamic responses of prestressed bridge and vehicle through bridge–vehicle interaction analysis. *Engineering Structures*, *87*, 116-125.

[9] Marchesiello, S., Fasana, A., Garibaldi, L., & Piombo, B. A. D. (1999). Dynamics of multi-span continuous straight bridges subject to multi-degrees of freedom moving vehicle excitation. *Journal of Sound and Vibration*, *224*(3), 541-561.

[10] Zhu, X. Q., & Law, S. S. (2002). Dynamic load on continuous multi-lane bridge deck from moving vehicles. *Journal of Sound and Vibration*, *251*(4), 697-716.

[11] Cai, C. S., Shi, X. M., Araujo, M., & Chen, S. R. (2007). Effect of approach span condition on vehicle-induced dynamic response of slab-on-girder road bridges. *Engineering Structures*, *29*(12), 3210-3226.

[12] Ahmari, S., Yang, M., & Zhong, H. (2015). Dynamic interaction between vehicle and bridge deck subjected to support settlement. *Engineering Structures*, *84*, 172-183.

[13] Tanabe, M., Yamada, Y., & Hajime, W. (1987). Modal method for interaction of train and bridge. *Computers & Structures*, *27*(1), 119-127.

[14] Delgado, R. M. (1997). Modelling of railway bridge-vehicle interaction on high speed tracks. *Computers & Structures*, *63*(3), 511-523.

[15] Song, M. K., Noh, H. C., & Choi, C. K. (2003). A new three-dimensional finite element analysis model of high-speed train–bridge interactions. *Engineering Structures*, *25*(13), 1611-1626.

[16] Deng, L., & Cai, C. S. (2009). Identification of parameters of vehicles moving on bridges. *Engineering Structures*, *31*(10), 2474-2485.

[17] Jiang, R. J., Au, F. T. K., & Cheung, Y. K. (2004). Identification of vehicles moving on continuous bridges with rough surface. Journal of Sound and Vibration, 274(3), 1045-1063.

[18] Bu, J. Q., Law, S. S., & Zhu, X. Q. (2006). Innovative bridge condition assessment from dynamic response of a passing vehicle. *Journal of Engineering Mechanics*, *132*(12), 1372-1379.

[19] Yang, Y. B., Lin, C. W., & Yau, J. D. (2004). Extracting bridge frequencies from the dynamic response of a passing vehicle. *Journal of Sound and Vibration*, *272*(3), 471-493.

[20] Lin, C. W., & Yang, Y. B. (2005). Use of a passing vehicle to scan the fundamental bridge frequencies: An experimental verification. *Engineering Structures*, *27*(13), 1865-1878.

[21] González, A., OBrien, E. J., & McGetrick, P. J. (2012). Identification of damping in a bridge using a moving instrumented vehicle. *Journal of Sound and Vibration*, *331*(18), 4115-4131.

[22] Malekjafarian, A., & OBrien, E. J. (2014). Identification of bridge mode shapes using short time frequency domain decomposition of the responses measured in a passing vehicle. *Engineering Structures*, *81*, 386-397

[23] Henchi, K., Fafard, M., Talbot, M., & Dhatt, G. (1998). An efficient algorithm for dynamic analysis of bridges under moving vehicles using a coupled modal and physical components approach. *Journal of Sound and Vibration*, *212*(4), 663-683.

[24] Saiidi, M., Douglas, B., & Feng, S. (1994). Prestress force effect on vibration frequency of concrete bridges. *Journal of structural Engineering*, *120*(7), 2233-2241.

[25] Kocatürk, T., & Şimşek, M. (2006). Vibration of viscoelastic beams subjected to an eccentric compressive force and a concentrated moving harmonic force. *Journal of Sound and Vibration*, *291*(1), 302-322.

[26] Kocatürk, T., & Şimşek, M. (2006). Dynamic analysis of eccentrically prestressed viscoelastic Timoshenko beams under a moving harmonic load. *Computers & structures*, *84*(31), 2113-2127.

[27] Şimşek, M., & Kocatürk, T. (2009). Nonlinear dynamic analysis of an eccentrically prestressed damped beam under a concentrated moving harmonic load. *Journal of Sound and Vibration*, *320*(1), 235-253.

[28] Van Khang, N., Dien, N. P., & Van Huong, N. T. (2009). Transverse vibrations of prestressed continuous beams on rigid supports under the action of moving bodies. *Archive of Applied Mechanics*, *79*(10), 939-953.

[29] AASHTO LRFD Bridge Design Specifications, 5th ed. (2010). American Association of State Highway and Transportation Officials, Washington, D.C.

[30] Wang, Z., Chen, G., Kwon, O. S., & Orton, S. (2011). Calibration of load and resistance factors in LRFD foundation design specifications. U.S. Department of Transportation (Report No. NUTC R237), Washington, D.C.

[31] Ahlborn, T. M., Shield, C. K., & French, C. W. (1997). Full-scale testing of prestressed concrete bridge girders. *Experimental Techniques*, *21*(1), 33-35.

[32] Barr, P. J., Kukay, B. M., & Halling, M. W. (2008). Comparison of prestress losses for a prestress concrete bridge made with high-performance concrete. *Journal of Bridge Engineering*, *13*(5), 468-475.

[33] Maji, A. K., & Negret, I. (1998). Smart prestressing with shape-memory alloy. *Journal of engineering mechanics*, *124*(10), 1121-1128.

[34] Gao, J., Shi, B., Zhang, W., & Zhu, H. (2006). Monitoring the stress of the post-tensioning cable using fiber optic distributed strain sensor. *Measurement*, *39*(5), 420-428.

[35] Zhou, Z., He, J., Chen, G., & Ou, J. (2009). A smart steel strand for the evaluation of prestress loss distribution in post-tensioned concrete structures. *Journal of Intelligent Material Systems and Structures*, *20*(16), 1901-1912.

[36] Lan, C., Zhou, Z., & Ou, J. (2012). Full-scale prestress loss monitoring of damaged RC structures using distributed optical fiber sensing technology. *Sensors*, *12*(5), 5380-5394.

[37] Lan, C., Zhou, Z., & Ou, J. (2014). Monitoring of structural prestress loss in RC beams by inner distributed Brillouin and fiber Bragg grating sensors on a single optical fiber. *Structural Control and Health Monitoring*, *21*(3), 317-330.

[38] Abdel-Jaber, H., & Glisic, B. (2014). A method for the on-site determination of prestressing forces using long-gauge fiber optic strain sensors. *Smart Materials and Structures*, *23*(7), 075004.

[39] Wang, C., & Cheng, L. (2014). Use of fiber Bragg grating sensors for monitoring concrete structures with prestressed near-surface mounted carbon fiber–reinforced polymer strips. *Journal of Intelligent Material Systems and Structures*, *25*(2), 164-173.

[40] Chen, R. H., & Wissawapaisal, K. (2002). An ultrasonic method for measuring tensile forces in a seven-wire prestressing strand. *Quantitative Nondestructive Evaluation*, *615*(1), 1295-1302.

[41] Beard, M. D., Lowe, M. J. S., & Cawley, P. (2003). Ultrasonic guided waves for inspection of grouted tendons and bolts. *Journal of Materials in Civil Engineering*, *15*(3), 212-218.

[42] Nucera, C., & di Scalea, F. L. (2011). Monitoring load levels in multi-wire strands by nonlinear ultrasonic waves. *Structural Health Monitoring*, *10*(6), 617-629.

[43] Bartoli, I., Salamone, S., Phillips, R., Lanza di Scalea, F., & Sikorsky, C. S. (2011). Use of interwire ultrasonic leakage to quantify loss of prestress in multiwire tendons. *Journal of Engineering Mechanics*, *137*(5), 324-333.

[44] Kim, J. T., Yun, C. B., Ryu, Y. S., & Cho, H. M. (2004). Identification of prestress-loss in PSC beams using modal information. *Structural Engineering and Mechanics*, *17*(3-4), 467-482.

[45] Kim, J. T., Park, J. H., Hong, D. S., Cho, H. M., Na, W. B., & Yi, J. H. (2009). Vibration and impedance monitoring for prestress-loss prediction in PSC girder bridges. *Smart Structures and Systems*, *5*(1), 81-94.

[46] Lu, Z. R., & Law, S. S. (2006). Identification of prestress force from measured structural responses. *Mechanical Systems and Signal Processing*, *20*(8), 2186-2199.

[47] Zhang, Y., Wang, L., & Xiang, Z. (2012). Damage detection by mode shape squares extracted from a passing vehicle. *Journal of Sound and Vibration*, *331*(2), 291-307.

[48] Zhang, Y., Lie, S. T., & Xiang, Z. (2013). Damage detection method based on operating deflection shape curvature extracted from dynamic response of a passing vehicle. *Mechanical Systems and Signal Processing*, *35*(1), 238-254.

CHAPTER 2. DYNAMIC RESPONSES OF PRESTRESSED BRIDGE AND VEHICLE THROUGH BRIDGE-VEHICLE INTERACTION ANALYSIS

2.1. Abstract

Existence of prestress in bridges affects the dynamic responses of both bridges and vehicles traveling over them. In this paper, the bridge is modeled as a continuous beam with eccentric prestress, and a half-vehicle model with 4 degrees of freedom is used to represent the vehicle passing the bridge. A new bridge-vehicle model with consideration of prestress effect is created through the principle of virtual works to investigate the continuous prestressed bridges and vehicle interaction responses. The correctness and accuracy of the model are validated with literature results and Abaqus model. Based on the created model, numerical simulations have been conducted using the Newmark integration method to perform a parametric study on effects of number of bridge spans, span length, eccentricity and amplitude of prestress. It is shown that prestress has a significant effect on the maximum vertical acceleration of vehicles, which may provide a good index for detecting the change of prestress.

2.2. Introduction

Highway bridges serve as a vital component in modern infrastructures. The safety of these bridges is a great concern of government agencies and general public. Many destructive and nondestructive methods have been used to evaluate bridge fitness for serving the anticipated traffic flow [1-3]. In this paper, a model capturing the responses of prestressed bridges and vehicles will be created and later used as a structural health monitoring method for detecting prestress losses.

Extensive research has been conducted to study the bridge vehicle interaction. Zhu and Law [4] studied the continuous bridge and vehicle interaction, in which the dynamics of the

bridge deck under single and several vehicles moving in different lanes is analyzed using the orthotropic plate theory and modal superposition technique. The dynamic impact factor is also summarized for different vehicle traveling speeds. Yang and Papagiannakis [5] studied the composite bridge and vehicle interactions and found that the dynamic impact factors are increased for bridges using FRP sandwich decks. Green and Cebon [6] studied dynamic responses of highway bridges to heavy vehicle loads and good agreements are found for the measured dynamic bridge midspan displacement and the predicted bridge midspan displacement. Kocaturk and Simsek [7] utilized the Lagrange equations to solve the dynamic response of a simply supported beam subjected to an eccentric compressive force and a concentrated moving harmonic force. Khang et al. [8] investigated transverse vibrations of prestressed continuous beams under the action of moving bodies by using the method of substructure, which neglected the eccentricity of the prestress. Cai et al. [9-12] particularly studied dynamic impact factor for performance evaluation of bridges and researched effect of wind and bridge approach length on responses of bridge vehicle interaction. However, the influence of the prestress with eccentricity on the dynamic responses of both continuous bridges and vehicles traveling over them has not been considered in these works.

In the present study, the dynamic responses of prestressed continuous bridges and vehicles traveling over them are investigated. The bridge is modeled as a continuous beam with eccentric prestress. A half-vehicle model with 4 degrees of freedom is used to represent the vehicle passing the bridge. A new bridge-vehicle model with consideration of prestress effect is created through the principle of virtual works. Based on the created model, the bridge-vehicle interaction response is solved by using the Newmark integration method. Through the conducted numerical simulations, effects of number of bridge span, span length, eccentricity and amplitude

of prestress are analyzed and discussed. It is anticipated that results given in this paper will help quantifying the loss of prestress in field.

2.3. Dynamic Behaviors of Prestressed Bridge and Vehicle

2.3.1. Equation of Motion for the Prestressed Bridge

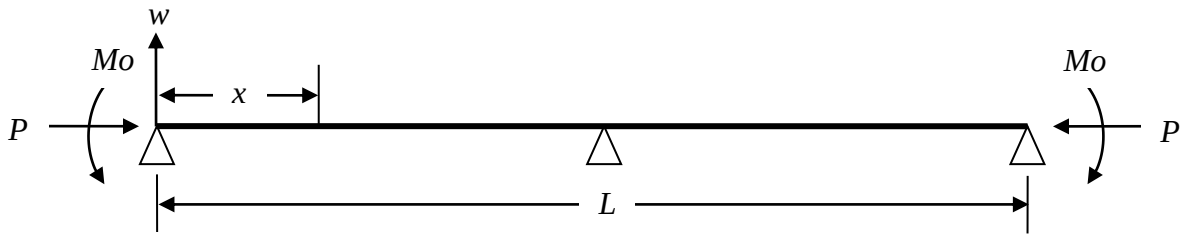

Fig. 2.1. Schematic of an eccentrically two-span continuous prestressed bridge

As shown in Fig. 2.1, a two-span continuous eccentrically-prestressed bridge can be simplified as a continuous beam subjected to one axial force (P) and one initial moment (M_o) at the two ends.

Based on the modal superposition principle, dynamic deflection $w(x,t)$ of the beam can be described as:

$$w(x,t) = \sum_{i=1}^{N} W_i(x)\, q_i(t) \tag{2.1}$$

where $W_i(x)$, $q_i(t)$, and N are the i^{th} mode shape function of the beam, the corresponding modal amplitude of the beam, and the selected number of mode shapes respectively.

According to the principle of virtual displacement [13], the external virtual work δW_E is equal to the internal virtual work δW_I:

$$\delta W_E = \delta W_I \tag{2.2}$$

The virtual displacements $\delta q_i W_i(x)$, i=1,2,…,N, are selected to be consistent with the assumed shape functions. The external virtual work is the sum of the works (δW_{in}, δW_V, δW_C, δW_P and δW_{M_o}) performed by the inertia force ($\bar{m}\frac{\partial^2 w}{\partial t^2}$), the moving vehicle tire loads (F_b^{int}), the

damping forces ($-c_{bi}\frac{\partial w}{\partial t}$) , the prestress force (P), and the moment (M_o), which can be written as:

$$\delta W_E = \delta W_{in} + \delta W_V + \delta W_C + \delta W_P + \delta W_{M_o} \tag{2.3}$$

where

$$\delta W_{in} = -\delta q_i \int_0^L W_i(x)\bar{m}\frac{\partial^2 w}{\partial t^2}dx$$

$$\delta W_V = \delta q_i \int_0^L \sum_{k=1}^{2} F_b^{int}(k)\,\delta[x - \widehat{x_k}(t)]W_i[\widehat{x_k}(t)]dx$$

$$\delta W_C = -\delta q_i \int_0^L c_{bi}(\frac{\partial w}{\partial t})W_i(x)dx \quad c_{bi} = 2\bar{m}\omega_i\zeta_i$$

$$\delta W_P = \delta q_i \int_0^L P\left(\frac{\partial w}{\partial x}\right)W_i'(x)dx$$

$$\delta W_{M_o} = \delta q_i[M_o W_i'(0) - M_o W_i'(L)] \tag{2.4}$$

and $\bar{m}$ is the mass of the beam per unit length; ω_i, ζ_i, c_{bi} is the natural frequency, damping ratio and damping coefficient for the i^{th} mode of the beam respectively; $F_b^{int}(k)$ is the k^{th} interaction force between the wheel of the vehicle and the bridge; $\widehat{x_k}(t)$ is the location of the k^{th} interaction force $F_b^{int}(k)$; $\delta(x)$ is the Dirac function; $W_i'(x)$ denotes the first derivative of $W_i(x)$ with respect to x.

The internal virtual work performed by the bending moment is:

$$\delta W_I = \delta q_i \int_0^L EI\left(\frac{\partial^2 w}{\partial x^2}\right)W_i''(x)dx \tag{2.5}$$

where EI is flexural rigidity of the beam; $W_i''(x)$ denotes the second derivative of $W_i(x)$ with respect to x.

Substituting Eq. (2.1) and Eqs. (2.3) ~ (2.5) into Eq. (2.2) and cancelling δq_i at both sides give

$$\sum_{j=1}^{N}\ddot{q}_j M_{bij} + \sum_{j=1}^{N}\dot{q}_j C_{bij} + \sum_{j=1}^{N} q_j(K_{bij} - K_{Gij}) = (W_V)_i + \left(W_{M_o}\right)_i \tag{2.6}$$

where

$$M_{bij} = \int_0^L \bar{m} W_i(x) W_j(x) dx \qquad K_{bij} = \int_0^L EI W_i''(x) W_j''(x) dx$$

$$K_{Gij} = \int_0^L P W_i'(x) W_j'(x) dx \qquad C_{bij} = \int_0^L c_{bi} W_i(x) W_j(x) dx$$

$$(W_V)_i = \sum_{k=1}^{2} F_b^{int}(k)\, W_i\big(\widehat{x_k}(t)\big) \qquad \big(W_{M_o}\big)_i = M_o W_i'(0) - M_o W_i'(L) \qquad (2.7)$$

, $\dot{q}_j$ and $\ddot{q}_j$ denote the first and second derivative of $q_j(t)$ with respect to time *t*.

Corresponding to the N independent virtual displacements $\delta q_i W_i(x)$, *i*=1,2,…,N, there are N virtual work equations in the form of Eq. (2.6). Together they can be expressed in matrix form as:

$$\boldsymbol{M_b}\ddot{\boldsymbol{Q}} + \boldsymbol{C_b}\dot{\boldsymbol{Q}} + (\boldsymbol{K_b} - \boldsymbol{K_G})\boldsymbol{Q} = \boldsymbol{W_V} + \boldsymbol{W_{M_o}} \qquad (2.8)$$

where

$$\boldsymbol{Q} = \{q_1(t), q_2(t), \dots, q_N(t)\}^T \qquad \boldsymbol{W_V} = W_b F_b^{int}$$

$$\boldsymbol{W_b} = \begin{bmatrix} W_1(\widehat{x_1}(t)) & W_1(\widehat{x_2}(t)) \\ \vdots & \\ W_N(\widehat{x_1}(t)) & W_N(\widehat{x_2}(t)) \end{bmatrix} \qquad \boldsymbol{F_b^{int}} = \begin{bmatrix} F_{t1} \\ F_{t2} \end{bmatrix} \qquad \boldsymbol{W_{M_o}} = \begin{Bmatrix} M_o[W_1'(0) - W_1'(L)] \\ \vdots \\ M_o[W_N'(0) - W_N'(L)] \end{Bmatrix} \qquad (2.9)$$

, $\boldsymbol{M_b}$, $\boldsymbol{K_b}$, $\boldsymbol{C_b}$ and $\boldsymbol{K_G}$ are the mass, stiffness, damping, and geometric stiffness matrices of the bridge respectively with their (*i*, *j*)th element calculated in Eq. (2.7); $\dot{\boldsymbol{Q}}$, $\ddot{\boldsymbol{Q}}$ are the first and second derivatives of $\boldsymbol{Q}$ with respect to time *t*; F_{t1}, F_{t2} are the bridge-vehicle interaction forces at the front and rear wheel locations shown in Eq. (2.19).

Actually, due to the axial force (*P*) and moment (M_o) at the two ends, the prestressed bridge has initial deflection (w_0) before it vibrates under the moving vehicle. The initial deflection of the bridge can be determined by Eq. (2.8) with $\dot{\boldsymbol{Q}}_{\boldsymbol{0}} = \ddot{\boldsymbol{Q}}_{\boldsymbol{0}} = (\boldsymbol{W_b F_b^{int}})_{t=0} = [\boldsymbol{0}]_{\boldsymbol{N\times 1}}$ at the time t = 0 and Eq. (2.1) as following:

$$(\boldsymbol{K_b} - \boldsymbol{K_G})\boldsymbol{Q_0} = \boldsymbol{W_{M_o}}$$

$$w_0 = \boldsymbol{W}\boldsymbol{Q_0} \tag{2.10}$$

where

$$\boldsymbol{W} = \{W_1(x), W_2(x), \dots, W_N(x)\}$$

$$\boldsymbol{Q_0} = \{q_1(0), q_2(0), \dots, q_N(0)\}^T \tag{2.11}$$

2.3.2. Modal Analysis of the Prestressed Bridge

For the free vibration of the beam, its vertical deflection can be expressed as:

$$w(x,t) = W(x)e^{i\omega t} \tag{2.12}$$

where ω is the natural frequency of the vibration and $i = \sqrt{-1}$.

The mode shape function of the beam $W(x)$ may be expressed in term of a series as:

$$W(x) = \sum_m A_m \varphi_m(x) \tag{2.13}$$

where $\varphi_m(x)$ is the assumed admissible function satisfying the boundary conditions of the beam and A_m is undermined coefficient. The selection of $\varphi_m(x)$ follows the method proposed by Zhou [14], which composes of free vibrating beam eigenfunctions and polynomials. It is of great importance to note that here the moment (M_o) is taken as an acting force but not a boundary condition.

Now the Rayleigh's method is used to determine the natural frequencies and mode shapes of the prestressed beam.

The maximum potential and kinetic energies of the prestressed beam over a vibration cycle can be expressed as follows:

$$E_{So} = \int_0^L \left\{ \frac{1}{2} EI \left[\frac{\partial^2 W(x)}{\partial x^2} \right]^2 - \frac{1}{2} P \left[\frac{\partial w}{\partial x} \right]^2 \right\} dx$$

$$E_{Ko} = \int_0^L \frac{1}{2} \bar{m} \omega^2 [W(x)]^2 \, dx \tag{2.14}$$

Substituting Eq. (2.13) into Eq. (2.14) and taking the first derivation of the Rayleigh's quotient with respect to each coefficient A_m would lead to the eigenvalue equations in a matrix form as following:

$$(\boldsymbol{K} - \omega^2 \boldsymbol{M})\boldsymbol{A} = \boldsymbol{0} \tag{2.15}$$

where

$$\boldsymbol{A} = \{A_1, A_2, \ldots . A_m\}^T$$

$$\boldsymbol{K_{ij}} = \int_0^L [EI\varphi_i''(x)\varphi_j''(x) - P\varphi_i'(x)\varphi_j'(x)]dx$$

$$\boldsymbol{M_{ij}} = \int_0^L \bar{m}\varphi_i(x)\varphi_j(x)dx$$

$$(i = 1, 2, \cdots, m; j = 1, 2, \cdots, m) \tag{2.16}$$

, m is the number of assumed admissible functions; $\varphi_i'(x)$, $\varphi_i''(x)$ are the first and second derivatives of $\varphi_i(x)$ with respect to x.

The natural frequencies ω and coefficients A_m can be determined from Eq. (2.15). Then the mode shape functions of the beam $W(x)$ can be determined through Eq. (2.13).

2.3.3. Vehicle Modal

To better understand the bridge-vehicle interaction, a half-vehicle vibration model shown in Fig. 2.2 is adopted in current study. This vehicle model has four degrees of freedom, corresponding to the vertical displacement of vehicular body (z_c), rotation of vehicular body about the transverse axis (θ_c), the vertical displacements of the front wheel (z_f) and rear wheel (z_r). Applying the Lagrange method [15], the equations of motion for the half-vehicle model can be derived and expressed in a matrix form as following:

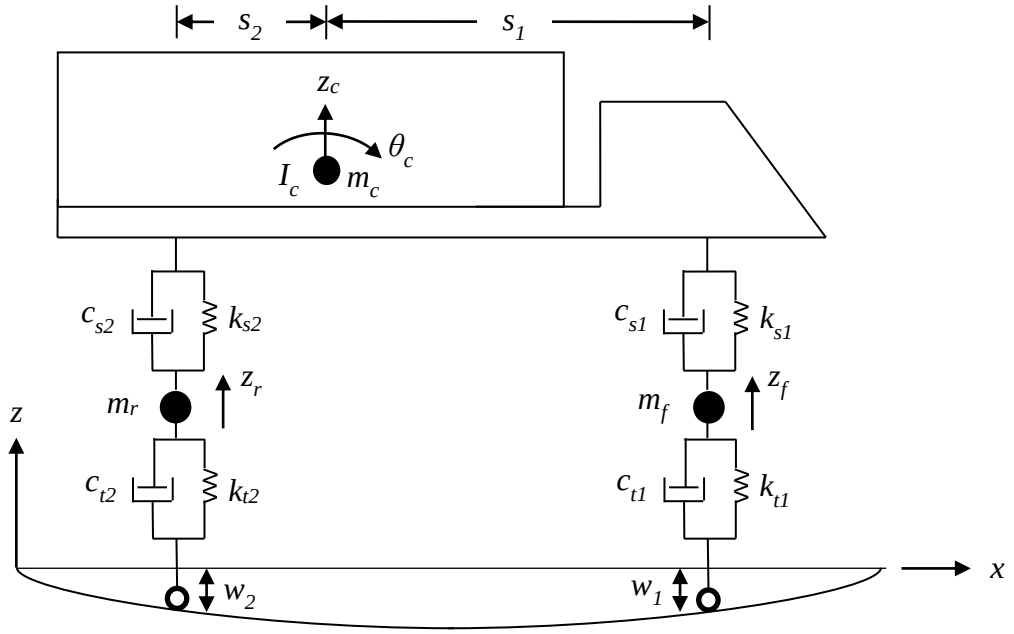

Fig. 2.2. Half-vehicle vibration model

$$\boldsymbol{M_v\ddot{Z} + C_v\dot{Z} + K_vZ = F_v^{int}} \tag{2.17}$$

where

$$\boldsymbol{Z} = \begin{bmatrix} Z_c \\ \theta_c \\ Z_f \\ Z_r \end{bmatrix} \qquad \boldsymbol{M_v} = \begin{bmatrix} m_c & 0 & 0 & 0 \\ 0 & I_c & 0 & 0 \\ 0 & 0 & m_f & 0 \\ 0 & 0 & 0 & m_r \end{bmatrix} \qquad \boldsymbol{F_v^{int}} = \begin{bmatrix} 0 \\ 0 \\ k_{t1}(w_1 + r_1) + c_{t1}(\dot{w}_1 + \dot{r}_1) \\ k_{t2}(w_2 + r_2) + c_{t2}(\dot{w}_2 + \dot{r}_2) \end{bmatrix}$$

$$\boldsymbol{C_v} = \begin{bmatrix} c_{s1} + c_{s2} & s_2c_{s2} - s_1c_{s1} & -c_{s1} & -c_{s2} \\ s_2c_{s2} - s_1c_{s1} & s_1^2c_{s1} + s_2^2c_{s2} & s_1c_{s1} & -s_2c_{s2} \\ -c_{s1} & s_1c_{s1} & c_{s1} + c_{t1} & 0 \\ -c_{s2} & -s_2c_{s2} & 0 & c_{s2} + c_{t2} \end{bmatrix}$$

$$\boldsymbol{K_v} = \begin{bmatrix} k_{s1} + k_{s2} & s_2k_{s2} - s_1k_{s1} & -k_{s1} & -k_{s2} \\ s_2k_{s2} - s_1k_{s1} & s_1^2k_{s1} + s_2^2k_{s2} & s_1k_{s1} & -s_2k_{s2} \\ -k_{s1} & s_1k_{s1} & k_{s1} + k_{t1} & 0 \\ -k_{s2} & -s_2k_{s2} & 0 & k_{s2} + k_{t2} \end{bmatrix} \tag{2.18}$$

, $\boldsymbol{\dot{Z}}$, $\boldsymbol{\ddot{Z}}$ are the first and second derivatives of $\boldsymbol{Z}$ with respect to time t; m_c, I_c, m_f, m_r are half of vehicular body mass, half of vehicular body lateral mass moment of inertia, the mass of a front wheel, and the mass of a rear wheel respectively; k_{s1}, k_{s2}, c_{s1}, c_{s2} are the stiffness and damping

coefficients of the front and rear suspensions respectively; k_{t1}, k_{t2}, c_{t1}, c_{t2} are the stiffness and damping coefficients of the front and rear tires respectively; s_1, s_2 are the distance of the center of gravity of the vehicular body from the front and rear axles respectively; w_1, w_2 are the deflection of the bridge at the front and rear wheel locations respectively; and $\dot{w}_1$, $\dot{w}_2$ are the first derivative of w_1, w_2 with respect to time *t*. Note that vehicle displacement vector $\boldsymbol{Z}$ is measured from the static equilibrium position of the vehicle, which leads to no gravity term in Eq. (2.17).

2.3.4. Vehicle-Bridge Interaction

The bridge-vehicle interaction forces for a single vehicle can be described as follows:

$$F_{t1} = k_{t1}(Z_f - w_1) + c_{t1}(\dot{Z}_f - \dot{w}_1) - \left(m_f + m_c \frac{s_2}{s_1 + s_2}\right) g$$

$$F_{t2} = k_{t2}(Z_r - w_2) + c_{t2}(\dot{Z}_r - \dot{w}_2) - (m_r + m_c \frac{s_1}{s_1 + s_2}) g \quad (2.19)$$

2.4. Numerical Simulations

2.4.1. Numerical Algorithm

The dynamic responses of the bridge and vehicle can be calculated from Eqs. (2.8), (2.9), (2.17), (2.18), and (2.19) using the Newmark integration method [16]. The implementation procedure of the Newmark integration method is shown in Fig. 2.3, in which v is the speed of the vehicle and ***Error*** representing the difference between the results of two consecutive iterations is defined as following:

$$Error = \sqrt{\left[\frac{w_1(x,t)_j - w_1(x,t)_{j-1}}{w_1(x,t)_j}\right]^2 + \left[\frac{w_2(x,t)_j - w_2(x,t)_{j-1}}{w_2(x,t)_j}\right]^2} \quad (2.20)$$

where $w_1(x,t)_{j-1}$, $w_1(x,t)_j$ are the deflection of the bridge at the front wheel location in the $(j-1)^{\text{th}}$ iteration and $(j)^{\text{th}}$ iteration respectively; $w_2(x,t)_{j-1}$, $w_2(x,t)_j$ are the deflection of the bridge at the rear wheel location in the $(j-1)^{\text{th}}$ iteration and the $(j)^{\text{th}}$ iteration respectively.

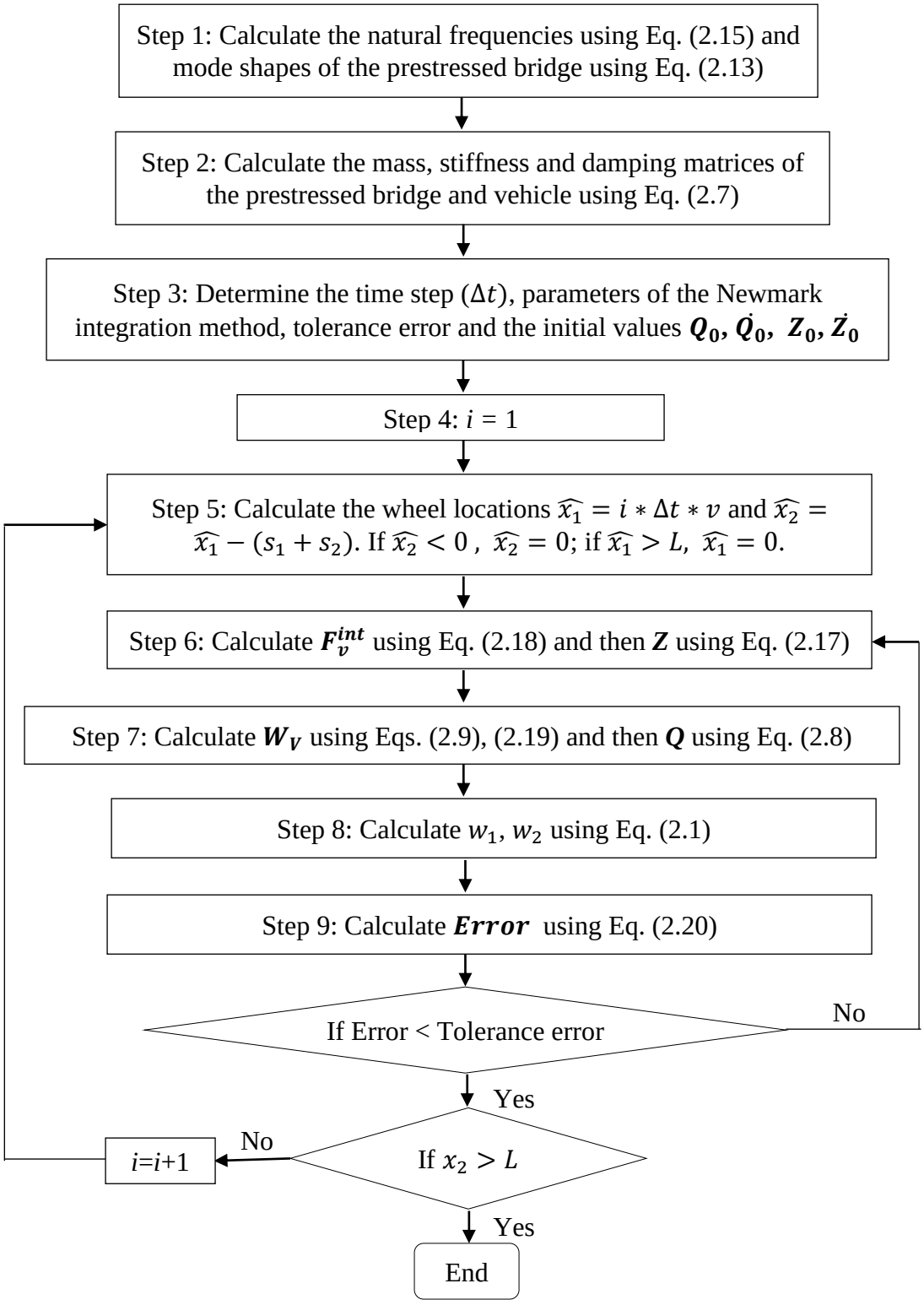

Fig. 2.3. Flow chart of implementation

2.4.2. Verification

To verify the theory proposed in Section 2.3, the initial deflection of a two-span continuous eccentrically-prestressed beam shown in Fig. 2.1 will be calculated by Eq. (2.10) and compared to the theoretical result calculated using the Timoshenko's theory [17]. The parameters used in the calculation are listed in Table 2.1. The comparison shown in Fig. 2.4 indicates that the proposed theory is accurate.

Table 2.1. Parameters of a two-span eccentrically-prestressed beam

Young's modulus (GPa)	32	Span length (m)	18+18
Cross-sectional area (m^2)	0.76	Prestress force (kN)	3.113×10^3
Moment of inertia (m^4)	0.1014	Initial moment (kN·m)	1.058×10^3
Mass of per unit volume (kg/m^3)	2700		

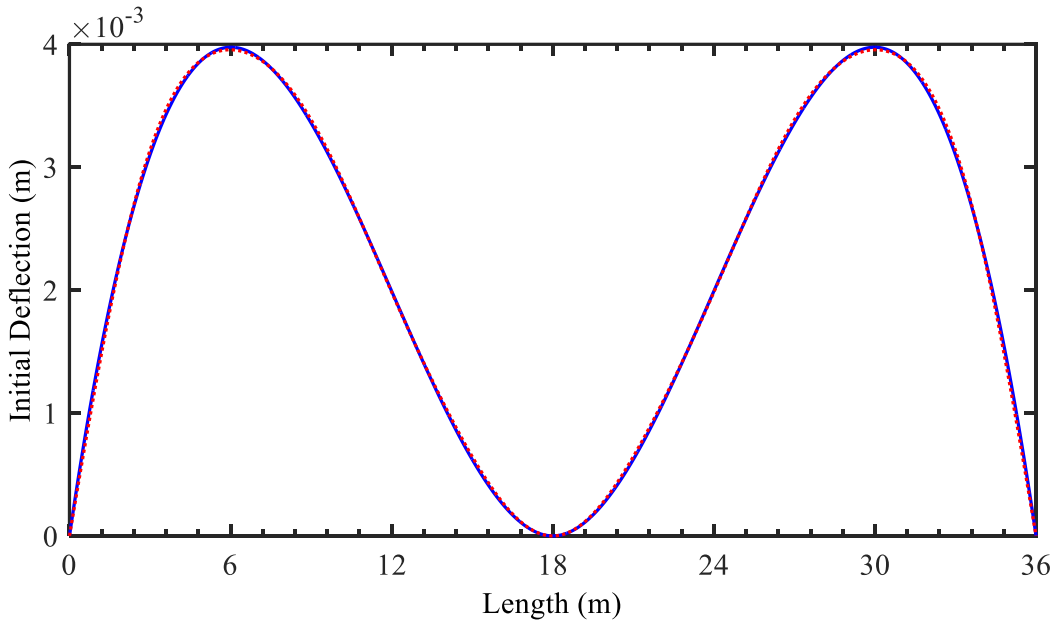

Fig. 2.4. Initial deflection of a two-span continuous eccentrically-prestressed beam
Present study; ····· Ref. [17]

Natural frequencies of some simply-supported single-span and two-span continuous beams with or without prestress force are shown in Table 2.2. These beams have the same properties as that shown in Table 2.1. There are no exact theoretical results for natural

frequencies of prestressed continuous beams, so the numerical results from Abaqus model is used for comparison. As shown in Table 2.2, the proposed method in Section 2.3 can get very close results compared to the results obtained in Ref. [18], [19] and the numerical results derived through Abaqus, which further verifies the correctness of the developed prestressed bridge model. Note that the prestress has little influence on the natural frequencies of the bridge which might be able to explain the inefficiency of frequency-based methods [20] in evaluating prestress. It needs to point out the Abaqus model adopted here is through a two-stage analysis with the first step to apply the prestress effect in the form of an axial force and the second step to perform the modal analysis and obtain its natural frequencies. The element type used is the 2-node B33 element.

No published results on dynamic response of eccentrically prestressed beams under moving vehicle load has been found, thus two cases in Ref. [6] and [21] will be used instead to verify the numerical algorithm presented in the previous section. In Ref. [6], the bridge-vehicle model shown in Fig. 2.5 was adopted, and the following parameters for the model were used: EI = 1.27×10^{11} N·m^2, ζ_b = 0.02, ρ = 12000 kg/m, L = 40 m, m_v = 76800 kg, k_v = 3.1×10^7 N/m, c_v = 1.54×10^5 kg/sec, V = 25.6 m/sec, where EI is the flexural rigidity of the bridge, ζ_b is the damping ratio of the bridge, ρ is the mass per unit length of the bridge, L is span length, m_v is mass of vehicle, k_v is spring stiffness, c_v is dashpot coefficient and V is the speed of the vehicle. As can be seen in Fig. 2.6, the obtained results are in excellent agreement with the results of Ref. [6].

Table 2.2. Natural frequencies of beams (Hz)

Mode	Single-span (L = 18 m)				Two-span continuous beam (L = 2×18 m)				
	Ref.[18]		Present study		Ref.[19]	Abaqus model		Present study	
	P (×10^3 kN)		P (×10^3 kN)		P	P (×10^3 kN)		P (×10^3 kN)	
	0	3.113	0	3.113	0	0	3.113	0	3.113
1	6.10	6.00	6.10	6.00	6.18	6.10	6.00	6.10	6.00
2	24.39	24.29	24.39	24.29	9.65	9.52	9.45	9.53	9.46
3	54.87	54.77	54.87	54.77	24.71	24.39	24.29	24.39	24.29
4	97.54	97.45	97.54	97.45	31.27	30.86	30.78	30.90	30.82
5	152.41	152.32	152.41	152.32	55.59	54.87	54.77	54.87	54.77
6	219.47	219.38	219.47	219.38	65.25	64.39	64.31	64.57	64.49
7	298.73	298.63	298.73	298.63	98.83	97.54	97.45	97.54	97.45
8	390.18	390.08	390.18	390.08	111.57	110.12	110.03	110.64	110.55
9	493.82	493.72	493.82	493.72	154.43	152.41	152.32	152.41	152.32
10	609.65	609.55	609.65	609.55	170.26	168.04	167.95	169.29	169.20

Note: Ref. [18] uses an analytical method to solve differential equations and derive natural frequencies; Ref. [19] utilizes a finite element method to obtain the natural frequencies.

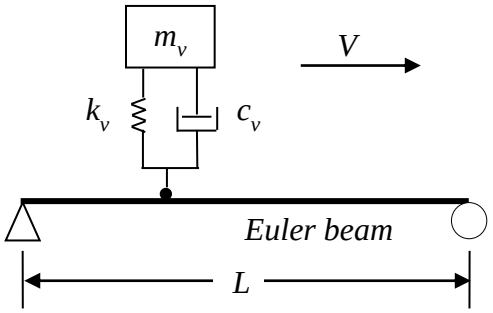

Fig. 2.5. The bridge-vehicle model adopted in Ref. [6]

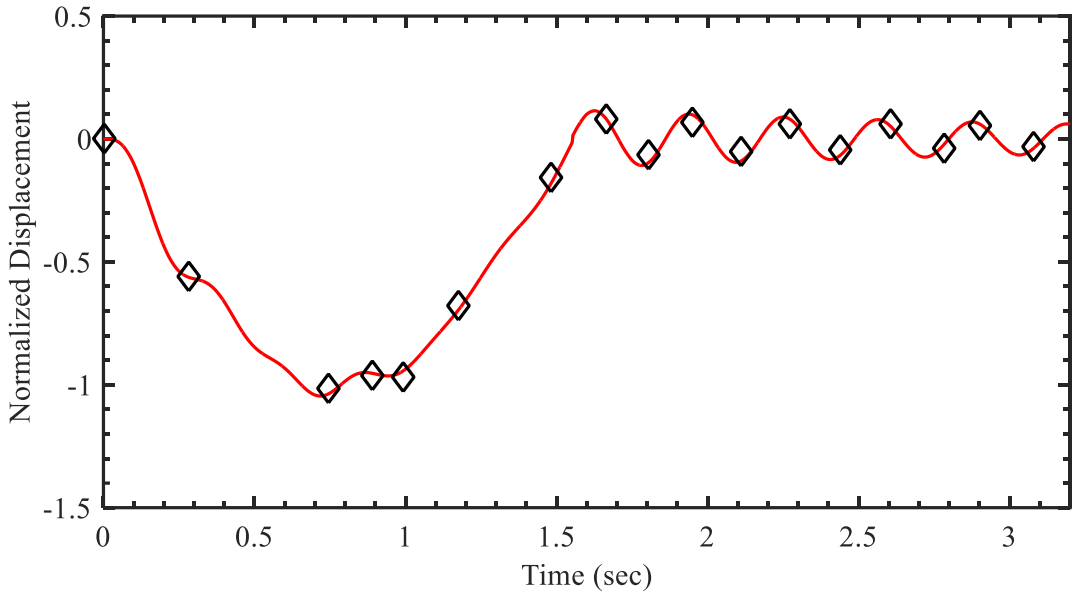

Fig. 2.6. Comparison of mid-span bridge deflection
Present study; ◊ Ref. [6].

A bridge-vehicle model consisting of a simple beam subjected to a moving rigid bar supported by spring–dashpot units shown in Fig. 2.7 was used in Ref. [21]. The properties of the beam are: length L = 30 m, modulus of elasticity E = 2.94×10^7 kN/m^2, Poisson's ration υ = 0.2, moment of inertia I = 8.65 m^4, mass per length m = 3.60×10^4 kg/m, damping ratio ξ = 0, and cross-sectional area A = 5.16 m^2. The following data for the vehicle are used: rigid bar mass M_v = 5.40×10^5 kg, mass moment of inertia I_v =1.38×10^7 kg·m^2, spring stiffness k_v = 41,350 kN/m, dashpot coefficient c_v = 0, wheel mass M_w = 0 kg, wheel-to-wheel distance d = 17.5 m, and the vehicle speed v = 27.78 m/s.

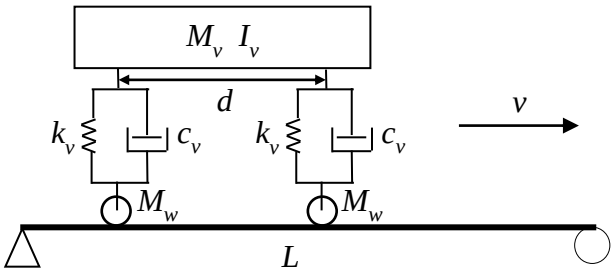

Fig. 2.7. The bridge-vehicle model adopted in Ref. [21]

The comparison of midpoint displacement of the beam and vertical acceleration of rigid bar for the present study and Ref. [21] are shown in Figs. 2.8 and 2.9, respectively. As can be seen, good agreements have been achieved.

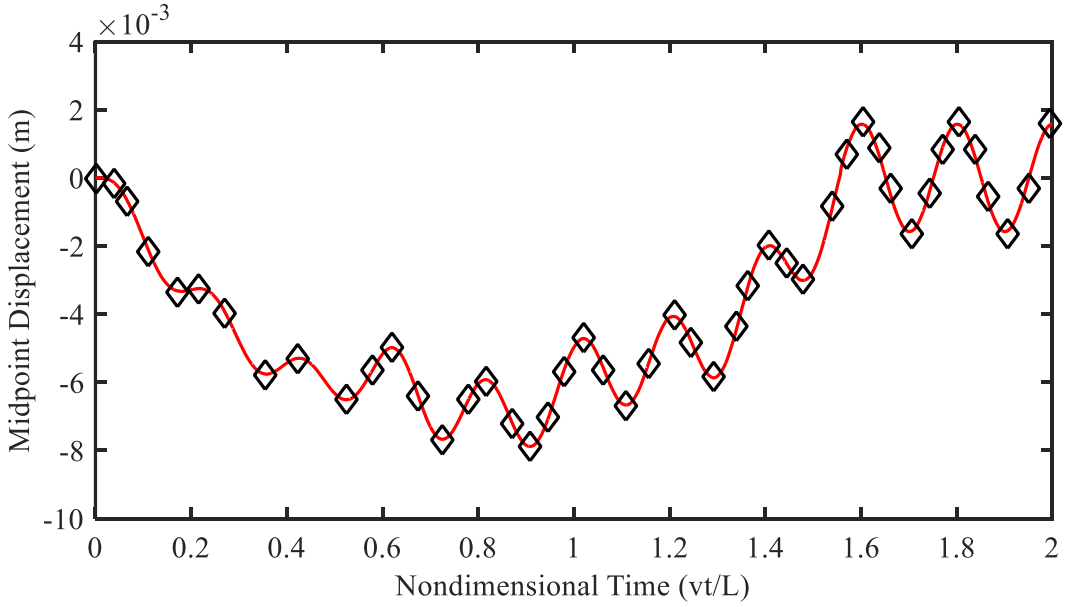

Fig. 2.8. Comparison of midpoint displacement of a simple beam
Present study; ◊ Ref. [21].

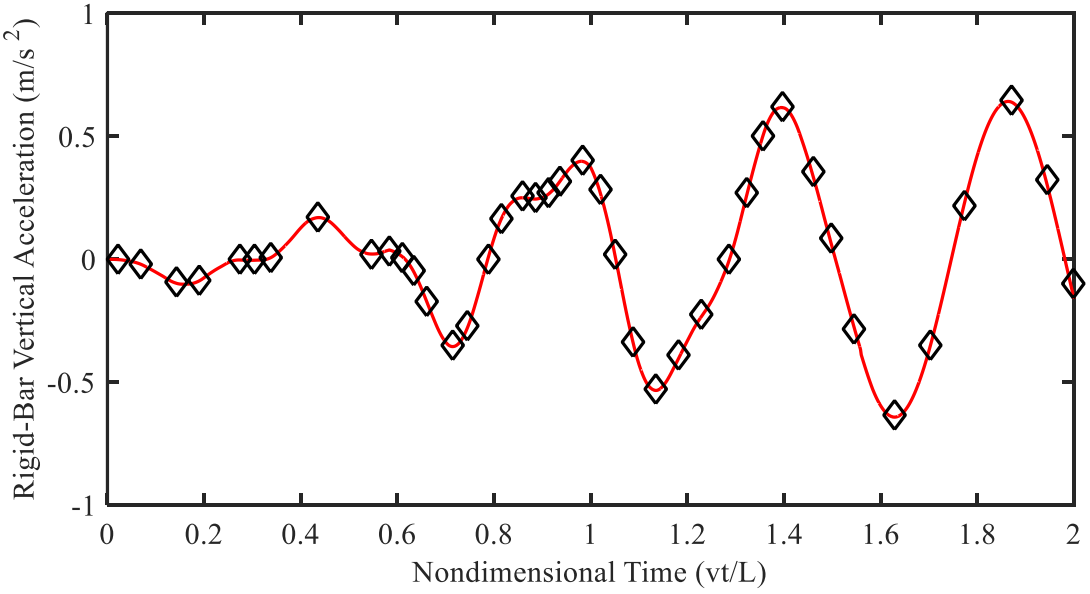

Fig. 2.9. Comparison of vertical acceleration of the rigid bar
Present study; ◊ Ref. [21].

2.4.3. Parametric Study

To determine the effect of parameters such as vehicle speed, span number, span length, eccentricity and amplitude of prestress on dynamic responses of the prestressed bridge and the passing vehicle, numerical simulations were conducted using the bridge and vehicle model as described in the previous sections. In these parametric studies, the properties of the bridge are the same as those in Table 2.1, except in the study of effect of span length where bridges with different span length will have different properties. The parameters for the vehicle in Maechesiello [22] are used in the simulations with some of them modified to accommodate the half vehicle model and listed as following: m_c = 8500 kg, I_c = 4.5×10^4 kg·m^2, m_f = 300 kg, m_r= 500 kg, k_{s1} = 1.16×10^5 N/m, k_{s2} = 3.73×10^5 N/m, k_{t1} = 7.85×10^5 N/m, k_{t2} = 1.57×10^6 N/m, c_{s1} = 2.5×10^4 N·sec/m, c_{s2} = 3.5×10^4 N·sec/m, c_{t1} = 100 N·sec/m, c_{t2} = 200 N·sec/m.

In this study, a program was coded in Matlab to compute the bridge and vehicle responses using the Newmark integration method with γ = 0.5 and β = 0.25, which implies a constant average acceleration over a time step with unconditional stability. The first 10 mode shapes of the bridge were used in the calculation and a time step of 0.00005 sec was selected. The tolerance error between two consecutive iterations was 1%. To focus on the prestress effect, the surface of the bridge pavement was assumed to be smooth implying no road roughness and smooth entrance and exit to the bridge were also assumed to keep the problem traceable.

2.4.3.1. Effect of span number of the bridge

Time histories of the displacement at the middle of the first span of the single-span, two-span, and three-span prestressed bridges under the vehicle speed of 20m/s are plotted in Fig. 2.10(a), with the vertical acceleration of the vehicle plotted in Fig. 2.10(b). Note that each single span of the bridges has the same length of 18 meters and shares the same properties including the

amount of prestress force and initial moment. As can be seen, the maximum displacement and vehicle vertical acceleration for the case of single-span bridges are obviously greater than that for the cases of two-span and three-span bridges. Fig. 2.10(c) shows the impact factors of the bridges under four different driving speeds. The impact factor is defined as following:

$$I_p = \left(\frac{D_d}{D_s} - 1\right) \times 100\% \tag{2.21}$$

where D_d and D_s are the maximum dynamic and static displacement of the bridge at the first span mid-point due to the vehicle respectively. Here D_s can be readily obtained by assuming $\dot{\boldsymbol{Q}}_{\boldsymbol{0}} = \ddot{\boldsymbol{Q}}_{\boldsymbol{0}} = [\boldsymbol{0}]_{\boldsymbol{N}\times\boldsymbol{1}}$ and then solving Eq. (2.8). It should be noted that this approach is much easier and more straightforward than the existing method assuming a very slow vehicle speed and then solving the dynamic bridge-vehicle interaction response. As shown in Fig. 2.10(c), the impact factor for the three-span continuous bridge varies little with the speed and is much smaller than these of the other two bridges at high speed (30-40 m/s).

The comparison of maximum vehicle vertical acceleration for the three bridges is shown in Fig. 2.10(d). As can be seen, the maximum vehicle accelerations for the single-span bridge are apparently larger than those for two-span and three-span continuous bridges. The reason for that can be that the single-span bridge has the smallest stiffness among these three bridges and thus have the largest vibration amplitude under the vehicle load, which leads for the vehicle to possess the largest vibration amplitude at the same time.

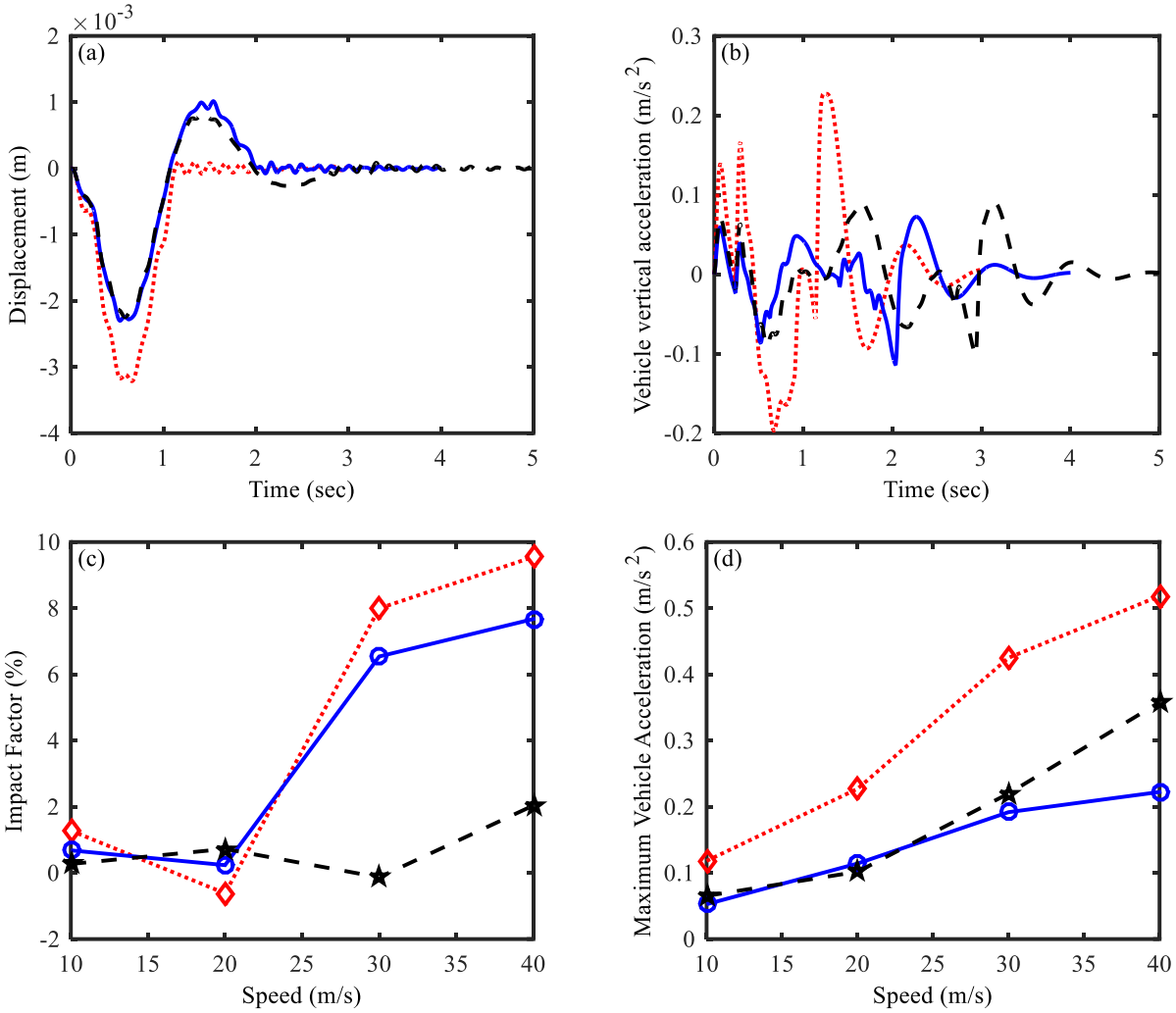

Fig. 2.10. Comparison of bridge and vehicle responses for different number of spans (a) Bridge displacement at the middle of the first span; (b) Vertical acceleration of the vehicle; (c) Impact factors for the bridge displacement; (d) Maximum vehicle vertical acceleration.
Single span; Two spans; Three spans.
Single span; Two spans; Three spans.

2.4.3.2. Effect of the prestress force

To investigate the effect of the prestress force on the bridge and vehicle responses, a range of percentage of practical prestress from 30% to 140% has been applied to a two-span continuous bridge, including the non-prestress case (0%) for comparison. Note that the eccentricity of the prestress is kept constant, implying the initial moment will change with the

prestress at the same rate. The other properties of the bridge are kept the same as those in Table 2.1.

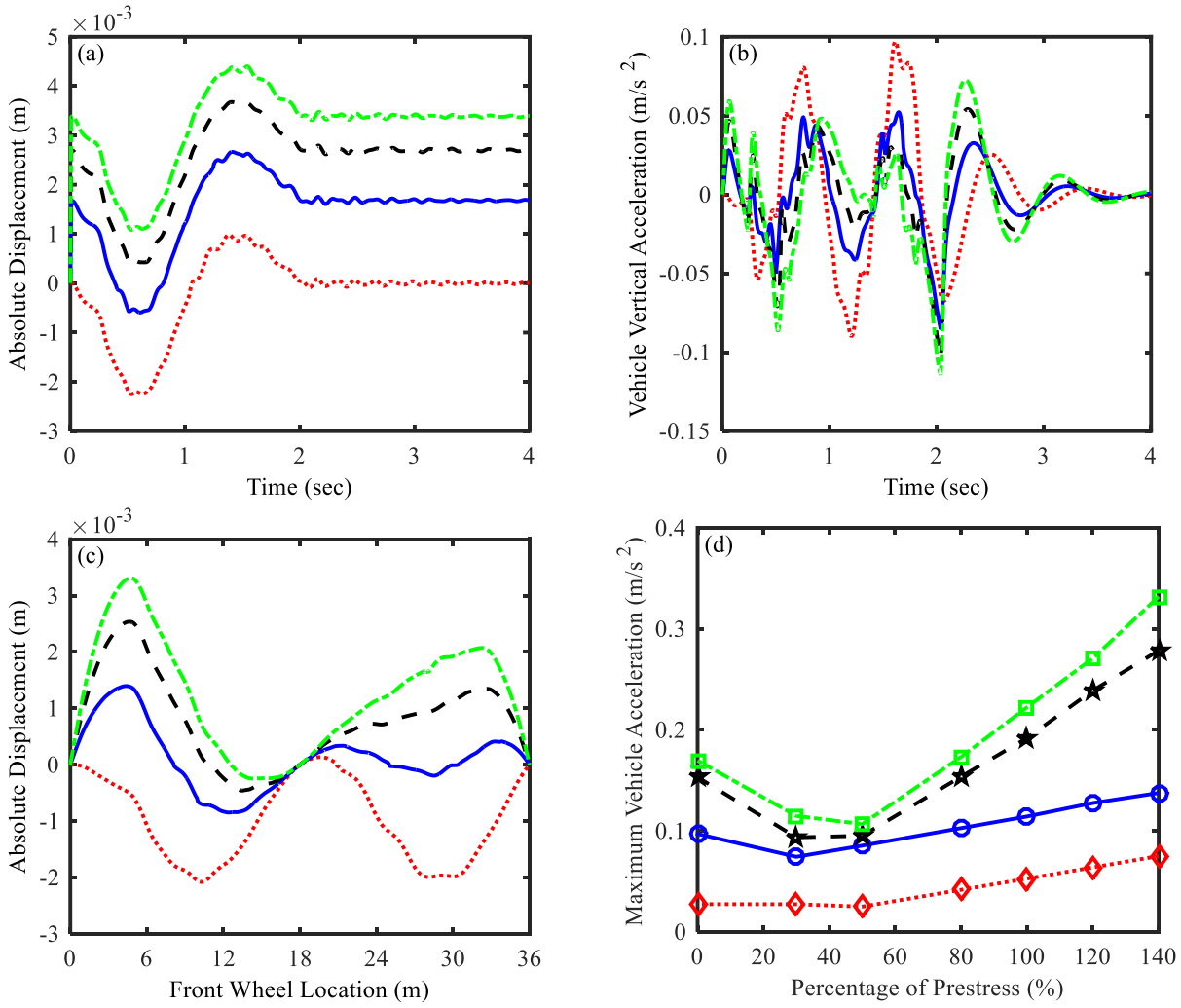

Fig. 2.11. Comparison of bridge and vehicle responses for different prestress forces
(a) Absolute displacement at the middle of the first span; (b) Vertical acceleration of the vehicle;
(c) Absolute displacement of the bridge at the front wheel location;
(d) Maximum vertical acceleration of the vehicle.
P - 0%; P - 50%; P - 80%; P - 100%.
10 m/s; 20 m/s; 30 m/s; 40 m/s.

Fig. 2.11(a) shows the time histories of absolute displacements of the bridge at the middle of the first span for 0%, 50%, 80%, and 100% of practical prestress under the vehicle speed of 20m/s. Here, the absolute displacement means that it was measured from the horizontal line through the supports, and for all the other displacements appearing in this paper, they were

relative displacements measured from the static equilibrium position of the bridge. From Fig. 2.11(a), one observes that they share very similar trends with nearly the same amplitude of variability, which implies the prestress has little effect on the bridge relative displacement.

Time histories of the vertical accelerations of the vehicle traveling over the bridge at the speed of 20 m/s with different percentages of practical prestress have been plotted in Fig. 2.11(b). As can be seen, similar trends with different amplitudes appeared for the vehicles passing the prestressed bridges (50%, 80% and 100%), while the trend for the vehicle passing the non-prestressed bridge is very different. The reason for that may be seen from Fig. 2.11(c) which shows the displacement of the bridge at the front wheel location when the vehicle was passing the bridge at 20 m/s.

As shown in Fig. 2.11(c), the trace of the front wheel passing the non-prestressed bridge consists of two nearly symmetric down-wards bumps. In contrast, the traces of the front wheel passing the prestressed bridges are composed of two asymmetric up-wards bumps. Thus, a conclusion can be drawn from Fig. 2.11(c) that the prestress force greatly changes the performance of the bridge under moving vehicles.

Moreover, to some extent, Fig. 2.11(c) may be used to explain the results shown in Fig. 2.11(d). Fig. 2.11(d) shows the maximum vertical acceleration of the vehicle under different levels of prestress. With the increase of the percentage of prestress from 0% to 140%, the maximum vertical acceleration of the vehicle will decrease first and then increase, and specially increases almost linearly when the percentage of prestress increases from 50% to 140%, corresponding to the increasing height of the bumps in Fig. 2.11(c) from 50% to 100%. For the same travelling distance and speed, the higher bump as shown in Fig. 2.11(c) is, the larger acceleration as shown in Fig. 2.11(d) will be, which consists with the common sense of life that

stiffer slope leads to stronger vibration of the vehicle. Meanwhile, the speed of the vehicle plays an important role in the variation of its maximum acceleration. Generally, the higher the speed is, the larger the maximum acceleration is.

2.4.3.3. Effect of the eccentricity

In the previous section, the effect of the prestress force has been studied with the eccentricity kept constant. Actually, the eccentricity is also an important component of the prestress in practical. Therefore, there is a need to investigate its effort.

Firstly, keeping the initial moment constant ($M_o = S \cdot e$), three cases are studied: (2.0*S*, 0.5*e*), (1.0*S*, 1.0*e*) and (0.5*S*, 2.0*e*), where *S* represents the amount of prestress force in practice and *e* is the eccentricity of the prestress in practice. The comparison of initial deflection of the bridge, time histories of the displacement at the middle of the first span and vertical acceleration of the vehicle are plotted in Figs. 2.12(a)-(c), respectively. As can be seen, three lines representing three cases are very close to each other, indicating little difference among three cases.

Fig. 2.12(d) shows the comparison of maximum vertical acceleration of the vehicle for two series of cases: one case with *e* fixed but *S* changing from 0% to 140% and the other with *S* fixed but *e* changing from 0% to 140%. As shown in Fig. 2.12(d), with the same initial moment, two cases nearly possess the same amount of maximum vehicle acceleration.

Thus, a general conclusion can be obtained that the change of eccentricity has the same effect as the change of prestress and the initial moment is a controlling factor of bridge-vehicle interaction response.

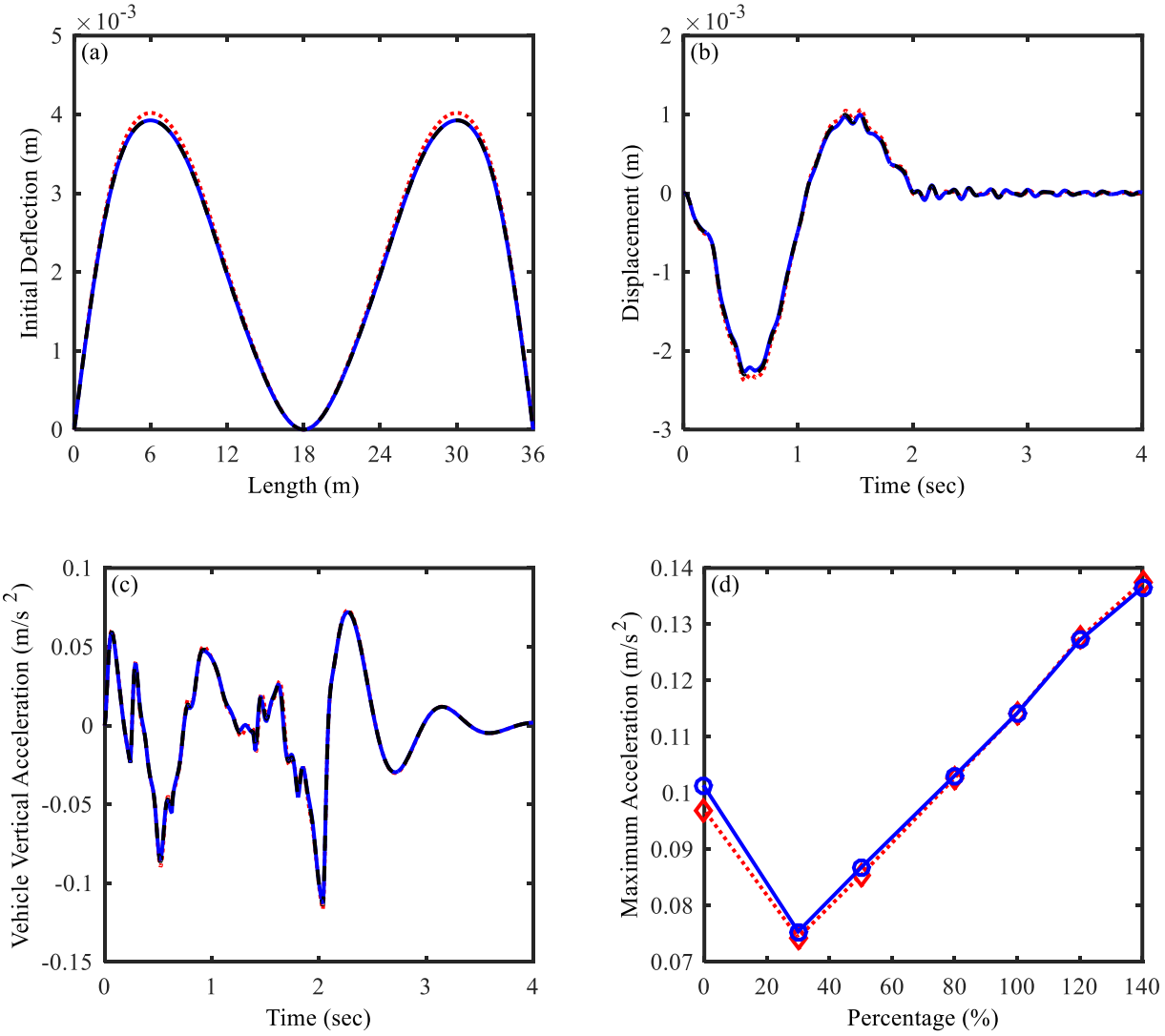

Fig. 2.12. Comparison of bridge and vehicle responses for different combinations of prestress force and eccentricity
(a) Initial deflection of the bridge; (b) Displacement at the middle of the first span.
(c) Vertical acceleration of the vehicle; (d) Maximum vertical acceleration of the vehicle.
(2.0*P*, 0.5*e*); (1.0*P*, 1.0*e*); (0.5*P*, 2.0*e*).
Prestress force; Eccentricity.

2.4.3.4. Effect of span length

As found in Section 2.4.3.2, the maximum vehicle acceleration increases almost linearly when the percentage of prestress increases from 50% to 140% for the bridge with span length

(18m+18m). It is essential to check whether this phenomenon happens on the other span length bridges.

In this section, another two continuous bridges with span length (11m+11m) and (30m+30m) have been studied. Their different properties are shown in Table 2.3.

Table 2.3. Properties of three two-span continuous bridges

Properties	Span length (m)		
	11+11	18+18	30+30
Moment of inertia (m^4)	0.0444	0.1014	0.3565
Cross-sectional area (m^2)	0.69	0.76	1.05
Mass of per unit length (kg/m)	1858	2052	2834
Prestress force (kN)	2.002×10^3	3.113×10^3	5.337×10^3
Initial moment (kN·m)	5.084×10^2	1.058×10^3	3.736×10^3

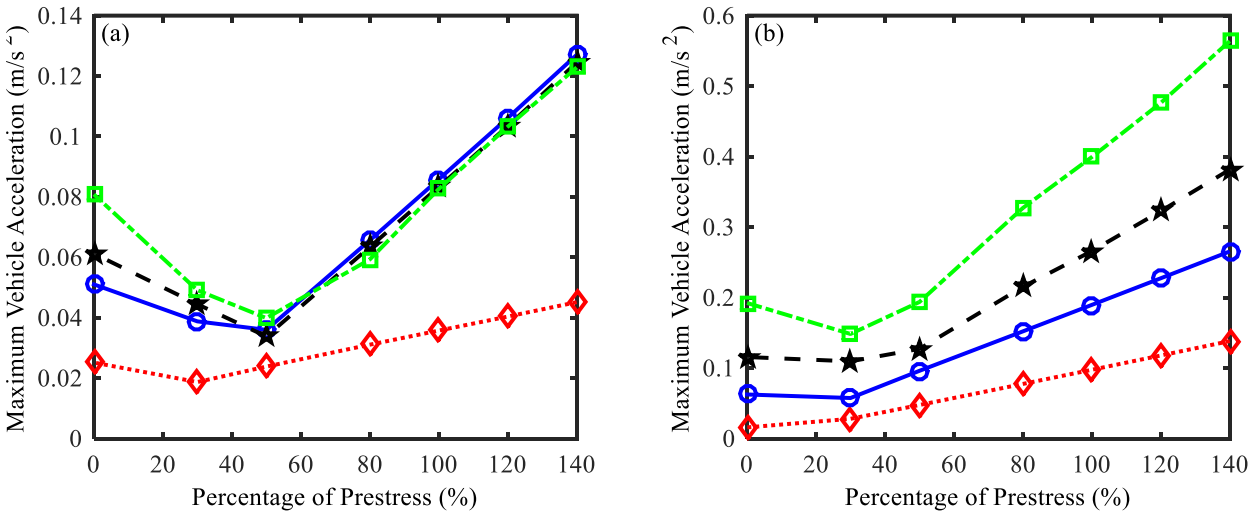

Fig. 2.13. Maximum vehicle vertical acceleration for different span lengths at four speeds (a) Span length (11m+11m); (b) Span length (30m+30m). 10 m/s; 20 m/s; 30 m/s; 40 m/s.

Figs. 2.13 (a) and (b) show the maximum vertical acceleration of the vehicle for span length (11m+11m) and (30m+30m), respectively. As can be seen, the same phenomenon happens that the maximum vehicle acceleration increases linearly when the percentage of

prestress increases from 50% to 140%. Specially, for the short-span bridge (11m+11m), maximum acceleration becomes insensitive to the speed from 20 m/s to above, of which the cause can be that the short bridge does not have enough time to vibrate under the high speed vehicle.

Yang et al. [23] proposed a method of measuring bridge frequencies through the analysis of the dynamic responses of a passing vehicle, which enlighten the authors that the maximum vertical acceleration of vehicles might be a good index for detecting the change of prestress of the bridge.

2.4.3.5. Effect of multiple vehicles

In practice, there are often multiple vehicles traveling over the bridge. Thus, it is important to know the performance of the bridge under multiple moving vehicles. Consider the bridge with a modest traffic flow, a 10.0 m following distance is assumed to include multiple vehicles on the bridge. Fig. 2.14(a) shows the model of multiple vehicles passing the bridge; Fig. 2.14(b) shows time histories of mid-span displacement of the bridge. As can be seen from Fig. 2.14(b), there is no big difference between the bridge response due to single vehicle and these due to multiple vehicles. It is interesting to find that the number of peaks of the curve in Fig. 2.14(b) is equal to the number of vehicles.

The maximum vehicle vertical accelerations are summarized in Table 2.4. One observation obtained from Table 2.4 is that the later-entering vehicle will significantly decrease the maximum vertical acceleration of the vehicle ahead of it, which mainly attributes to the suppression of the initial curvature of the prestressed bridge due to the later entered vehicles.

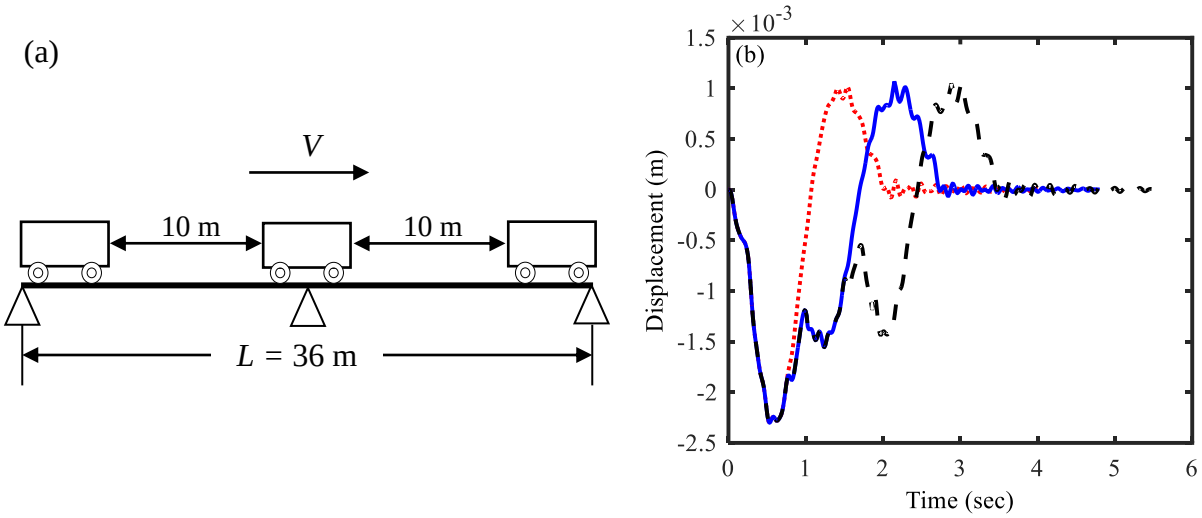

Fig. 2.14. Multiple vehicles traveling over the bridge
(a) Schematic of multiple vehicles passing the bridge;
(b) Bridge displacements at the middle of the first span.
····· One vehicle; ——— Two vehicles; – – – – Three vehicles.

Table 2.4. Maximum vertical acceleration of vehicles

Speed (m/s)	Number of vehicles	Maximum vehicle acceleration (m/s^2)		
		First vehicle	Second vehicle	Third vehicle
10	1	0.0527		
	2	0.0457	0.0528	
	3	0.0495	0.0437	0.0528
20	1	0.1142		
	2	0.0865	0.1100	
	3	0.0865	0.0689	0.1105
30	1	0.1918		
	2	0.1443	0.2055	
	3	0.1604	0.1791	0.2009
40	1	0.2223		
	2	0.1876	0.2125	
	3	0.2205	0.1779	0.2170

2.5. Summary

In this chapter, a new bridge-vehicle model with consideration of prestress effect is created through the principle of virtual works to address the prestressed continuous bridges and vehicle interaction. The correctness and accuracy of the current model are validated with the theoretical results in literature, results from the Abaqus model created in this chapter, and the existing published results. Based on the created model, numerical simulations have been conducted to perform a parametric study on effects of span number, level of prestress, eccentricity of prestress, span length, and presence of multiple vehicles.

Several conclusions were reached.

- The prestress has little influence on the natural frequencies of the bridge which might be able to explain the inefficiency of frequency-based methods in evaluating prestress.
- Impact factor for the three-span prestressed bridge varies little with the speed and is much smaller than that of single-span and two-span prestressed bridges at the high speed (30-40 m/s).
- Maximum vehicle vertical accelerations for the single-span prestressed bridge are apparently larger than those for the multiple-span prestressed bridges.
- Prestress has a significant effect on the maximum vertical acceleration of vehicles, which may provide a good index for detecting the change of prestress.
- Eccentricity is an important component of the prestress in the bridge and the initial moment induced is a controlling factor of the bridge-vehicle interaction response.
- The later-entered vehicle on the prestressed bridge will largely reduce the maximum vertical acceleration of the vehicles ahead of it.

2.6. References

[1] Pandey, A. K., Biswas, M., & Samman, M. M. (1991). Damage detection from changes in curvature mode shapes. *Journal of sound and vibration*, *145*(2), 321-332.

[2] Dilena, M., & Morassi, A. (2010). Reconstruction method for damage detection in beams based on natural frequency and antiresonant frequency measurements. *Journal of engineering mechanics*, *136*(3), 329-344.

[3] Lan, C., Zhou, Z., & Ou, J. (2012). Full-scale prestress loss monitoring of damaged RC structures using distributed optical fiber sensing technology. *Sensors*, *12*(5), 5380-5394.

[4] Zhu, X. Q., & Law, S. S. (2002). Dynamic load on continuous multi-lane bridge deck from moving vehicles. *Journal of Sound and Vibration*, *251*(4), 697-716.

[5] Yang, M., & Papagiannakis, A. T. (2010). A coupled honeycomb composite sandwich bridge-vehicle interaction model. *Journal of Mechanics of Materials and Structures*, *5*(4), 617-635.

[6] Green, M. F., & Cebon, D. (1997). Dynamic interaction between heavy vehicles and highway bridges. *Computers & structures*, *62*(2), 253-264.

[7] Kocatürk, T., & Şimşek, M. (2006). Vibration of viscoelastic beams subjected to an eccentric compressive force and a concentrated moving harmonic force. *Journal of Sound and Vibration*, *291*(1), 302-322.

[8] Van Khang, N., Dien, N. P., & Van Huong, N. T. (2009). Transverse vibrations of prestressed continuous beams on rigid supports under the action of moving bodies. *Archive of Applied Mechanics*, *79*(10), 939-953.

[9] Deng, L., & Cai, C. S. (2010). Development of dynamic impact factor for performance evaluation of existing multi-girder concrete bridges. *Engineering Structures*, *32*(1), 21-31.

[10] Deng, L., & Cai, C. S. (2009). Identification of parameters of vehicles moving on bridges. *Engineering Structures*, *31*(10), 2474-2485.

[11] Chen, S. R., & Wu, J. (2009). Dynamic performance simulation of long-span bridge under combined loads of stochastic traffic and wind. *Journal of Bridge Engineering*, *15*(3), 219-230.

[12] Cai, C. S., Shi, X. M., Araujo, M., & Chen, S. R. (2007). Effect of approach span condition on vehicle-induced dynamic response of slab-on-girder road bridges. *Engineering Structures*, *29*(12), 3210-3226.

[13] Humar, J. L. (1990). Dynamics of structures, Prentice-Hall Inc, New Jersey.

[14] Zhou, D. (1994). Eigenfrequencies of line supported rectangular plates. *International Journal of Solids and Structures*, *31*(3), 347-358.

[15] Jazar, R. N. (2008). Vehicle dynamics: theory and application, Springer Science+Business Media, New York.

[16] Newmark, N. M. (1959). A method of computation for structural dynamics. *Journal of the engineering mechanics division*, *85*(3), 67-94.

[17] Timoshenko, S. (1961). Theory of elastic stability, McGRAW-HILL Book Company, New York And London.

[18] Shaker, F. J. (1975). Effect of axial load on mode shapes and frequencies of beams. NASA Technical Note, Lewis Research Center.

[19] Hayashikawa, T., & Watanabe, N. (1985). Free vibration analysis of continuous beams. *Journal of engineering mechanics*, *111*(5), 639-652.

[20] Kim, J. T., Yun, C. B., Ryu, Y. S., & Cho, H. M. (2004). Identification of prestress-loss in PSC beams using modal information. *Structural Engineering and Mechanics*, *17*(3-4), 467-482.

[21] Yang, Y. B., & Wu, Y. S. (2001). A versatile element for analyzing vehicle–bridge interaction response. *Engineering structures*, *23*(5), 452-469.

[22] Marchesiello, S., Fasana, A., Garibaldi, L., & Piombo, B. A. D. (1999). Dynamics of multi-span continuous straight bridges subject to multi-degrees of freedom moving vehicle excitation. *Journal of Sound and Vibration*, *224*(3), 541-561.

[23] Yang, Y. B., Lin, C. W., & Yau, J. D. (2004). Extracting bridge frequencies from the dynamic response of a passing vehicle. *Journal of Sound and Vibration*, *272*(3), 471-493.

CHAPTER 3. DYNAMIC EFFECT OF FOUNDATION SETTLEMENT ON BRIDGE-VEHICLE INTERACTION

3.1. Abstract

Foundation settlement is a common issue for bridges, which not only generates additional static stresses in continuous bridge members but also may affect the dynamic interaction between the bridge and vehicle traveling over it. In this chapter, a new bridge-vehicle model with consideration of foundation settlement effect is created through the principle of virtual works to investigate the settled bridge and vehicle interaction responses. The correctness and accuracy of the model are validated with theoretical and numerical results. Based on the proposed model, numerical simulations have been conducted using the Newmark's β method to investigate the effects of settlement mode, vehicle traveling speed, road surface roughness, and boundary condition. It is shown that foundation settlement has a significant effect on impact factors of the bridge at high vehicle speeds, and road surface roughness may work together with the settlement to have a coupling effect, which needs special attentions.

3.2. Introduction

Like other structures, a bridge may experience foundation settlements in its lifetime, which could occur at the abutments or piers of the bridge due to the compaction or consolidation of the bearing soil under the weight of the structure, high traffic load, and the scour, etc. Since the settlement might cause serviceability issues and potential structural damage, it has been noticed and studied for a long time.

Grover [1] reported that 90% of the 68 bridges studied in 1961 suffered abutment settlements and 80% had settlements of larger than 1 inch (25.4 mm) up to 4 inches (101.6 mm). In 1975, Walkinshaw [2] did a survey on 35 bridges from 10 western states and found that large

settlements may be tolerable from a structural view of point but may lead to a poor riding quality once exceeding 2.5 inches (63.5 mm). Moulton et al. [3] conducted a comprehensive study on foundation movements of 314 bridges in U.S. and Canada and suggested a tolerable angular distortion (differential settlement/span length) of 0.4% for continuous bridges and 0.5% for simply-supported in 1985. AASHTO [4] adopts similar tolerable criteria for highway bridge settlement, angular distortions less than 0.004 and 0.008 for continuous and simple span bridges respectively. Schopen [5] and Wang et al. [6] did refined settlement analysis on more rent bridges than Moulton et al. [3] and got similar conclusions that moment induced by differential settlements can be as high as that due to dead and live loads alone, and strengthening the bridge superstructures to tolerate the settlement may be more economical than limiting the foundation not to move. However, the preceding findings and criteria are mostly based on static and probabilistic analysis, with little consideration on dynamic effect of foundation settlement.

Due to the significant increase of heavy and high-speed traffics, bridge-vehicle interaction has gained increasingly attention in recent decades and been studied by many researchers [7-21]. Au et al. [22] investigated the effects of deck surface roughness and long-term deflection of bridges on impact factors due to moving vehicles. Yin et al. [23] studied the lateral vibration of high-pier bridge under moving vehicular loads. Zhong et al. [24] analyzed the effect of prestress on bridge vehicle interaction responses. Cai et al. [25], Zhang et al. [26,27] researched the effect of approach span settlement on dynamic behaviors of bridge and vehicle. Ahmari et al. [28] carried out dynamic analysis of a three-span continuous bridge with different support settlement scenarios. In reality, bridges may be subjected to road surface roughness and foundation settlements simultaneously, which has not been studied in previous works.

In this chapter, road surface roughness and foundation settlement have been incorporated into the bridge-vehicle interaction model through the principle of virtual works. The created model was first validated with theoretical and numerical results, and then used to compute the dynamic responses of the bridge and vehicle using Newmark's β method. Effects of settlement mode, vehicle traveling speed, road surface roughness and boundary condition were analyzed and discussed. It is anticipated that results given in this paper will help quantifying the settlement limit of the bridge in future.

3.3. Theory Background

3.3.1. Equation of Motion for the Bridge under Foundation Settlements

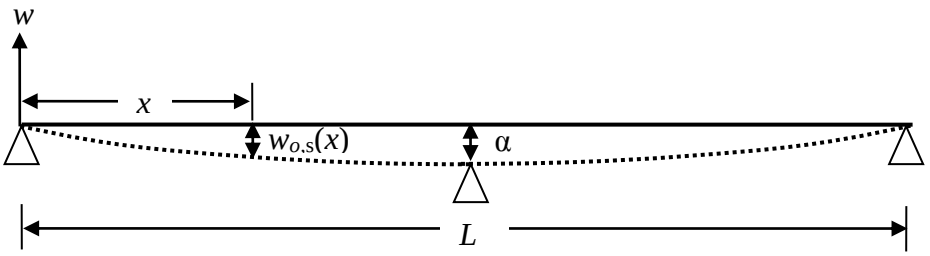

Fig. 3.1. Schematic of a continuous bridge with central pier settlement

As shown in Fig. 1, a two-span continuous bridge subjected to central pier settlement can be modeled as a continuous beam having displacement at the middle support.

Based on the modal superposition principle, the vertical deflection $w(x,t)$ of the beam with support settlement can be described as:

$$w(x,t) = \sum_{i=1}^{N} W_i(x)\, q_i(t) + w_{o,s}(x) \tag{3.1}$$

where $W_i(x)$, $q_i(t)$, N and $w_{o,s}(x)$ are the i^{th} mode shape function of the beam, the corresponding modal amplitude of the beam, the selected number of mode shapes and the initial deflection of the beam due to support settlement, respectively.

According to the principle of virtual displacement, the external virtual work δW_E is equal to the internal virtual work δW_I:

$$\delta W_E = \delta W_I \tag{3.2}$$

The virtual displacements $\delta q_i W_i(x)$, i=1,2,…,N are selected to be consistent with the assumed shape functions. The external virtual work is the sum of the works (δW_{in}, δW_{gL}, δW_V and δW_C) performed by the inertia force ($\bar{m}\frac{\partial^2 w}{\partial t^2}$), the gravity load ($\bar{m}g$), the moving vehicle load (F_b^{int}) and the damping force ($-c_{bi}\frac{\partial w}{\partial t}$), which can be written as,

$$\delta W_E = \delta W_{in} + \delta W_{gL} + \delta W_V + \delta W_C \tag{3.3}$$

where

$$\delta W_{in} = -\delta q_i \int_0^L W_i(x)\bar{m}\frac{\partial^2 w}{\partial t^2}dx$$

$$\delta W_{gL} = -\delta q_i \int_0^L \bar{m}gW_i(x)dx$$

$$\delta W_V = \delta q_i \int_0^L \sum_{k=1}^2 F_b^{int}(k)\,\delta[x-\widehat{x_k}(t)]W_i[\widehat{x_k}(t)]dx$$

$$\delta W_C = -\delta q_i \int_0^L c_{bi}(\frac{\partial w}{\partial t})W_i(x)dx \quad c_{bi} = 2\bar{m}\omega_i\zeta_i \tag{3.4}$$

and $\bar{m}$ is the mass of the beam per unit length; ω_i, ζ_i, c_{bi} is the natural frequency, damping ratio and damping coefficient for the i^{th} mode of the beam respectively; $F_b^{int}(k)$ is the k^{th} interaction force between the wheel of the vehicle and the bridge; $\widehat{x_k}(t)$ is the location of the k^{th} interaction force $F_b^{int}(k)$; $\delta(x)$ is the Dirac function; $W_i'(x)$ denotes the first derivative of $W_i(x)$ with respect to x; g is the acceleration of gravity.

The internal virtual work performed by the bending moment is:

$$\delta W_I = \delta q_i \int_0^L EI\left(\frac{\partial^2 w}{\partial x^2}\right)W_i''(x)dx \tag{3.5}$$

where EI is flexural rigidity of the beam; $W_i''(x)$ denotes the second derivative of $W_i(x)$ with respect to x.

Substituting Eq. (3.1) and Eqs. (3.3) ~ (3.5) into Eq. (3.2) and cancelling δq_i at both sides give

$$\sum_{j=1}^{N} \ddot{q}_j M_{bij} + \sum_{j=1}^{N} \dot{q}_j C_{bij} + \sum_{j=1}^{N} q_j K_{bij} = (W_V)_i + (W_{gL})_i + \left(W_{w_{o,s}}\right)_i \qquad (3.6)$$

where

$$M_{bij} = \int_0^L \bar{m} W_i(x) W_j(x) dx \qquad C_{bij} = \int_0^L c_{bi} W_i(x) W_j(x) dx$$

$$K_{bij} = \int_0^L EI W_i''(x) W_j''(x) dx \qquad (W_V)_i = \sum_{k=1}^{2} F_b^{int}(k)\, W_i\left(\widehat{x_k}(t)\right)$$

$$\left(W_{gL}\right)_i = -\int_0^L \bar{m} g W_i(x) dx \qquad \left(W_{w_{o,s}}\right)_i = -\int_0^L EI W_i''(x) w_{o,s}''(x) dx \qquad (3.7)$$

, $\dot{q}_j$ and $\ddot{q}_j$ denote the first and second derivative of $q_j(t)$ with respect to time *t*.

Corresponding to the N independent virtual displacements $\delta q_i W_i(x)$, *i*=1,2,…,N, there are N virtual work equations in the form of Eq. (3.6). Together they can be expressed in matrix form as:

$$\boldsymbol{M_b \ddot{Q} + C_b \dot{Q} + K_b Q = W_V + W_{gL} + W_{w_{o,s}}} \qquad (3.8)$$

where

$$\boldsymbol{Q} = \{q_1(t), q_2(t), \ldots, q_N(t)\}^T \qquad \boldsymbol{W_V} = W_b F_b^{int}$$

$$\boldsymbol{W_b} = \begin{bmatrix} W_1(\widehat{x_1}(t)) & W_1(\widehat{x_2}(t)) \\ \vdots & \\ W_N(\widehat{x_1}(t)) & W_N(\widehat{x_2}(t)) \end{bmatrix} \qquad \boldsymbol{F_b^{int}} = \begin{bmatrix} F_{t1} \\ F_{t2} \end{bmatrix}$$

$$\boldsymbol{W_{gL}} = \begin{Bmatrix} -\int_0^L \bar{m} g W_1(x) dx \\ \vdots \\ -\int_0^L \bar{m} g W_N(x) dx \end{Bmatrix} \qquad \boldsymbol{W_{w_{o,s}}} = \begin{Bmatrix} -\int_0^L EI w_{o,s}''(x) [W_1''(x)] dx \\ \vdots \\ -\int_0^L EI w_{o,s}''(x) [W_N''(x)] dx \end{Bmatrix} \qquad (3.9)$$

, $\boldsymbol{M_b}$, $\boldsymbol{C_b}$ and $\boldsymbol{K_b}$ are the mass, damping and stiffness matrices of the bridge respectively with their $(i, j)^{th}$ element calculated in Eq. (3.7); $\boldsymbol{\dot{Q}}$, $\boldsymbol{\ddot{Q}}$ are the first and second derivatives of $\boldsymbol{Q}$ with

respect to time t; F_{t1}, F_{t2} are the bridge-vehicle interaction forces at the front and rear wheel locations shown in Eq. (3.20). Actually, the term $W_{w_{o,s}}$ in Eq. (3.9) is zero-valued or equal to $[0]_{N\times 1}$, and the reason is that foundation settlement is not a kind of external force and thus will not create work on the beam, which has been verified by the authors through numerical calculations.

In practice, besides the deflection due to the support settlement $w_{o,s}(x)$, the continuous beam has an initial deflection $w_{o,g}(x)$ under its own self-weight or the gravity load before it vibrates under the moving load. In other words, the total initial static deflection of the bridge $w_o(x)$ is the superposition of the deflections due to the support settlement $w_{o,s}(x)$ and self-weight $w_{o,g}(x)$, which is described in Eq. (3.10). $w_{o,s}(x)$ can be obtained by solving the elastic beam differential equation, while the determination of $w_{o,g}(x)$ can be conducted in a mode-analysis way by using Eq. (3.11).

$$w_o(x) = w_{o,g}(x) + w_{o,s}(x) \tag{3.10}$$

$$K_b Q_0 = W_{gL} \qquad w_{o,g}(x) = W Q_0 \tag{3.11}$$

where

$$\boldsymbol{W} = \{W_1(x), W_2(x), \dots, W_N(x)\}$$

$$\boldsymbol{Q_0} = \{q_1(0), q_2(0), \dots, q_N(0)\}^T \tag{3.12}$$

3.3.2. Modal Analysis for the Bridge

For the free vibration of the beam, its vertical deflection can be expressed as:

$$w(x,t) = W(x)e^{i\omega t} \tag{3.13}$$

where ω is the natural frequency of the vibration and $i = \sqrt{-1}$.

The mode shape function of the beam $W(x)$ may be expressed in term of a series as:

$$W(x) = \sum_m A_m \varphi_m(x) \tag{3.14}$$

where $\varphi_m(x)$ is the assumed admissible function satisfying the boundary conditions of the beam and A_m is the undermined coefficient. The selection of $\varphi_m(x)$ follows the method proposed by Zhou [29], which composes of free vibrating beam eigenfunctions and polynomials.

Now the Rayleigh's method is used to determine the natural frequencies and mode shapes of the beam. The maximum potential and kinetic energies of the beam over a vibration cycle can be expressed as follows:

$$E_{So} = \int_0^L \frac{1}{2} EI \left[\frac{\partial^2 W(x)}{\partial x^2}\right]^2 dx$$

$$E_{Ko} = \int_0^L \frac{1}{2} \bar{m}\omega^2 [W(x)]^2 \, dx \tag{3.15}$$

Substituting Eq. (4.13) into Eq. (4.14) and taking the first derivation of the Rayleigh's quotient with respect to each coefficient A_m would lead to the eigenvalue equations in a matrix form as following:

$$(\boldsymbol{K} - \omega^2 \boldsymbol{M})\boldsymbol{A} = \boldsymbol{0} \tag{3.16}$$

where

$$\boldsymbol{A} = \{A_1, A_2, \ldots . A_m\}^T$$

$$\boldsymbol{K_{ij}} = \int_0^L EI\varphi_i''(x)\varphi_j''(x)dx$$

$$\boldsymbol{M_{ij}} = \int_0^L \bar{m}\varphi_i(x)\varphi_j(x)dx \qquad (i = 1, 2, \cdots, m; j = 1, 2, \cdots, m) \tag{3.17}$$

, m is the number of assumed admissible functions; $\varphi_i'(x)$, $\varphi_i''(x)$ are the first and second derivatives of $\varphi_i(x)$ with respect to x.

The natural frequencies ω and coefficients A_m can be determined from Eq. (3.16). Then the mode shape functions of the beam $W(x)$ can be determined through Eq. (3.14).

3.3.3. Vehicle Model

To better understand the bridge-vehicle interaction, a half-vehicle vibration model shown in Fig. 3.2 is adopted in current study. This vehicle model has four degrees of freedom, corresponding to the vertical displacement of vehicular body (z_c), rotation of vehicular body about the transverse axis (θ_c), the vertical displacements of the front wheel (z_f) and rear wheel (z_r). Applying the Lagrange method, the equations of motion for the half-vehicle model can be derived and expressed in a matrix form as following:

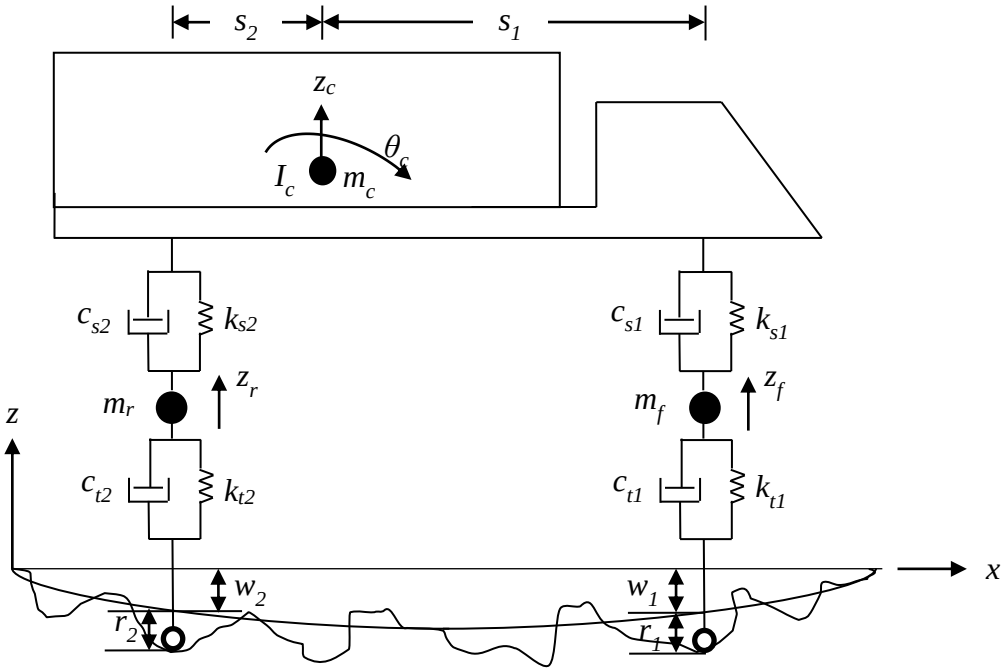

Fig. 3.2. Half-vehicle vibration model

$$\boldsymbol{M_v\ddot{Z} + C_v\dot{Z} + K_vZ = F_v^{int}} \tag{3.18}$$

where

$$\boldsymbol{Z} = \begin{bmatrix} Z_c \\ \theta_c \\ Z_f \\ Z_r \end{bmatrix} \qquad \boldsymbol{M_v} = \begin{bmatrix} m_c & 0 & 0 & 0 \\ 0 & I_c & 0 & 0 \\ 0 & 0 & m_f & 0 \\ 0 & 0 & 0 & m_r \end{bmatrix} \qquad \boldsymbol{F_v^{int}} = \begin{bmatrix} 0 \\ 0 \\ k_{t1}(w_1 + r_1) + c_{t1}(\dot{w}_1 + \dot{r}_1) \\ k_{t2}(w_2 + r_2) + c_{t2}(\dot{w}_2 + \dot{r}_2) \end{bmatrix}$$

$$\boldsymbol{C_v} = \begin{bmatrix} c_{s1} + c_{s2} & s_2 c_{s2} - s_1 c_{s1} & -c_{s1} & -c_{s2} \\ s_2 c_{s2} - s_1 c_{s1} & s_1^2 c_{s1} + s_2^2 c_{s2} & s_1 c_{s1} & -s_2 c_{s2} \\ -c_{s1} & s_1 c_{s1} & c_{s1} + c_{t1} & 0 \\ -c_{s2} & -s_2 c_{s2} & 0 & c_{s2} + c_{t2} \end{bmatrix}$$

$$\boldsymbol{K_v} = \begin{bmatrix} k_{s1} + k_{s2} & s_2 k_{s2} - s_1 k_{s1} & -k_{s1} & -k_{s2} \\ s_2 k_{s2} - s_1 k_{s1} & s_1^2 k_{s1} + s_2^2 k_{s2} & s_1 k_{s1} & -s_2 k_{s2} \\ -k_{s1} & s_1 k_{s1} & k_{s1} + k_{t1} & 0 \\ -k_{s2} & -s_2 k_{s2} & 0 & k_{s2} + k_{t2} \end{bmatrix} \quad (3.19)$$

, $\dot{\boldsymbol{Z}}$, $\ddot{\boldsymbol{Z}}$ are the first and second derivatives of $\boldsymbol{Z}$ with respect to time t; m_c, I_c, m_f, m_r are half of vehicular body mass, half of vehicular body lateral mass moment of inertia, the mass of a front wheel, and the mass of a rear wheel respectively; k_{s1}, k_{s2}, c_{s1}, c_{s2} are the stiffness and damping coefficients of the front and rear suspensions respectively; k_{t1}, k_{t2}, c_{t1}, c_{t2} are the stiffness and damping coefficients of the front and rear tires respectively; s_1, s_2 are the distance of the center of gravity of the vehicular body from the front and rear axles respectively; w_1, w_2 are the deflection of the bridge at the location of the front and rear wheels respectively; and $\dot{w}_1$, $\dot{w}_2$ are the first derivative of w_1, w_2 with respect to time *t*; r_1, r_2 are the surface roughness of the bridge pavement at the location of the front and rear wheels respectively; $\dot{r}_1$, $\dot{r}_2$ are the first derivative of r_1, r_2 with respect to time *t*. Note that the vehicle displacement vector $\boldsymbol{Z}$ is measured from the static equilibrium position of the vehicle, which leads to no gravity term in Eq. (3.18).

3.3.4. Bridge-Vehicle Interaction Force

The bridge-vehicle interaction forces for a single vehicle can be described as follows:

$$\begin{aligned} F_{t1} &= k_{t1}(Z_f - w_1 - r_1) + c_{t1}(\dot{Z}_f - \dot{w}_1 - \dot{r}_1) - \left(m_f + m_c \frac{s_2}{s_1 + s_2}\right) g \\ F_{t2} &= k_{t2}(Z_r - w_2 - r_2) + c_{t2}(\dot{Z}_r - \dot{w}_2 - \dot{r}_2) - (m_r + m_c \frac{s_1}{s_1 + s_2}) g \end{aligned} \quad (3.20)$$

3.3.5. Road Surface Roughness of the Bridge

Road surface roughness can be described by the power spectral density (PSD) of its vertical displacement. The general form of the displacement PSD can be expressed as [31]:

$$G_d(n) = G_d(n_0)(\frac{n}{n_0})^{-w} \quad (3.21)$$

where n is the spatial frequency (cycle/m); n_0 (=0.1 cycle/m) is the reference spatial frequency; w is the exponent of the PSD, which is taken as 2 in the present study.

In the space domain, road surface roughness can be simulated by applying the inverse fast Fourier transformation on $G_d(n)$ as following [10]:

$$r(x) = \sum_{i=1}^{N} \sqrt{4G_d(i \cdot \Delta n)\Delta n}\ \cos(2\pi \cdot i \cdot \Delta n \cdot x + \varphi_i) \quad (3.22)$$

where x is the horizontal ordinate of the road profile from 0 to L; L is the length of the road profile; $\Delta n = 1/L$; $N = L/B$; B is the sampling interval of the road profile; φ_i is a set of randomly generated phase angle following an uniform probabilistic distribution within the 0–2π range.

3.4. Numerical Simulations

3.4.1. Numerical Algorithm

The dynamic responses of the bridge and vehicle can be calculated from Eqs. (3.8), (3.9), (3.18), (3.19), and (3.20) using the Newmark-β method. The implementation procedure of the Newmark integration method is shown in Fig. 3.3, in which v is the speed of the vehicle and ***Error*** representing the difference between the results of two consecutive iterations is defined as following:

$$Error = \sqrt{\left[\frac{w_1(x,t)_j - w_1(x,t)_{j-1}}{w_1(x,t)_j}\right]^2 + \left[\frac{w_2(x,t)_j - w_2(x,t)_{j-1}}{w_2(x,t)_j}\right]^2} \quad (3.23)$$

where $w_1(x,t)_{j-1}$, $w_1(x,t)_j$ are the deflection of the bridge at the front wheel location in the $(j-1)^{\text{th}}$ iteration and $(j)^{\text{th}}$ iteration respectively; $w_2(x,t)_{j-1}$, $w_2(x,t)_j$ are the deflection of the bridge at the rear wheel location in the $(j-1)^{\text{th}}$ iteration and the $(j)^{\text{th}}$ iteration respectively.

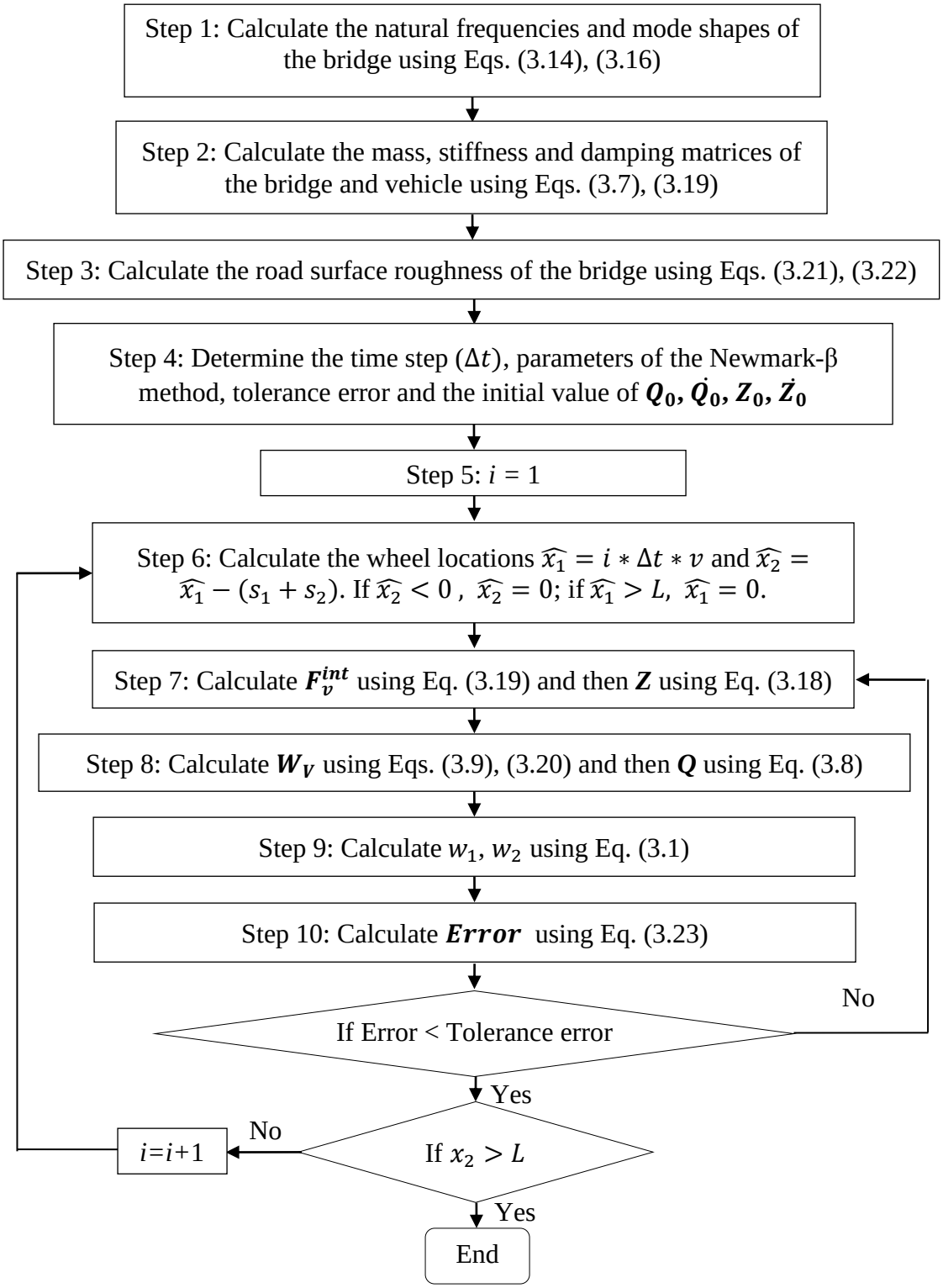

Fig. 3.3. Flow chart of implementation

3.4.2. Verification

Verification of the bridge model developed in Section 3.3.1 and 3.3.2 has been conducted in three steps on a two-span continuous bridge with properties of overall span length L = 18+18 = 36 m, flexural rigidity EI = 3.245×10^9 N·m^2 and mass per unit length $\bar{m}$ = 2052 kg/m, as shown in Fig. 3.4.

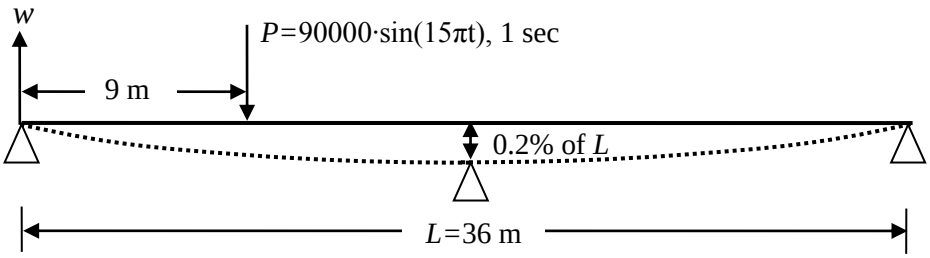

Fig. 3.4. A two-span continuous bridge used for verification

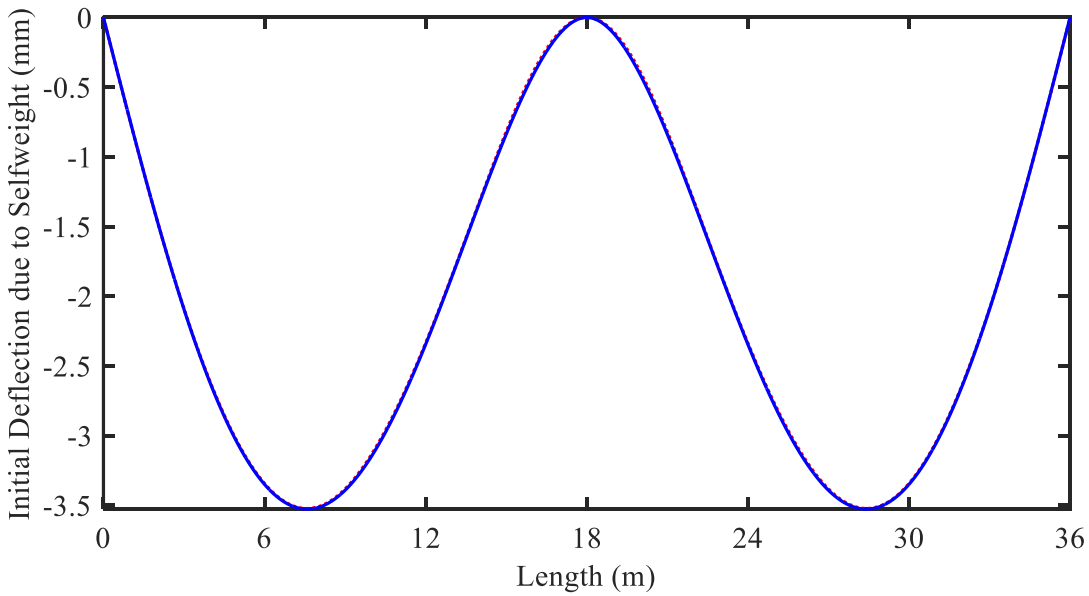

Fig. 3.5. Initial deflection of the two-span continuous bridge due to gravity load
Proposed method; Theoretical result.

First, the initial deflection of the bridge due to the gravity load has been calculated through Eq. (3.11) in a mode-analysis way and then compared with the theoretical result

obtained by solving the classical beam differential equation. These two results are almost the same as shown in Fig. 3.5, indicating the effectiveness and accuracy of the proposed method.

Table 3.1. Natural frequencies of the two-span continuous bridge (Hz)

Mode	Proposed method	Abaqus modeling				
	With/Without settlement	Without settlement (Nlgeom on/off)	With (of L) settlement (Nlgeom **off**)		With (of L) settlement (Nlgeom **on**)	
			0.1%	0.2%	0.1%	0.2%
1	6.096	6.097	6.097	6.097	6.101	6.115
2	9.533	9.524	9.524	9.524	9.528	9.541
3	24.386	24.386	24.386	24.386	24.391	24.405
4	30.960	30.864	30.864	30.864	30.868	30.882
5	54.868	54.869	54.869	54.869	54.873	54.887
6	64.820	64.394	64.394	64.394	64.399	64.413
7	97.544	97.544	97.544	97.544	97.549	97.562
8	111.413	110.118	110.118	110.118	110.123	110.136
9	152.412	152.413	152.413	152.413	152.417	152.430
10	171.451	168.035	168.035	168.035	168.039	168.053

Second, natural frequencies of the continuous bridge with or without central support settlement were determined from both current study by using Eq. (3.16) and finite element analysis with Abaqus software. A 2-node cubic beam element (B33) was chosen to use and settlement was applied as change of boundary condition in Abaqus modeling. The comparison between two results is shown in Table 3.1. Current study assumes that the bridge is still in linear elastic range or without crack under small settlement ($\leq$ 0.4% of span length $1/2L$ or 0.2% of total length L), and concludes that natural frequencies of the bridge are not affected by that small settlement, which agrees with the experimental results of Wahab and Roeck [30] on a settled bridge. Abaqus modeling achieves the same conclusion for the case without considering the geometric nonlinearity induced by settlement (Nlgeom **off**). The option 'Nlgeom' in Abaqus

controls the inclusion or exclusion of nonlinear effects of ‘large displacements and deformation’. With ‘Nlgeom’ on, the result has little change, which is negligible.

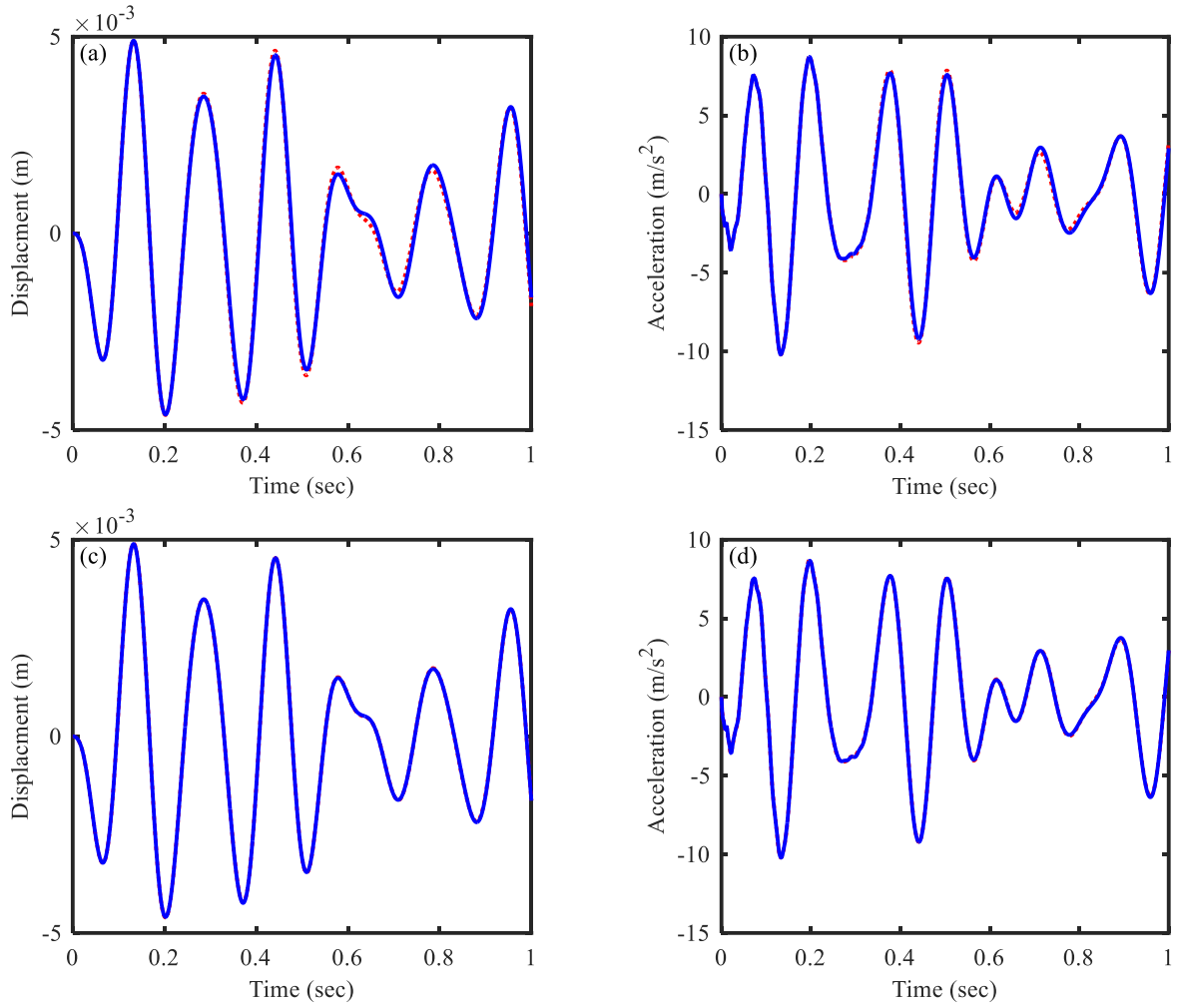

Fig. 3.6. Comparison of the bridge response at loading position
(a) Displacement; (b) Acceleration: ····· Nlgeom **on**; ——— Nlgeom **off**.
(c) Displacement; (d) Acceleration: ····· Nlgeom **off**; ——— Current study.

Third, a sinusoidal load with the amplitude of 90 kN and a circular frequency of 15π rad/s was applied at the middle of the first span of the bridge as shown in Fig. 3.4. The duration of the load is 1.0 sec and the bridge has a center support settlement of 0.2% of L. A time step of 0.001 sec and a damping coefficient of 0.02 have been chosen for both current study and Abaqus modeling. Time histories of displacement and acceleration of the bridge at loading position from

Abaqus are shown in Fig. 3.6 (a) and (b) respectively. It can be seen that there is little difference between the case 'Nlgeom on' and the case 'Nlgeom off'. The results from current study are the same as that from Abaqus with 'Nlgeom' off, as shown in Fig. 3.6 (c) and (d). Thus, a general conclusion can be obtained that proposed method is accurate enough to capture the bridge dynamic response ignoring the geometric nonlinearity induced by small support settlement.

3.4.3. Parametric Study

Numerical simulations following the algorithm shown in Section 3.4.1 were conducted to investigate the dynamic effect of foundation settlement on the bridge and vehicle responses, considering different settlement modes, vehicle speeds, bridge span lengths, road surface roughness conditions and bridge types. The same bridge properties as that in verification part were used through the study. The vehicle parameters used by Maechesiello [8] are adopted in the present study with some of them modified to accommodate the half vehicle model and listed as following: m_c = 8500 kg, I_c = 4.5×10^4 kg·m^2, m_f = 300 kg, m_r= 500 kg, k_{s1} = 1.16×10^5 N/m, k_{s2} = 3.73×10^5 N/m, k_{t1} = 7.85×10^5 N/m, k_{t2} = 1.57×10^6 N/m, c_{s1} = 2.5×10^4 N·sec/m, c_{s2} = 3.5×10^4 N·sec/m, c_{t1} = 100 N·sec/m, c_{t2} = 200 N·sec/m.

In this study, a program was coded in Matlab to compute the bridge and vehicle dynamic responses using the Newmark-β method withγ = 0.5 and β = 0.25, which implies a constant average acceleration over a time step with unconditional stability. The first 10 modes of the bridge were used in the calculation with a damping coefficient of 0.02 for all the modes. A time step of 0.0001 sec was selected and the tolerance error between two consecutive iterations was set to be 0.01.

3.4.3.1. Effect of settlement modes

Since the studied bridge is symmetric and vehicles can enter the bridge from both directions, two settlement modes were investigated with left and central support settled respectively, as shown in Fig. 3.7. Both modes have a settlement of 0.2% of the overall length L (the maximum settlement suggested by AASHTO [4]), and the vehicle travelling on them has a speed of 30 m/s.

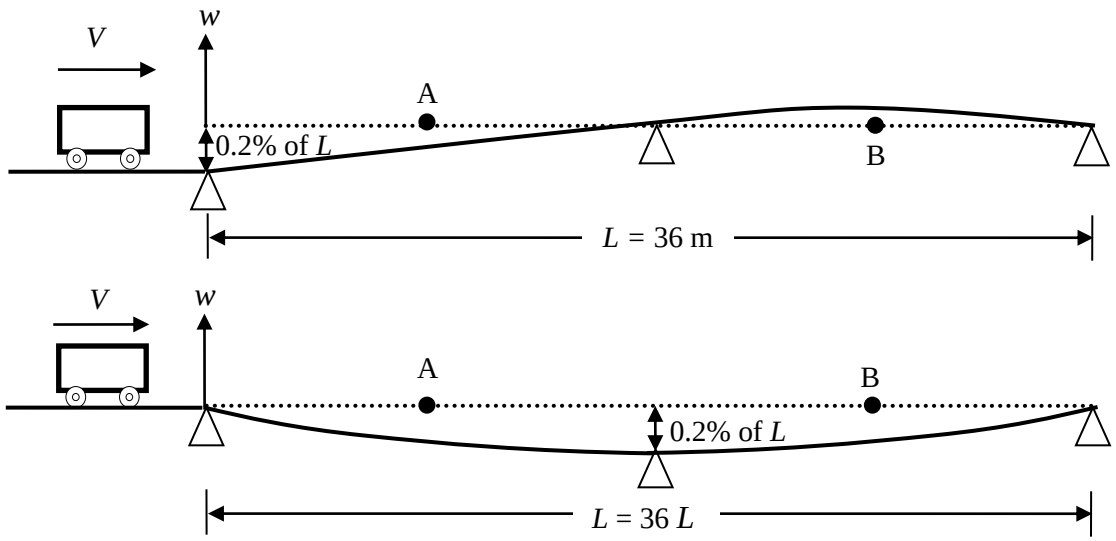

Fig. 3.7. Bridge settles at: Left support (top); (b) Central support (bottom).

Time histories of the displacement at the middle of the first span (Point A) and the second span (Point B) of the bridge under different settlement modes are plotted in Figs. 3.8(a) and 3.8(b), while the front tire force and vertical acceleration of the vehicle are shown in Figs. 3.8(c) and 3.8(d). As can be seen, the change of vehicle responses due to settlement is much larger than that for bridge, for which the reason is that the bridge is much heavier and stiffer than the vehicle and thus less susceptible to the settlement. The maximum and minimum of vehicle responses are summarized in Table 3.2, in which RMS represents root mean square of the vertical vehicle acceleration and can be calculated by Eq. (3.24). The magnitude of RMS is closely related to the

ride comfort of the vehicle, and the significant change of RMS due to settlement as shown in Table 3.2 may cause considerable discomfort to passengers.

$$RMS = \left\{\frac{1}{T}\int_0^T [a(t)]^2 dt\right\}^{1/2} \tag{3.24}$$

where $a(t)$ is the vehicle acceleration at time t and T equals the time duration.

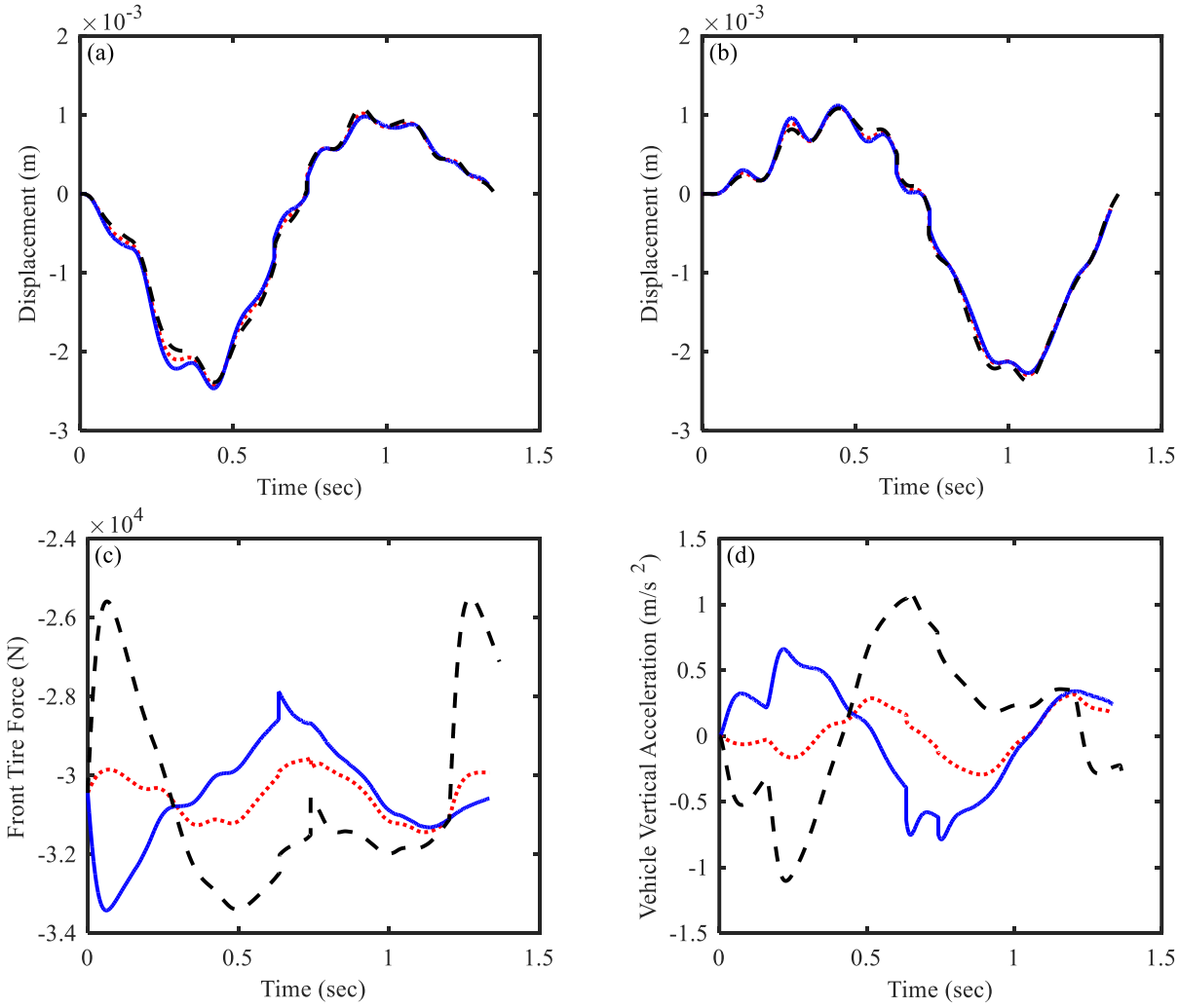

Fig. 3.8. Comparison of bridge and vehicle responses for different settlement modes
(a) Displacement of the bridge at Point A; (b) Displacement of the bridge at Point B;
(c) Front tire force of the vehicle; (d) Vertical vehicle acceleration.
No settlement; Left support settlement; Center support settlement.

Table 3.2. Summary of the vehicle responses

Settlement mode	Vehicle acceleration (m/s^2)			Vehicle tire force (×10^4 N)			
	Min	Max	RMS	Front		Rear	
				Min	Max	Min	Max
No	-0.294	0.316	0.179	-2.956	-3.144	-5.841	-6.307
Left	-0.787	0.660	0.409	-2.789	-3.343	-5.494	-6.551
Center	-1.103	1.102	0.573	-2.549	-3.340	-5.243	-6.929

Fig. 3.9 shows the distribution of impact factors along the bridge for three cases. The impact factor is defined as following:

$$I_p = \left(\frac{D_d}{D_s} - 1\right) \times 100\% \tag{3.25}$$

where D_d and D_s are the maximum dynamic and static displacement of the bridge due to the vehicle loading respectively. Here D_s can be readily obtained by assuming $\dot{\boldsymbol{Q}}_{\boldsymbol{0}} = \ddot{\boldsymbol{Q}}_{\boldsymbol{0}} = [\boldsymbol{0}]_{\boldsymbol{N\times 1}}$ and then solving Eq. (3.8). It needs to note that this approach is much easier and more straightforward than the existing method assuming a very slow vehicle speed and then solving the dynamic bridge-vehicle interaction response. From Fig. 3.9, one can observe that compared with the distribution for no-settlement case, left support settlement results in larger impact factors at the left span and smaller ones at the right span, and in contrast, center support settlement leads to smaller impact factors at the left span and larger ones at the right span. This can be explained by using Fig. 3.8(c), in which the increasing or decreasing tire force due to settlement harvests corresponding larger or smaller impact factors at each span. It can be easily understood that when climbing upon a slope like in Fig. 3.7(a), the vehicle tire is compressed at the beginning to generate a larger tire force making bigger impact factors, and then rebound to have a smaller force at the time of the slope becoming flatter and flatter. In the similar way, when driving across a valley like in Fig. 3.7(b), the tire will first be released and then

compressed to produce the force shown in Fig. 3.8(c), which leads to the distribution in Fig. 3.9. The above observations consist with the common sense of life well.

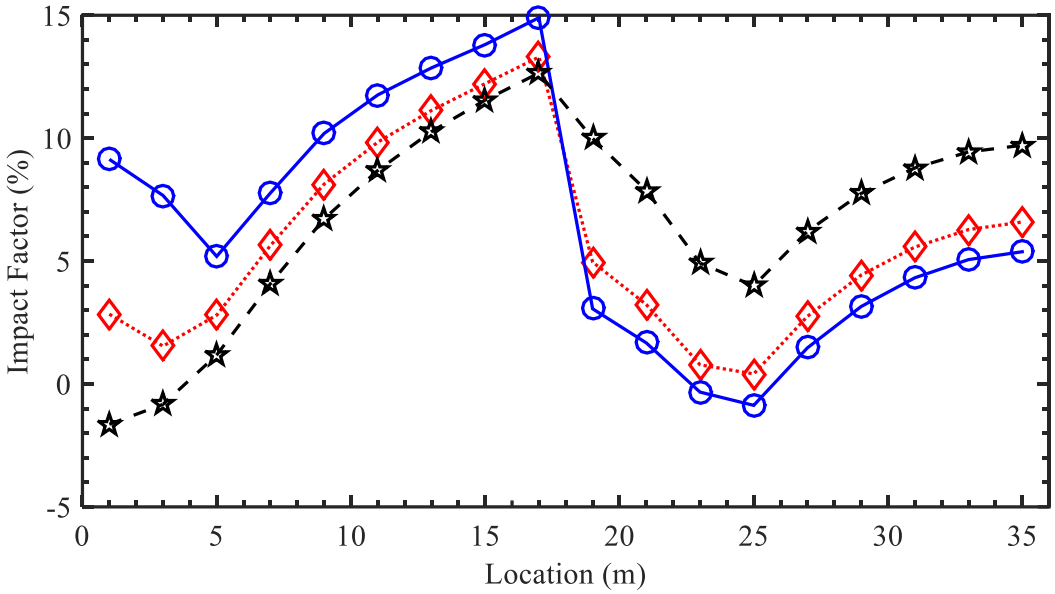

Fig. 3.9. Impact factors for the bridge displacement

No settlement; Left support settlement; Center support settlement.

Time step is of great importance in dynamic simulation and needs special attention. Fig. 3.10 shows the results of convergence analysis conducted on dynamic bridge and vehicle responses for three different time steps – 0.001 sec, 0.0001sec and 0.00001 sec. As can be seen, the smallest time step gives the most satisfactory or smoothest results, however, the computation time required for completing a simulation with this small time step is nearly 22 hours on an average computer, much longer than that for the other two time steps, which is 0.5 hour for 0.001 sec and 3 hours for 0.0001 sec. Considering both computational efficiency and accuracy, a time step of 0.0001 sec is finally selected to be used all through the study.

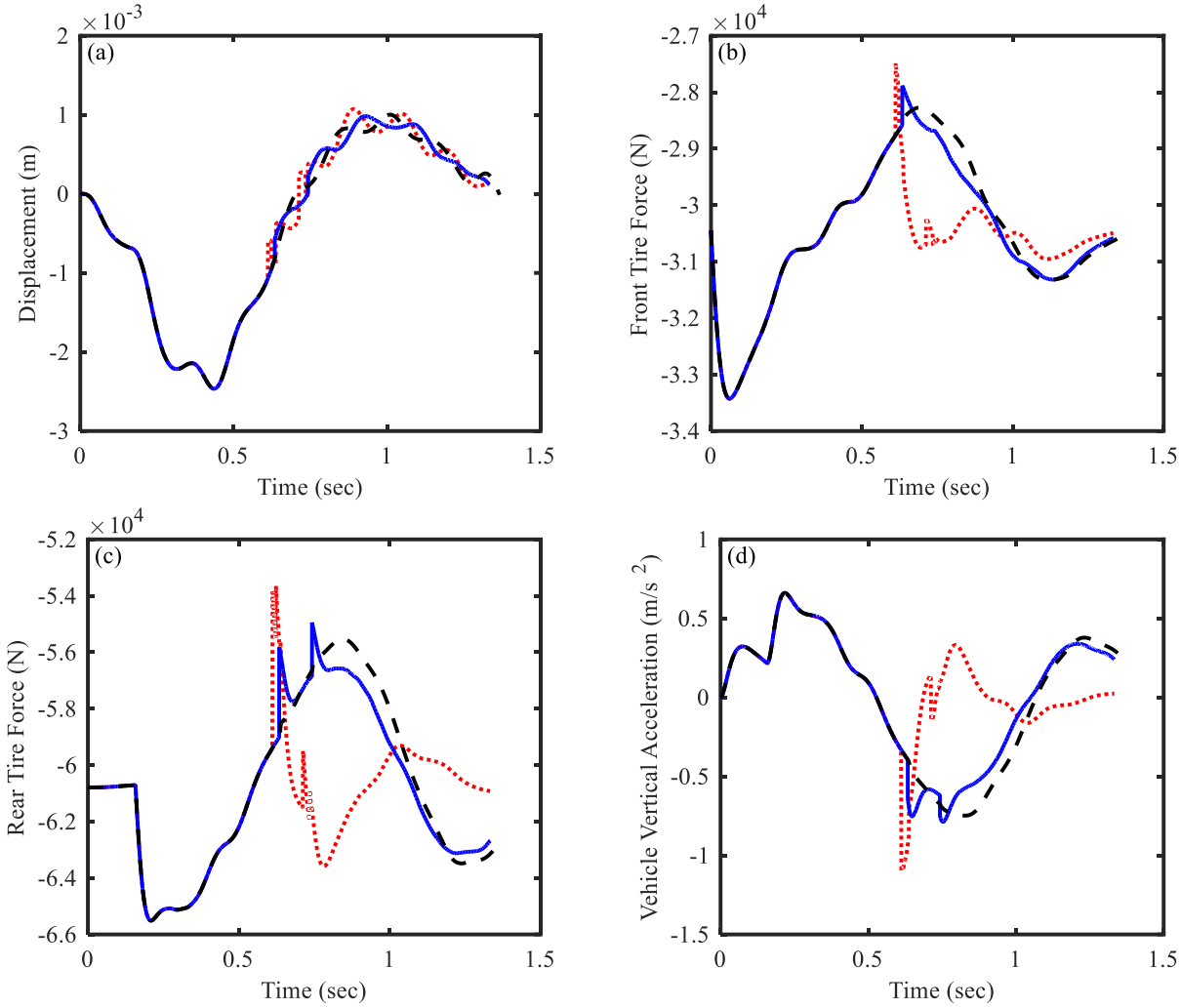

Fig. 3.10. Convergence analysis of the time step (Left support settlement)
(a) Displacement of the bridge at Point A; (b) Front vehicle tire force;
(c) Rear vehicle tire force; (d) Vertical vehicle acceleration.
····· Δt = 0.001 sec, 0.5 hr; ——— Δt = 0.0001 sec, 3 hrs; – – – – Δt = 0.00001 sec, 22 hrs.

3.4.3.2. Effect of vehicle speed

Vehicle speed plays an important role in bridge vehicle interaction. Figs. 3.11(a) and 3.11(b) shows the change of impact factors at Point A and B with the speed increasing from 20 m/s to 40 m/s. It can be observed that the difference between no-settlement case and with-settlement cases becomes increasingly larger with the speed increase, and the settlement has significant impact on bridge vehicle interaction at high speeds.

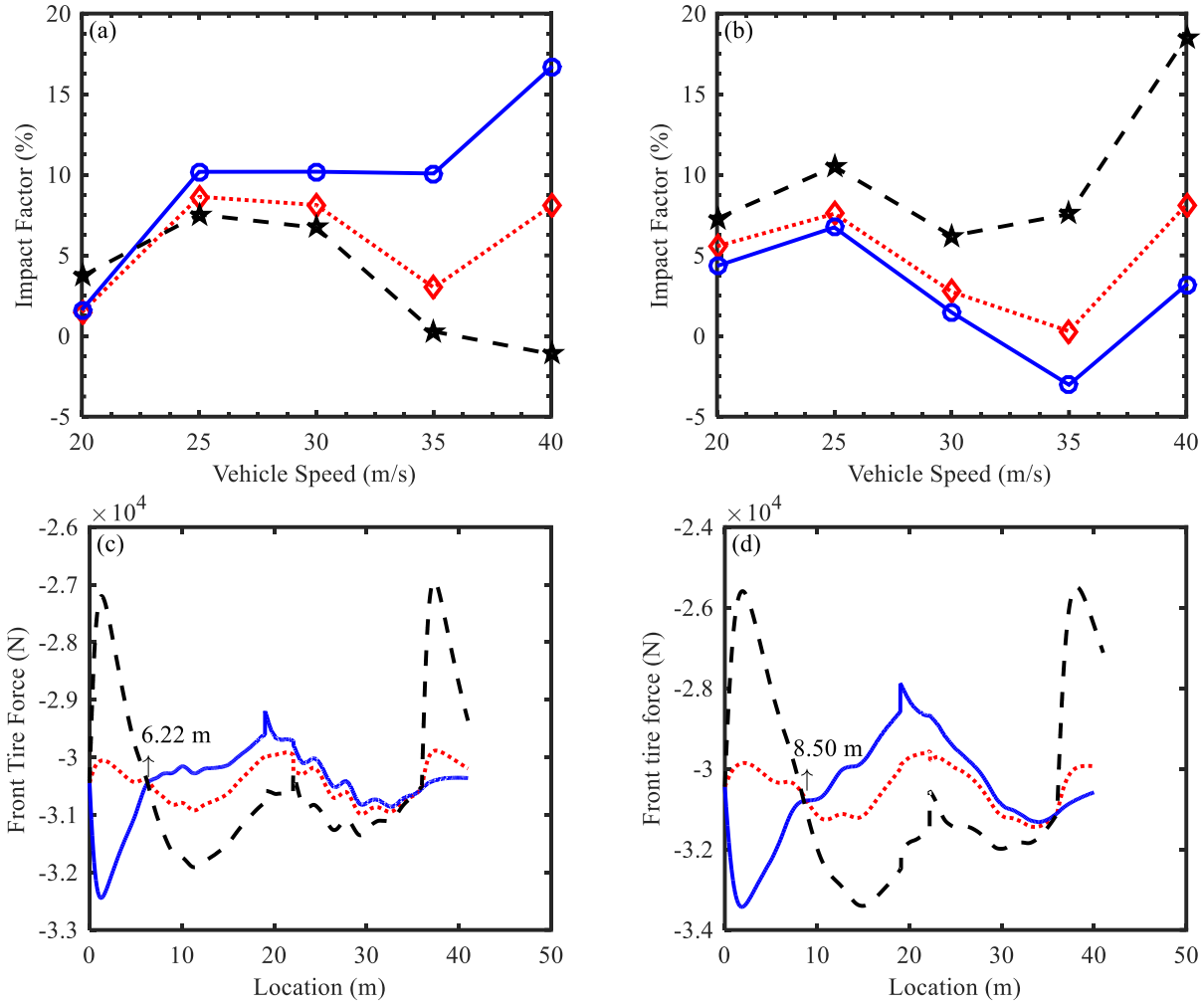

Fig. 3.11. Comparison of bridge and vehicle responses for different vehicle speeds (a) Impact factor at Point A of the bridge; (b) Impact factor at Point B of the bridge: ····◇···· No settlement; —○— Left support settlement; – – ★ – – Center support settlement. Front tire force of the vehicle: (c) V = 20 m/s; (d) V = 30 m/s. ····· No settlement; ——— Left support settlement; – – – – Center support settlement.

It is interesting to notice that in Fig. 3.11(a), at the speed of 20 m/s, the impact factor for center support settlement case is surprisingly larger than that for no-settlement case, which is opposite to the general trend at the other speeds. The reason for that may be seen from Figs. 3.11(c) and 3.11(d) depicting the change of front tire force of the vehicle along the path at the speed of 20 m/s and 30 m/s respectively. At 20 m/s, as shown in Fig. 3.11(c), the front tire force for center support settlement is smaller than that for no-settlement case at the first 6.22 m but

quickly becomes larger in the following location. In other words, the vehicle still have enough time or distance to pass sufficient energy to the bridge to make it obtain a larger displacement at Point A (9.00 m) and thus induces a bigger impact factor compared with the no-settlement case. However, the things change at the speed of 30 m/s. As Fig. 3.11(d) shows, the tire force decreases more due to center support settlement than that at 20 m/s and becomes larger until 8.50 m, which leaves no time for the vehicle to actuate a large displacement at Point A (9.00 m), resulting in a smaller impact factor shown in Fig. 3.11(a). From the above observation and discussion, it can be seen that the effect of settlement is closely related to or greatly affected by the vehicle speed.

3.4.3.3. Effect of road surface roughness

In this section, four types of road surface profile are investigated in order to examine the effect of surface roughness: S (smooth, no roughness), Class A, Class B and Class C. $G_d(n_0)$ in Eq. (3.21) is a constant controlling the degree of roughness of the road surface, having geometric means of 16×10^{-6} m^3, 64×10^{-6} m^3 and 256×10^{-6} m^3 for Class A, B and C respectively, based on ISO 8608 specifications [31]. Because of the square root shown in Eq. (3.22), if keeping the other parameters the same except $G_d(n_0)$, a certain relationship exists among the three classes of road profile: $r(x, C)$=2× $r(x, B)$= 4× $r(x, A)$, which means that the amplitude of Class C profile at the same position of x is 2 times larger than Class B and 4 times larger than Class A. Namely, they share the same trend but different amplitudes, as shown in Fig. 3.12. The purpose of doing this is to make the simulation results for different classes of road profile more comparable and better serve the research. Moreover, a constraint of nearly zero value at both ends of the bridge has been provided when generating the random surface roughness to ensure a smooth entrance and exit to the bridge for the vehicle, avoiding jump in and jump out.

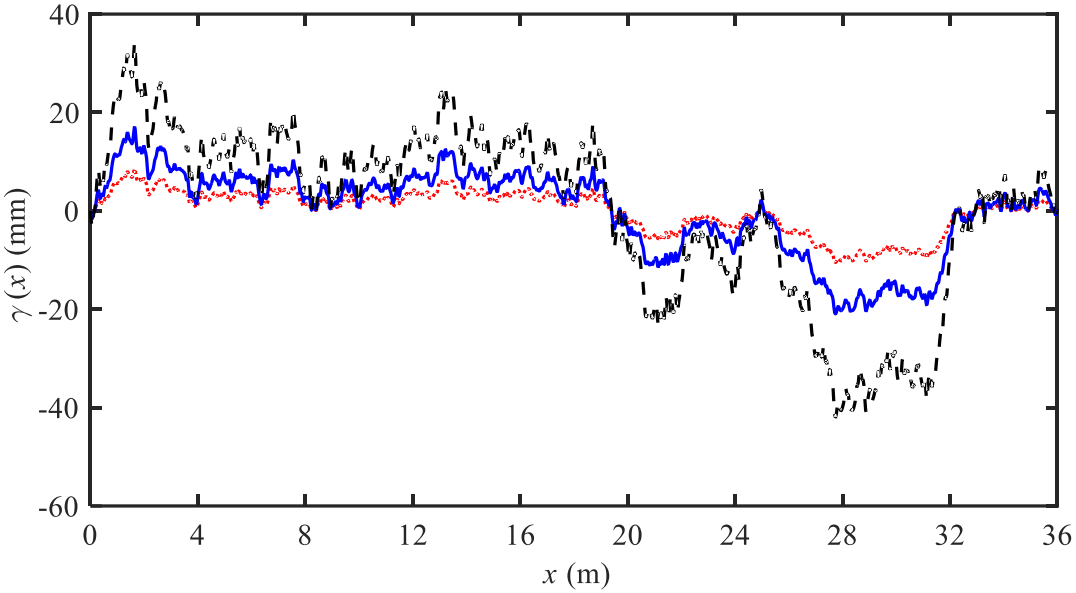

Fig. 3.12. Road surface roughness profiles
Class A; Class B; Class C.

Impact factors at Point A and B of the bridge for different settlement modes, road surface profiles and vehicle speeds are plotted in Figs. 3.13(a)-(d). The following observations can be made from Fig. 3.13:

- Three lines representing three settlement modes in four subfigures are approximately parallel to each other except in Fig. 3.13(d) for Class C profile at 40 m/s;
- At 30 m/s, as shown in Figs. 3.13(a) and 3.13(b), the road surface roughness has a significant effect on impact, indicated by the slope of lines; however, the effect of settlement is small to moderate, represented by the distance between lines;
- At 40 m/s, as Fig. 3.13(c) and 3.13(d) shows, the effect of settlement becomes significant, and the road surface roughness has a moderate to significant effect on impact.

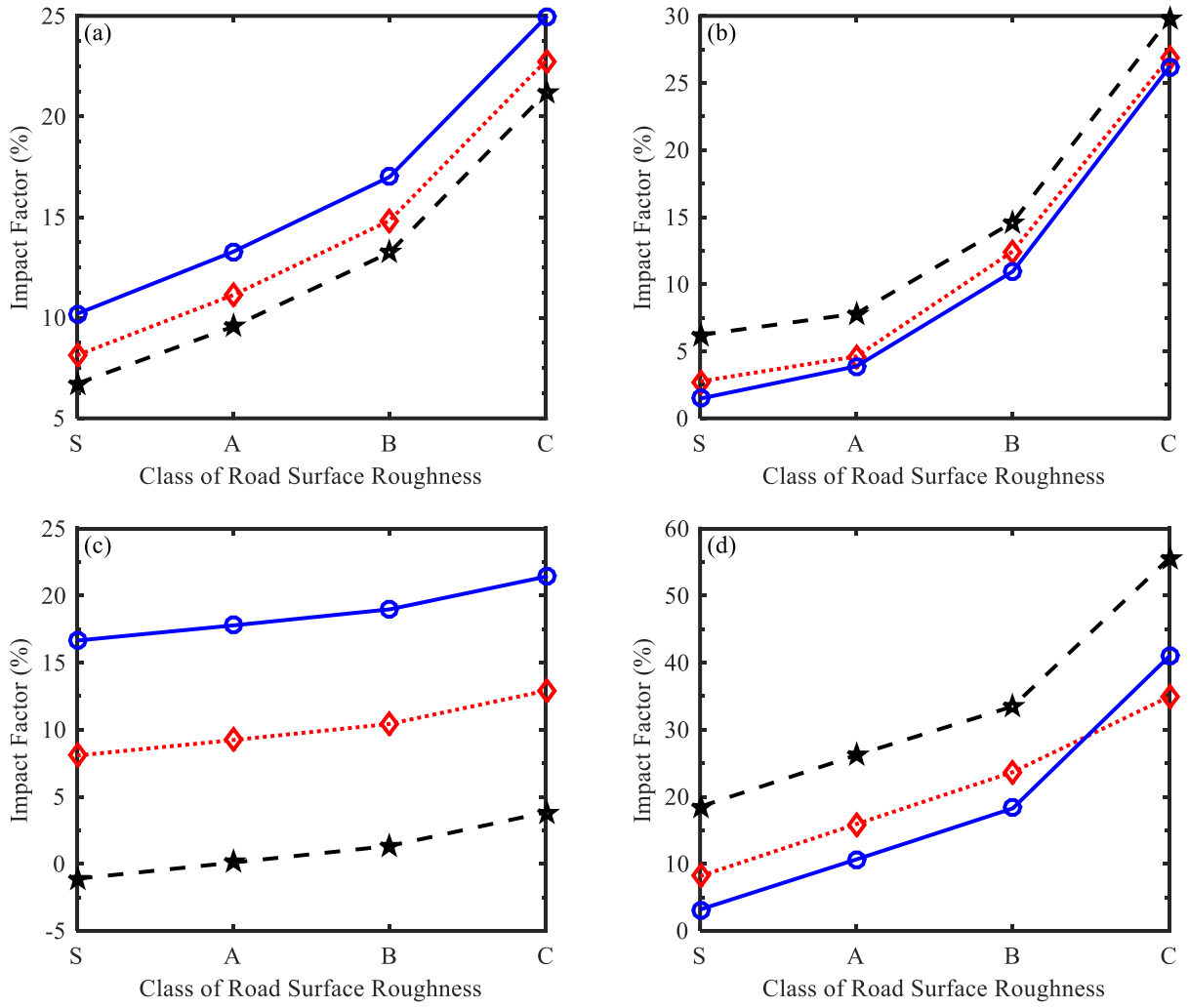

Fig. 3.13. Comparison of impact factors
(a) V = 30 m/s, at Point A; (b) V = 30 m/s, at Point B;
(c) V = 40 m/s, at Point A; (d) V = 40 m/s, at Point B:
No settlement; Left support settlement; Center support settlement.

When the vehicle is traveling on the bridge, it goes point by point in the simulation as shown in Fig. 3.2, like a man walking on the bridge step by step. Since the interval between points ($v \cdot \Delta t$) where v is vehicle speed and Δt is the time step is small enough, the vehicle can be treated as passing the bridge continuously. All those contacted points compose the vehicle traveling profile. Fig. 3.14 shows the spectral analysis of the left settlement profile and Class C road surface profile that are composed by points the vehicle has passed in Fig. 3.7(a) and Fig.

3.12, respectively. It can be seen that both profiles mainly consist of low-frequency components and with the speed increasing from 30 m/s to 40 m/s, a small shift exists and high-frequency components become more obvious. It is worthy to note that the frequency with the peak amplitude in both subfigures changes from 0.83 Hz for 30 m/s to 1.11 Hz for 40 m/s. The two frequencies are actually equal to (v/L) where v is the vehicle speed and L is the bridge length.

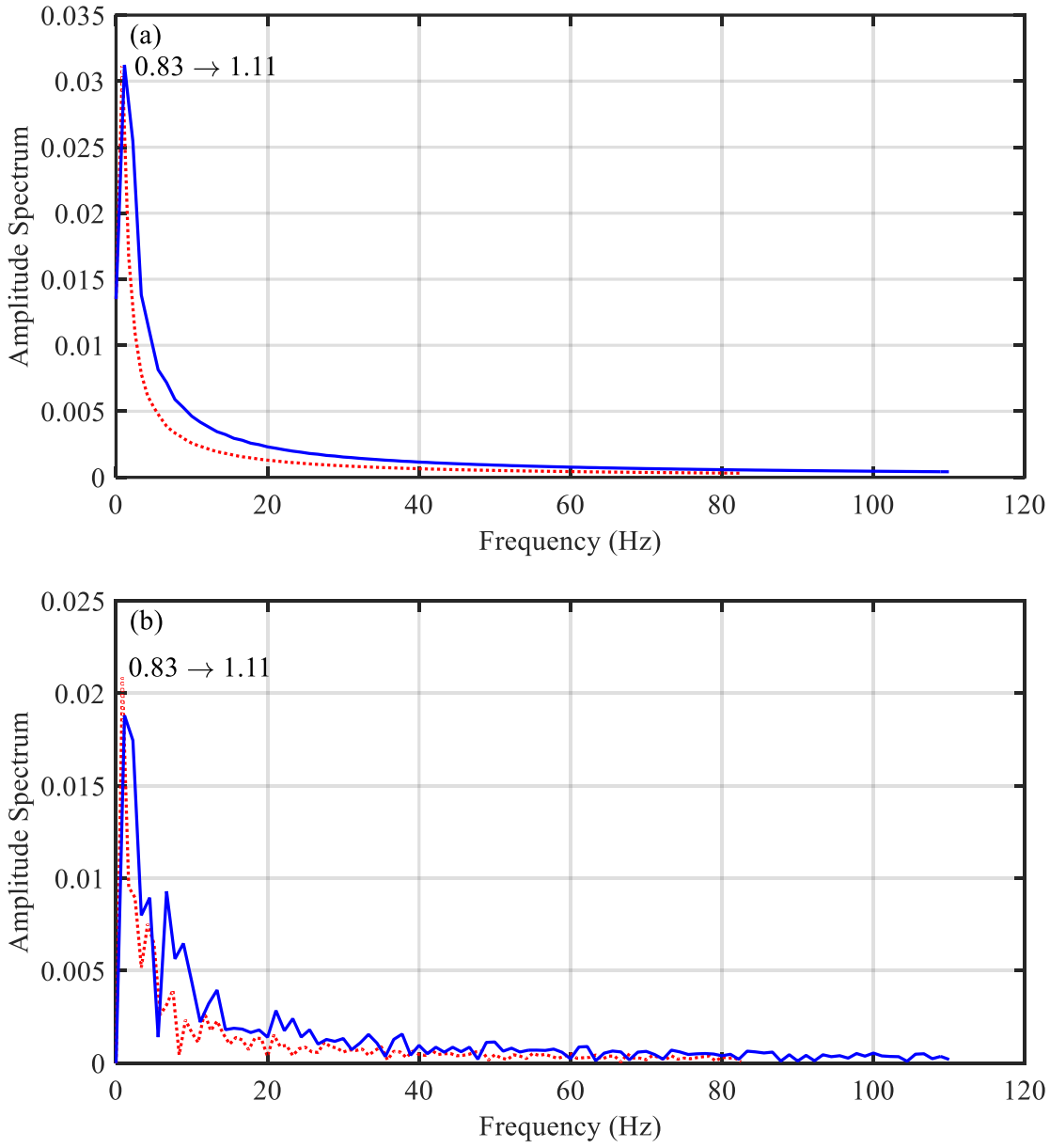

Fig. 3.14. Spectral analysis of left settlement profile (a) and Class C road surface profile (b) ····· 30 m/s; ——— 40 m/s.

Fig. 3.15 shows the spectral analysis of dynamic displacements at Point A and B for No-Roughness case. As can be seen, three lines representing three settlement modes in Fig. 3.15(a) and 3.15(b) are very close to each other, however, they become more distinguishable in Fig. 3.15(c) and 3.15(d), indicating a more significant impact of the settlement on the bridge at 40 m/s than it has at 30 m/s, as shown in Fig. 3.13.

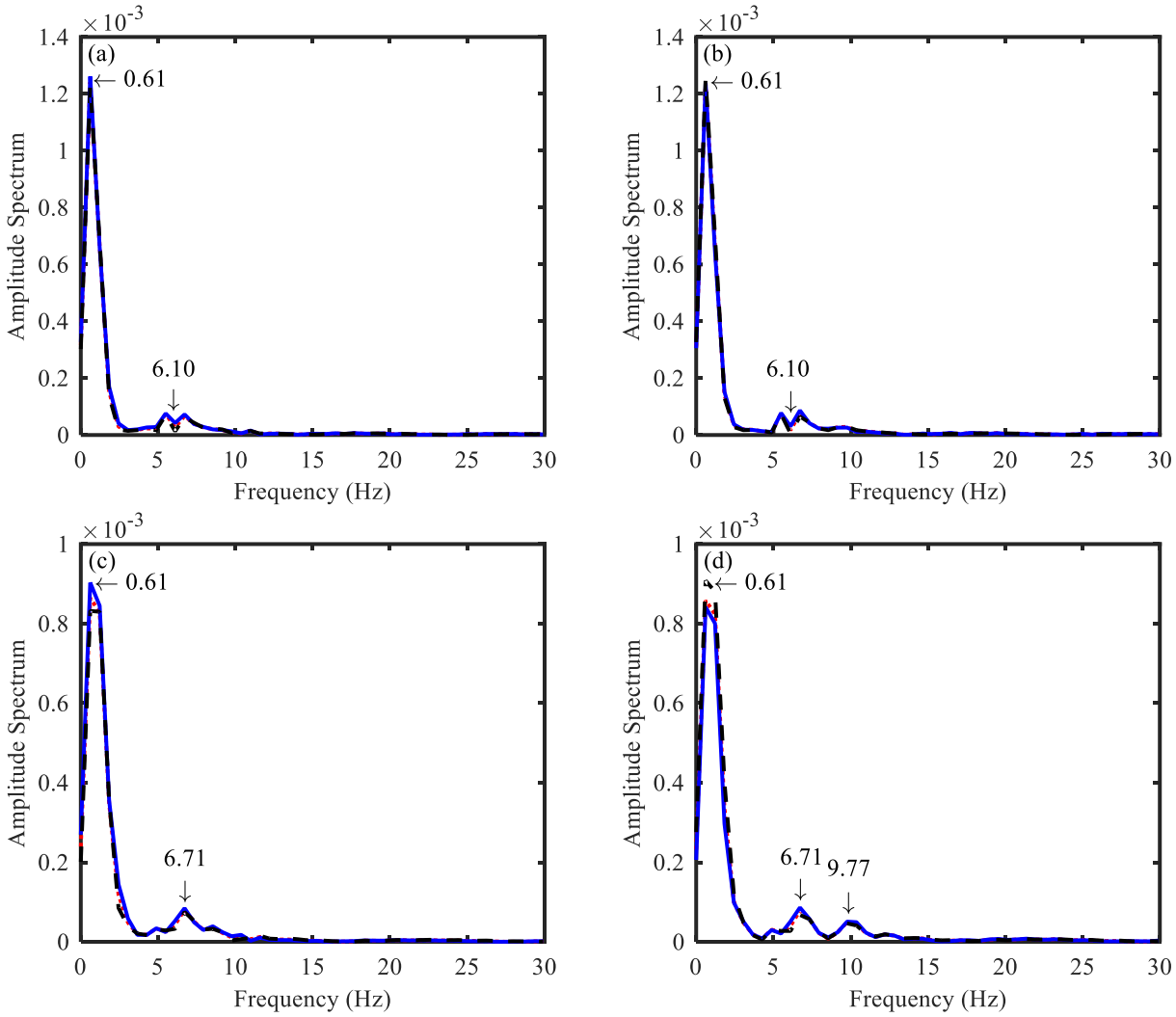

Fig. 3.15. Spectral analysis of the dynamic displacement for No-Roughness cases
(a) Point A, 30 m/s; (b) Point B, 30 m/s; (c) Point A, 40 m/s; (d) Point B, 40 m/s.
No settlement; Left support settlement; Center support settlement.

Without settlement, the effect of road surface roughness on amplitude spectrum of bridge displacements is shown in Fig. 3.16. It can be seen the clear differences among the four lines around 6.10 Hz or 6.71 Hz in Figs. 3.16(a) and 3.16(b), which corresponds to the change of slope of the lines in Fig. 3.13(a) and 3.13(b). At 40 m/s, as shown in Figs. 3.16(c) and 3.16(d), another peak frequency of 10.38 Hz becomes obvious, which may imply that a higher mode of the bridge is getting excited and taking part in the vibration.

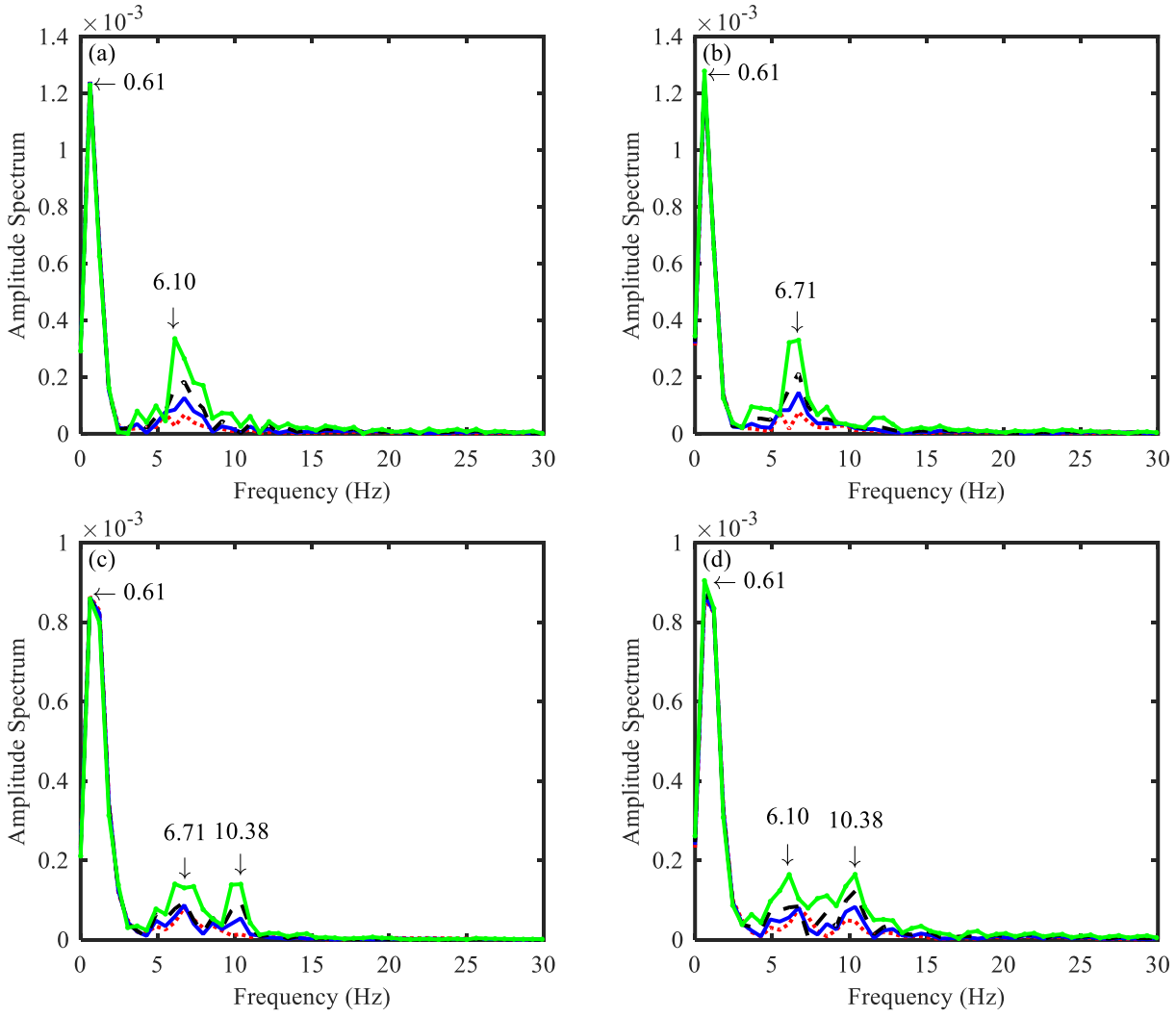

Fig. 3.16. Spectral analysis of the dynamic displacement for No-Settlement case
(a) Point A, 30 m/s; (b) Point B, 30 m/s; (c) Point A, 40 m/s; (d) Point B, 40 m/s
Smooth; Class A; Class B; Class C.

As can be observed from Fig. 3.15 and Fig. 3.16, the bridge mainly vibrates at or around the frequencies of 0.61, 6.71 and 9.77 Hz, which are close to the peak frequency of 0.833 Hz in Fig. 3.14, the first and second natural frequencies of the bridge, 6.10 Hz and 9.53 Hz, respectively. In Fig. 3.15, the frequency of 0.61 Hz is in dominant, with the significantly larger amplitude over other frequencies. Therefore, if a bridge has both settlement and road surface roughness, these two profiles may work together on the vibration of the bridge at 0.61 Hz mostly, which is far from the first natural frequency of 6.10 Hz, leading to no coupling between them. In other words, these two profiles work together but in an independent or superposition way, which results in the parallelism of lines in Fig. 3.13. This has been confirmed in Figs. 3.17(a) and 3.17(b), which shows with or without road surface roughness, the change of tire force due to the settlement is actually the same. Fig. 3.17(a) shows the front tire force at 30 m/s under four different cases, in which 'No-S' indicates the bridge has no settlement with a smooth road surface profile, and 'Left-A' represents 'Left support settlement and Class A road surface roughness profile'. The subtraction results of the tire force for these four cases are shown in Fig. 3.17(b). However, things get changed at 40m/s, point B and Class C road surface profile, as shown in Fig. 3.13(d), parallelism of lines disappearing. The reason for that may be due to the coupling effect of settlement profile and road surface roughness profile, indicated by the fluctuation of the blue solid line after 18 m in Fig. 3.17(d). The appearance of 9.77 Hz in Fig. 3.15(d) and large amplitude of 10.38 Hz in Fig. 3.16(d) could lead to the existence of the coupling.

It needs to point out here that this section is only a preliminary study of the combination of settlement and road surface roughness, and more cases need to be investigated to find out at what condition the coupling exists and the mechanism behind it.

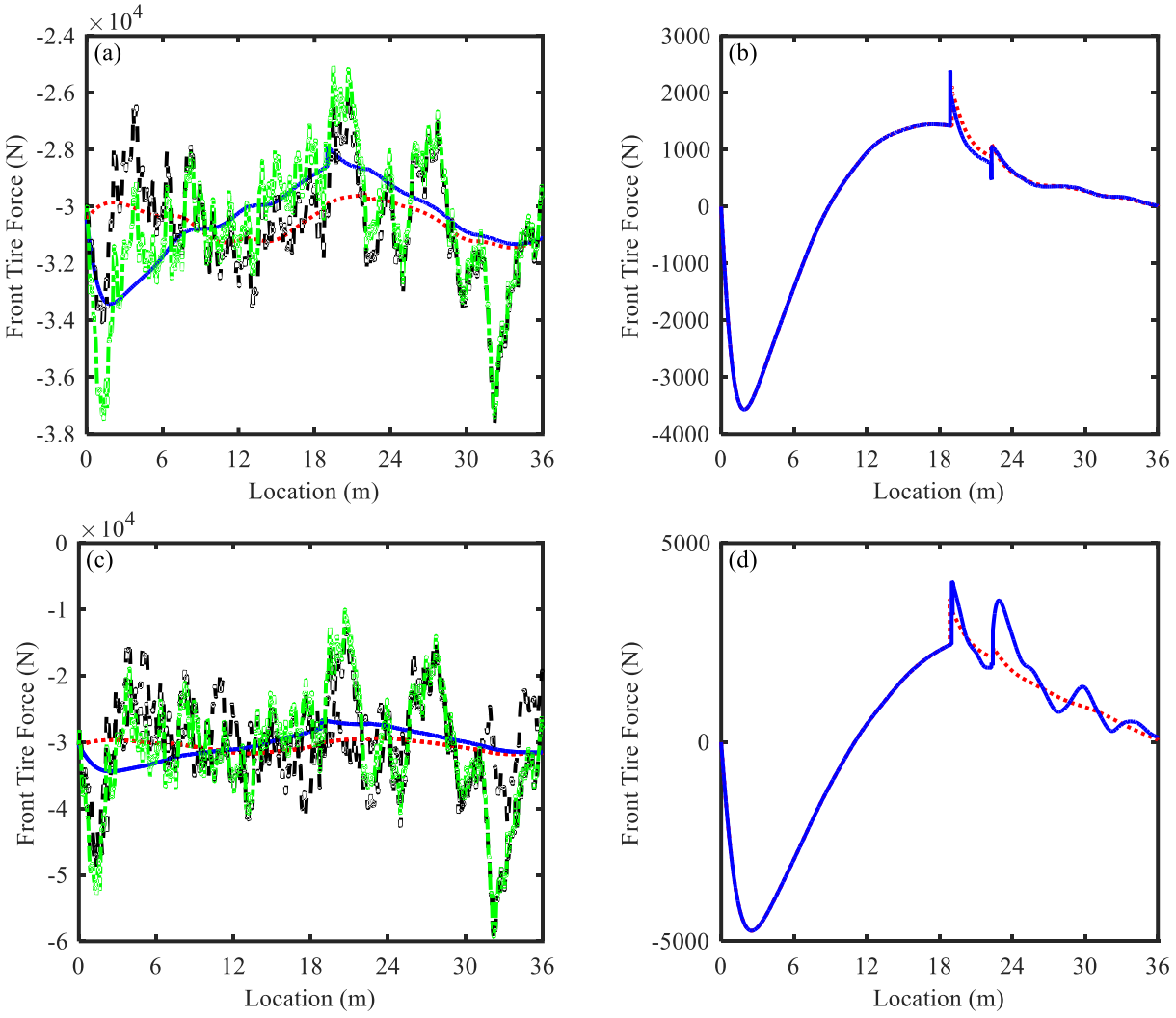

Fig. 3.17. Comparison of front tire forces

(a) 30 m/s: ····· No-S; ——— Left-S; – – – – No-A; – · – · – Left-A.

(b) 30 m/s: ····· $T_{(Left\text{-}S)}$ - $T_{(No\text{-}S)}$; ——— $T_{(Left\text{-}A)}$ - $T_{(No\text{-}A)}$.

(c) 40 m/s: ····· No-S; ——— Left-S; – – – – No-C; – · – · – Left-C.

(d) 40 m/s: ····· $T_{(Left\text{-}S)}$ - $T_{(No\text{-}S)}$; ——— $T_{(Left\text{-}C)}$ - $T_{(No\text{-}C)}$.

3.4.3.4. Effect on two-span simply-supported bridge

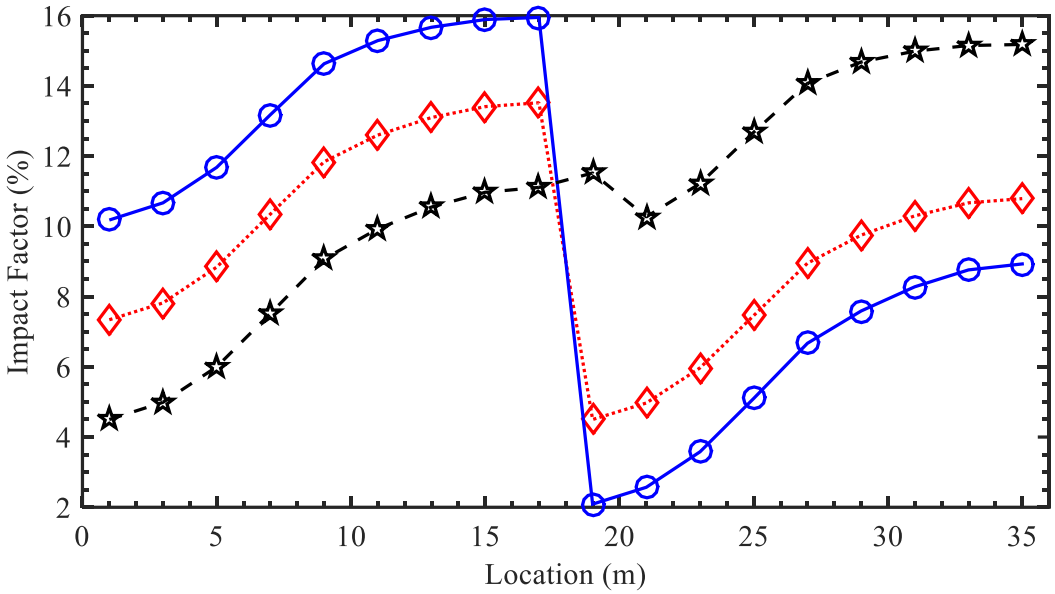

Fig. 3.18. Impact factors for the simply-supported bridge

No settlement; Left support settlement; Center support settlement.

Fig. 3.18 shows the distribution of impact factors along a two-span simply-supported bridge that has the same properties as the continuous bridge studied. Compared with Fig. 3.9, it can be seen that the simply-supported bridge generally has larger impact factors than the continuous one, and the change of impact factors due to support settlements is also bigger. The reason for that may be due to the no constraints of one span from the other, which grants the bridge a lower stiffness and thus more susceptible to the vehicle load and settlement.

3.5. Summary

In this chapter, a new bridge-vehicle interaction model has been created through the principle of virtual works to investigate the effect of bridge foundation settlement. The correctness and accuracy of the proposed model are validated with the theoretical results and numerical results from Abaqus modeling. Based on the created model, numerical simulations

have been conducted to investigate the effects of settlement modes, vehicle speed, road surface roughness, and boundary conditions. The following conclusions were reached.

- Foundation settlement may have adverse or beneficial effects on impact factors of different span of the bridge, depending on the settlement mode.
- Vehicle responses are more vulnerable to the settlement that may result in a poor riding quality.
- The effect of foundation settlement on impact factors increases with the vehicle speed and becomes significant at the high speeds.
- Road surface roughness has considerable effect on the impact factors and may couple with the settlement to aggregate the overall effect.
- Impact factors of simply-supported bridges are more susceptible to the foundation settlement.

3.6. References

[1] Grover, R. A. (1978). Movements of bridge abutments and settlements of approach pavements in Ohio. Transportation Research Record No. 678, Transportation Research Board, Washington, D.C., 12-17.

[2] Walkinshaw, J. L. (1978). Survey of bridge movements in the western United States. Transportation Research Record No. 678, Transportation Research Board, Washington, D.C., 6-10.

[3] Moulton, L. K., GangaRao, H. V., & Halvorsen, G. T. (1985). Tolerable movement criteria for highway bridges. Federal Highway Administration (Report No. FHWA/RD-85-107), Washington.

[4] AASHTO LRFD Bridge Design Specifications, 5th ed. (2010). American Association of State Highway and Transportation Officials, Washington, D.C.

[5] Schopen, D. (2010). Analyzing and designing for substructure movement in highway bridges: an LRFD approach. Master's thesis, University of Delaware.

[6] Wang, Z., Chen, G., Kwon, O. S., & Orton, S. (2011). Calibration of load and resistance factors in LRFD foundation design specifications. U.S. Department of Transportation (Report No. NUTC R237), Washington, D.C.

[7] Henchi, K., Fafard, M., Talbot, M., & Dhatt, G. (1998). An efficient algorithm for dynamic analysis of bridges under moving vehicles using a coupled modal and physical components approach. *Journal of Sound and Vibration*, *212*(4), 663-683.

[8] Marchesiello, S., Fasana, A., Garibaldi, L., & Piombo, B. A. D. (1999). Dynamics of multi-span continuous straight bridges subject to multi-degrees of freedom moving vehicle excitation. *Journal of Sound and Vibration*, *224*(3), 541-561.

[9] Yang, Y. B., & Wu, Y. S. (2001). A versatile element for analyzing vehicle–bridge interaction response. *Engineering structures*, *23*(5), 452-469.

[10] Zhu, X. Q., & Law, S. S. (2002). Dynamic load on continuous multi-lane bridge deck from moving vehicles. *Journal of Sound and Vibration*, *251*(4), 697-716.

[11] Law, S. S., & Zhu, X. Q. (2005). Bridge dynamic responses due to road surface roughness and braking of vehicle. *Journal of Sound and Vibration*, *282*(3), 805-830.

[12] Bu, J. Q., Law, S. S., & Zhu, X. Q. (2006). Innovative bridge condition assessment from dynamic response of a passing vehicle. *Journal of Engineering Mechanics*, *132*(12), 1372-1379.

[13] Yang, Y. B., & Chang, K. C. (2009). Extraction of bridge frequencies from the dynamic response of a passing vehicle enhanced by the EMD technique.*Journal of sound and vibration*, *322*(4), 718-739.

[14] Pakrashi, V., O'Connor, A., & Basu, B. (2010). A bridge–vehicle interaction based experimental investigation of damage evolution. *Structural Health Monitoring*. 9, 285-296.

[15] Yang, M., & Papagiannakis, A. T. (2010). A coupled honeycomb composite sandwich bridge-vehicle interaction model. *Journal of Mechanics of Materials and Structures*, *5*(4), 617-635.

[16] Zhang, Y., Wang, L., & Xiang, Z. (2012). Damage detection by mode shape squares extracted from a passing vehicle. *Journal of Sound and Vibration*, *331*(2), 291-307.

[17] González, A., OBrien, E. J., & McGetrick, P. J. (2012). Identification of damping in a bridge using a moving instrumented vehicle. *Journal of Sound and Vibration*, *331*(18), 4115-4131.

[18] Zhang, Y., Lie, S. T., & Xiang, Z. (2013). Damage detection method based on operating deflection shape curvature extracted from dynamic response of a passing vehicle. *Mechanical Systems and Signal Processing*, *35*(1), 238-254.

[19] McGetrick, P., Kim, C. W., & González, A. (2013). Dynamic axle force and road profile identification using a moving vehicle. *Engineering and Construction*, *2*, 1-16.

[20] Malekjafarian, A., & OBrien, E. J. (2014). Identification of bridge mode shapes using short time frequency domain decomposition of the responses measured in a passing vehicle. *Engineering Structures*, *81*, 386-397.

[21] Li, Y., Cai, C. S., Liu, Y., Chen, Y., & Liu, J. (2016). Dynamic analysis of a large span specially shaped hybrid girder bridge with concrete-filled steel tube arches. *Engineering Structures*, *106*, 243-260.

[22] Au, F. T. K., Cheng, Y. S., & Cheung, Y. K. (2001). Effects of random road surface roughness and long-term deflection of prestressed concrete girder and cable-stayed bridges on impact due to moving vehicles. *Computers & Structures*, *79*(8), 853-872.

[23] Yin, X., Fang, Z., & Cai, C. S. (2010). Lateral vibration of high-pier bridges under moving vehicular loads. *Journal of bridge engineering*, *16*(3), 400-412.

[24] Zhong, H., Yang, M., & Gao, Z. J. (2015). Dynamic responses of prestressed bridge and vehicle through bridge-vehicle interaction analysis. *Engineering Structures*, *87*, 116-125.

[25] Cai, C. S., Shi, X. M., Araujo, M., & Chen, S. R. (2007). Effect of approach span condition on vehicle-induced dynamic response of slab-on-girder road bridges. *Engineering Structures*, *29*(12), 3210-3226.

[26] Zhang, H. L., & Hu, C. S. (2007). Determination of allowable differential settlement in bridge approach due to vehicle vibrations. *Journal of Bridge Engineering*, *12*(2), 154-163.

[27] Zhang, H. L. (2010). Determination of allowable differential settlement between bridge abutment and approach embankment with five-degree-of-freedom vehicle model. *International Journal of Pavement Research and Technology*, *3*(6), 311-319.

[28] Ahmari, S., Yang, M., & Zhong, H. (2015). Dynamic interaction between vehicle and bridge deck subjected to support settlement. *Engineering Structures*, *84*, 172-183.

[29] Zhou, D. (1994). Eigenfrequencies of line supported rectangular plates.*International Journal of Solids and Structures*, *31*(3), 347-358.

[30] Wahab, M. A., & De Roeck, G. (1999). Damage detection in bridges using modal curvatures: application to a real damage scenario. *Journal of Sound and Vibration*, *226*(2), 217-235.

[31] International Organization for Standardization (ISO). Mechanical vibration-road surface profiles-reporting of measured data. ISO 8068: 1995 (E), ISO. Geneva, 1995.

CHAPTER 4. PRESTRESS LOSS IDENTIFICATION BASED ON DYNAMIC VEHICLE RESPONSE

4.1. Abstract

Nowadays, how to detect the prestress loss of the bridge in a fast and economical way is still a challenging problem. Although some sensors have been developed to monitor the prestress, it is usually difficult and expensive to install, maintain and monitor these sensors. Drive-by inspection, using vehicle response to identify the prestress loss, could be a good alternative. In this chapter, earlier-developed prestressed bridge vehicle interaction model has been modified to account for the influence of effective rigidity and the gravity load. Both half and quarter vehicle models were adopted in the study. Numerical simulations have been conducted to show that light, low-frequency vehicles moving at low speeds have a better performance in detecting the bridge prestress loss than the heavy, high-frequency vehicles with high speeds.

4.2. Introduction

In recent years, prestressed concrete has been extensively used in the construction of bridges for its unique advantages such as reduction in self-weight and enhancement of crack resistance. Based on the data from US Department of Transportation [1], nearly 44% of all new and replaced bridges built in US between 2009 and 2010 were prestressed bridges. Also, they make up 9% of all structurally deficient bridges in the US [2]. Prestress loss is one of key reasons for the structural deficiency of prestressed bridges. Plenty of researches have been conducted to detect the prestress force in the structure. Ahlborn et al. [3] bonded the electrical-resistance strain gauges to steel strands to estimate the prestress forces and its losses. Kim et al. [4,5] proposed to utilize the change of model parameters such as natural frequencies to identify the prestress-loss in prestressed concrete beams or girders. Lu and Law [6] used the measured

structural response (strain or acceleration) to inversely analyze the prestress force. Ultrasonic waves have been used to identify the load levels of prestressed strands [7-10]. Recently, the use of fiber optic sensors has been extensively researched to monitor the prestress force in bridge [11-16]. However, the above methods are based on the measurement of response of the bridge. They all require the deployment of sensors and measurement equipment on bridges, which is not only costly but also inconvenient.

Yang et al. [17-20] proposed to extract natural frequencies of the bridge through the vehicle acceleration and successfully conducted a field experiment to validate this idea. This method only needs a few sensors installed on the vehicle, and works without interrupting the ongoing traffic, which is efficient and appealing. Encouraged by Yang's work, Gonzalez et al. [21] and Malekjafarian et al. [22] investigated the possibility of identifying damping and mode shapes of the bridge through measurement of the vehicle response, respectively. Prestress force as a significant parameter of prestressed bridge also might be detected using vehicle responses, which is the aim of the present study.

From a theoretical view of point, the existence of axial force in an elastic homogeneous beam would result in the decrease of stiffness of the beam. However, Saiidi et al. [23] conducted field and laboratory tests to find out that the actual stiffness of the prestressed concrete bridge increases with the applied prestress force, for which he named as "effective rigidity" and confirmed by Kim et al. [4,5]. The gain of stiffness might be due to the closure of microcracks.

In this chapter, first, the governing equation for the prestressed bridge vibration has been updated to take the gravity load into account; second, effective rigidity has been adopted in the study and effects of prestress force and road surface roughness have been investigated through half vehicle model; third, a simple quarter vehicle model has been employed to find out the best

vehicle parameters in detecting the prestress loss of the bridge. It is hoped that results given in this paper will help identifying the prestress loss of the bridge in future.

4.3. Theory Background

4.3.1. Updated Equation of Motion for the Prestressed Bridge

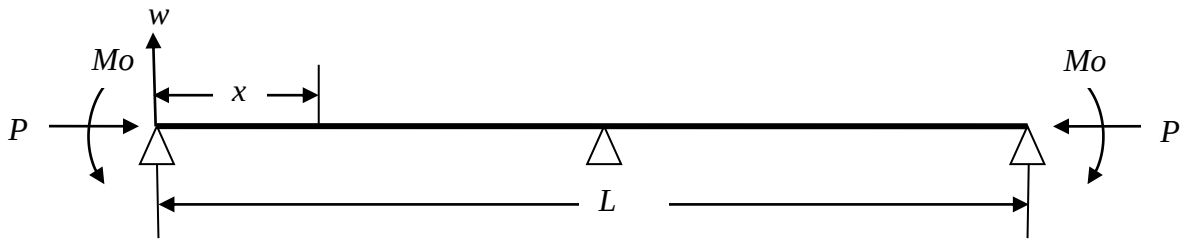

Fig. 4.1. Schematic of an eccentrically two-span continuous prestressed bridge

As shown in Fig. 4.1, a two-span continuous eccentrically-prestressed bridge can be simplified as a continuous beam subjected to one axial force (P) and one initial moment (M_o) at the two ends.

Based on the modal superposition principle, dynamic deflection $w(x,t)$ of the beam can be described as:

$$w(x,t) = \sum_{i=1}^{N} W_i(x)\, q_i(t) \tag{4.1}$$

where $W_i(x)$, $q_i(t)$, and N are the i^{th} mode shape function of the beam, the corresponding modal amplitude of the beam, and the selected number of mode shapes respectively.

According to the principle of virtual displacement, the external virtual work δW_E is equal to the internal virtual work δW_I:

$$\delta W_E = \delta W_I \tag{4.2}$$

The virtual displacements $\delta q_i W_i(x)$, i=1,2,…,N, are selected to be consistent with the assumed shape functions. The external virtual work is the sum of the works (δW_{in}, δW_{gL}, δW_V, δW_C, δW_P and δW_{M_o}) performed by the inertia force ($\overline{m}\frac{\partial^2 w}{\partial t^2}$), the gravity load ($\overline{m}g$), the

moving vehicle tire loads (F_b^{int}), the damping forces ($-c_{bi}\frac{\partial w}{\partial t}$) , the prestress force (P), and the moment (M_o), which can be written as:

$$\delta W_E = \delta W_{in} + \delta W_{gL} + \delta W_V + \delta W_C + \delta W_P + \delta W_{M_o} \tag{4.3}$$

where

$$\delta W_{in} = -\delta q_i \int_0^L W_i(x)\bar{m}\frac{\partial^2 w}{\partial t^2}dx$$

$$\delta W_{gL} = -\delta q_i \int_0^L \bar{m}gW_i(x)dx$$

$$\delta W_V = \delta q_i \int_0^L \sum_{k=1}^2 F_b^{int}(k)\,\delta[x - \widehat{x_k}(t)]W_i[\widehat{x_k}(t)]dx$$

$$\delta W_C = -\delta q_i \int_0^L c_{bi}(\frac{\partial w}{\partial t})W_i(x)dx \quad c_{bi} = 2\bar{m}\omega_i\zeta_i$$

$$\delta W_P = \delta q_i \int_0^L P\left(\frac{\partial w}{\partial x}\right)W_i'(x)dx$$

$$\delta W_{M_o} = \delta q_i[M_o W_i'(0) - M_o W_i'(L)] \tag{4.4}$$

and $\bar{m}$ is the mass of the beam per unit length; g is the acceleration of gravity; ω_i, ζ_i, c_{bi} is the natural frequency, damping ratio and damping coefficient for the i^{th} mode of the beam respectively; $F_b^{int}(k)$ is the k^{th} interaction force between the wheel of the vehicle and the bridge; $\widehat{x_k}(t)$ is the location of the k^{th} interaction force $F_b^{int}(k)$; $\delta(x)$ is the Dirac function; $W_i'(x)$ denotes the first derivative of $W_i(x)$ with respect to x.

The internal virtual work performed by the bending moment is:

$$\delta W_I = \delta q_i \int_0^L EI\left(\frac{\partial^2 w}{\partial x^2}\right)W_i''(x)dx \tag{4.5}$$

where EI is flexural rigidity of the beam; $W_i''(x)$ denotes the second derivative of $W_i(x)$ with respect to x.

Substituting Eq. (4.1) and Eqs. (4.3) ~ (4.5) into Eq. (4.2) and cancelling δq_i at both sides give

$$\sum_{j=1}^{N} \ddot{q}_j M_{bij} + \sum_{j=1}^{N} \dot{q}_j C_{bij} + \sum_{j=1}^{N} q_j (K_{bij} - K_{Gij}) = (W_V)_i + (W_{gL})_i + \left(W_{M_o}\right)_i \quad (4.6)$$

where

$$M_{bij} = \int_0^L \bar{m} W_i(x) W_j(x) dx \qquad K_{bij} = \int_0^L EI W_i''(x) W_j''(x) dx$$

$$K_{Gij} = \int_0^L P W_i'(x) W_j'(x) dx \qquad C_{bij} = \int_0^L c_{bi} W_i(x) W_j(x) dx$$

$$(W_V)_i = \sum_{k=1}^{2} F_b^{int}(k)\, W_i\left(\widehat{x_k}(t)\right) \qquad \left(W_{gL}\right)_i = -\int_0^L \bar{m} g W_i(x) dx$$

$$\left(W_{M_o}\right)_i = M_o W_i'(0) - M_o W_i'(L) \quad (4.7)$$

, $\dot{q}_j$ and $\ddot{q}_j$ denote the first and second derivative of $q_j(t)$ with respect to time *t*.

Corresponding to the N independent virtual displacements $\delta q_i W_i(x)$, *i*=1,2,…,N, there are N virtual work equations in the form of Eq. (4.6). Together they can be expressed in matrix form as:

$$\boldsymbol{M_b}\ddot{\boldsymbol{Q}} + \boldsymbol{C_b}\dot{\boldsymbol{Q}} + (\boldsymbol{K_b} - \boldsymbol{K_G})\boldsymbol{Q} = \boldsymbol{W_V} + \boldsymbol{W_{gL}} + \boldsymbol{W_{M_o}} \quad (4.8)$$

where

$$\boldsymbol{Q} = \{q_1(t), q_2(t), \dots, q_N(t)\}^T \qquad \boldsymbol{W_V} = W_b F_b^{int}$$

$$\boldsymbol{W_b} = \begin{bmatrix} W_1(\widehat{x_1}(t)) & W_1(\widehat{x_2}(t)) \\ & \vdots \\ W_N(\widehat{x_1}(t)) & W_N(\widehat{x_2}(t)) \end{bmatrix} \qquad \boldsymbol{F_b^{int}} = \begin{bmatrix} F_{t1} \\ F_{t2} \end{bmatrix}$$

$$\boldsymbol{W_{gL}} = \begin{Bmatrix} -\int_0^L \bar{m} g W_1(x) dx \\ \vdots \\ -\int_0^L \bar{m} g W_N(x) dx \end{Bmatrix} \qquad \boldsymbol{W_{M_o}} = \begin{Bmatrix} M_o[W_i'(0) - W_i'(L)] \\ \vdots \\ M_o[W_N'(0) - W_N'(L)] \end{Bmatrix} \quad (4.9)$$

, $\boldsymbol{M_b}$, $\boldsymbol{K_b}$, $\boldsymbol{C_b}$ and $\boldsymbol{K_G}$ are the mass, stiffness, damping, and geometric stiffness matrices of the bridge respectively with their (*i*, *j*)th element calculated in Eq. (4.7); $\dot{\boldsymbol{Q}}$, $\ddot{\boldsymbol{Q}}$ are the first and second derivatives of $\boldsymbol{Q}$ with respect to time *t*; F_{t1}, F_{t2} are the bridge-vehicle interaction forces at the front and rear wheel locations shown in Eq. (4.20).

In reality, due to the gravity load or self-weight and the applied prestress, the prestressed bridge has an initial deflection $w_o(x)$ before it vibrates under the moving vehicle loads. In other words, the total initial deflection of the bridge can be regarded as a combination of the deflections due to the self-weight $w_{o,gL}(x)$ and the prestress $w_{o,P}(x)$. These deflections can be calculated in a mode-analysis way by using Eq. (4.8) with $(\dot{\boldsymbol{Q}})_{\boldsymbol{t=0}} = (\ddot{\boldsymbol{Q}})_{\boldsymbol{t=0}} = (\boldsymbol{W_V})_{t=0} = [\boldsymbol{0}]_{\boldsymbol{N\times 1}}$ at the time t = 0, which are shown in Eq. (4.10) as follows:

$$w_o(x) = w_{o,gL}(x) + w_{o,P}(x)$$

$$(K_b - K_G)Q_{0,gL} = W_{gL} \qquad (K_b - K_G)Q_{0,P} = W_{M_o}$$

$$w_{o,gL}(x) = WQ_{0,gL} \qquad w_{o,P}(x) = WQ_{0,P} \tag{4.10}$$

where

$$\boldsymbol{W} = \{W_1(x), W_2(x), \dots, W_N(x)\} \tag{4.11}$$

4.3.2. Modal Analysis for the Prestressed Bridge

For the free vibration of the beam, its vertical deflection can be expressed as:

$$w(x,t) = W(x)e^{i\omega t} \tag{4.12}$$

where ω is the natural frequency of the vibration and $i = \sqrt{-1}$.

The mode shape function of the beam $W(x)$ may be expressed in term of a series as:

$$W(x) = \sum_m A_m \varphi_m(x) \tag{4.13}$$

where $\varphi_m(x)$ is the assumed admissible function satisfying the boundary conditions of the beam and A_m is undermined coefficient. The selection of $\varphi_m(x)$ follows the method proposed by Zhou [24], which composes of free vibrating beam eigenfunctions and polynomials. It is of great importance to note that here the moment (M_o) is taken as an acting force but not a boundary condition.

Now the Rayleigh's method is used to determine the natural frequencies and mode shapes of the prestressed beam. The maximum potential and kinetic energies of the beam over a vibration cycle can be expressed as follows:

$$E_{So} = \int_0^L \left\{ \frac{1}{2} EI \left[\frac{\partial^2 W(x)}{\partial x^2} \right]^2 - \frac{1}{2} P \left[\frac{\partial w}{\partial x} \right]^2 \right\} dx$$

$$E_{Ko} = \int_0^L \frac{1}{2} \bar{m} \omega^2 [W(x)]^2 \, dx \tag{4.14}$$

Substituting Eq. (4.13) into Eq. (4.14) and taking the first derivation of the Rayleigh's quotient with respect to each coefficient A_m would lead to the eigenvalue equations in a matrix form as following:

$$(\boldsymbol{K} - \omega^2 \boldsymbol{M}) \boldsymbol{A} = \boldsymbol{0} \tag{4.15}$$

where

$$\boldsymbol{A} = \{A_1, A_2, \ldots . A_m\}^T$$

$$\boldsymbol{K_{ij}} = \int_0^L [EI \varphi_i''(x) \varphi_j''(x) - P \varphi_i'(x) \varphi_j'(x)] dx$$

$$\boldsymbol{M_{ij}} = \int_0^L \bar{m} \varphi_i(x) \varphi_j(x) dx \qquad (i = 1, 2, \cdots, m; j = 1, 2, \cdots, m) \tag{4.16}$$

, m is the number of assumed admissible functions; $\varphi_i'(x)$, $\varphi_i''(x)$ are the first and second derivatives of $\varphi_i(x)$ with respect to x.

The natural frequencies ω and coefficients A_m can be determined from Eq. (4.15). Then the mode shape functions of the beam $W(x)$ can be determined through Eq. (4.13).

4.3.3. Effective Flexural Rigidity of the Prestressed Bridge

Saiidi et al. [23] conducted field and laboratory tests on prestressed concrete bridge and beams, and found that the actual rigidity of these members increased with the prestress force applied on them, for which they described as "Effective Rigidity" and proposed an equation to calculate it. The equation is shown as following:

$$(\boldsymbol{EI})_{\boldsymbol{e}} = \left(1 + 1.75\frac{N}{f_c'}\right)\boldsymbol{EI_g} \tag{4.17}$$

where N is the applied axial force, positive as compression; f_c' is the standard 28-day concrete compressive strength; $\boldsymbol{EI_g}$ is the rigidity of the beam without prestress.

Eq. (4.17) accounts for the stiffness increase of the member due to the prestress force applied on them and will be used in the following numerical simulations to study the effect of prestress on dynamic bridge and vehicle responses.

4.3.4. Vehicle Model

To better understand the bridge-vehicle interaction, a half-vehicle vibration model shown in Fig. 4.2 is adopted in current study. This vehicle model has four degrees of freedom, corresponding to the vertical displacement of vehicular body (z_c), rotation of vehicular body about the transverse axis (θ_c), the vertical displacements of the front wheel (z_f) and rear wheel (z_r).

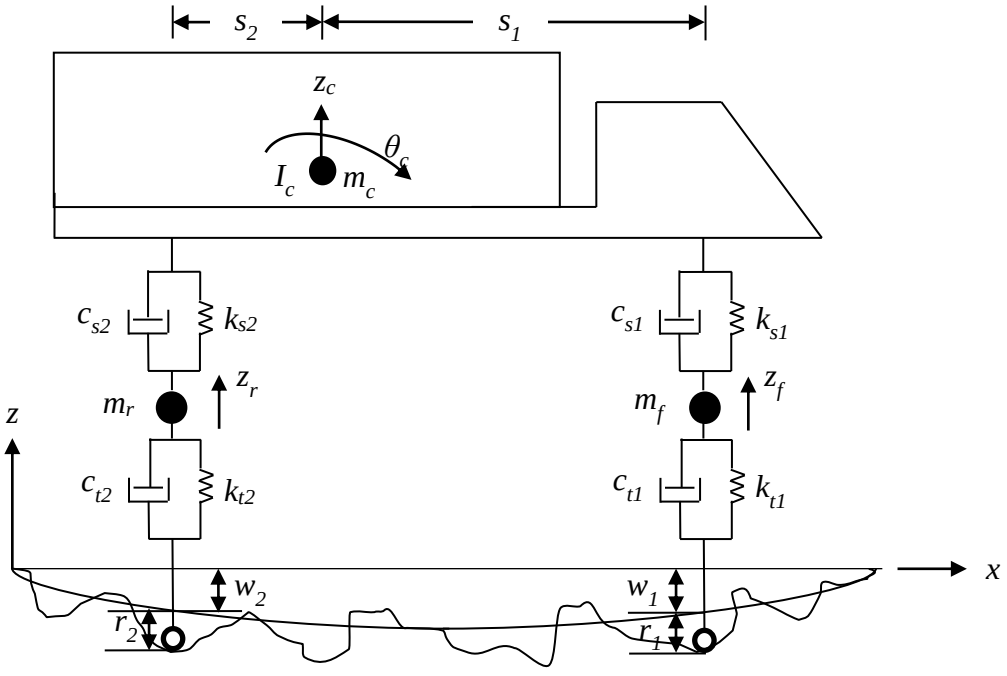

Fig. 4.2. Half-vehicle vibration model

Applying the Lagrange method, the equations of motion for the half-vehicle model can be derived and expressed in a matrix form as following:

$$\boldsymbol{M_v}\ddot{\boldsymbol{Z}} + \boldsymbol{C_v}\dot{\boldsymbol{Z}} + \boldsymbol{K_v}\boldsymbol{Z} = \boldsymbol{F_v^{int}} \tag{4.18}$$

where

$$\boldsymbol{Z} = \begin{bmatrix} Z_c \\ \theta_c \\ Z_f \\ Z_r \end{bmatrix} \qquad \boldsymbol{M_v} = \begin{bmatrix} m_c & 0 & 0 & 0 \\ 0 & I_c & 0 & 0 \\ 0 & 0 & m_f & 0 \\ 0 & 0 & 0 & m_r \end{bmatrix} \qquad \boldsymbol{F_v^{int}} = \begin{bmatrix} 0 \\ 0 \\ k_{t1}(w_1 + r_1) + c_{t1}(\dot{w}_1 + \dot{r}_1) \\ k_{t2}(w_2 + r_2) + c_{t2}(\dot{w}_2 + \dot{r}_2) \end{bmatrix}$$

$$\boldsymbol{C_v} = \begin{bmatrix} c_{s1} + c_{s2} & s_2c_{s2} - s_1c_{s1} & -c_{s1} & -c_{s2} \\ s_2c_{s2} - s_1c_{s1} & s_1^2c_{s1} + s_2^2c_{s2} & s_1c_{s1} & -s_2c_{s2} \\ -c_{s1} & s_1c_{s1} & c_{s1} + c_{t1} & 0 \\ -c_{s2} & -s_2c_{s2} & 0 & c_{s2} + c_{t2} \end{bmatrix}$$

$$\boldsymbol{K_v} = \begin{bmatrix} k_{s1} + k_{s2} & s_2k_{s2} - s_1k_{s1} & -k_{s1} & -k_{s2} \\ s_2k_{s2} - s_1k_{s1} & s_1^2k_{s1} + s_2^2k_{s2} & s_1k_{s1} & -s_2k_{s2} \\ -k_{s1} & s_1k_{s1} & k_{s1} + k_{t1} & 0 \\ -k_{s2} & -s_2k_{s2} & 0 & k_{s2} + k_{t2} \end{bmatrix} \tag{4.19}$$

, $\dot{\boldsymbol{Z}}$, $\ddot{\boldsymbol{Z}}$ are the first and second derivatives of $\boldsymbol{Z}$ with respect to time t; m_c, I_c, m_f, m_r are half of vehicular body mass, half of vehicular body lateral mass moment of inertia, the mass of a front wheel, and the mass of a rear wheel respectively; k_{s1}, k_{s2}, c_{s1}, c_{s2} are the stiffness and damping coefficients of the front and rear suspensions respectively; k_{t1}, k_{t2}, c_{t1}, c_{t2} are the stiffness and damping coefficients of the front and rear tires respectively; s_1, s_2 are the distance of the center of gravity of the vehicular body from the front and rear axles respectively; w_1, w_2 are the deflection of the bridge at the location of the front and rear wheels respectively; and $\dot{w}_1$, $\dot{w}_2$ are the first derivative of w_1, w_2 with respect to time *t*; r_1, r_2 are the surface roughness of the bridge pavement at the location of the front and rear wheels respectively; $\dot{r}_1$, $\dot{r}_2$ are the first derivative of r_1, r_2 with respect to time *t*. Note that the vehicle displacement vector $\boldsymbol{Z}$ is measured from the static equilibrium position of the vehicle, which leads to no gravity term in Eq. (4.18).

4.3.5. Bridge-Vehicle Interaction Force

The bridge-vehicle interaction forces for a single vehicle can be described as follows:

$$F_{t1} = k_{t1}(Z_f - w_1 - r_1) + c_{t1}(\dot{Z}_f - \dot{w}_1 - \dot{r}_1) - \left(m_f + m_c \frac{s_2}{s_1+s_2}\right) g$$
$$F_{t2} = k_{t2}(Z_r - w_2 - r_2) + c_{t2}(\dot{Z}_r - \dot{w}_2 - \dot{r}_2) - (m_r + m_c \frac{s_1}{s_1+s_2}) g \quad (4.20)$$

4.3.6. Road Surface Roughness of the Bridge

Road surface roughness can be described by the power spectral density (PSD) of its vertical displacement. The general form of the displacement PSD can be expressed as [25]:

$$G_d(n) = G_d(n_0)(\frac{n}{n_0})^{-w} \quad (4.21)$$

where n is the spatial frequency (cycle/m); n_0 (=0.1 cycle/m) is the reference spatial frequency; w is the exponent of the PSD, which is taken as 2 in the present study.

In the space domain, road surface roughness can be simulated by applying the inverse fast Fourier transformation on $G_d(n)$ as following [26]:

$$r(x) = \sum_{i=1}^{N} \sqrt{4G_d(i \cdot \Delta n)\Delta n}\ \cos(2\pi \cdot i \cdot \Delta n \cdot x + \varphi_i) \quad (4.22)$$

where x is the horizontal ordinate of the road profile from 0 to L; L is the length of the road profile; $\Delta n = 1/L$; $N = L/B$; B is the sampling interval of the road profile; φ_i is a set of randomly generated phase angle following an uniform probabilistic distribution within the 0–2π range.

4.4. Numerical Simulations

4.4.1. Numerical Algorithm

The dynamic responses of the bridge and vehicle can be calculated from Eqs. (4.8), (4.9), (4.18), (4.19), and (4.20) using the Newmark-β method. The implementation procedure of the Newmark integration method is shown in Fig. 4.3, in which v is the speed of the vehicle and

Error representing the difference between the results of two consecutive iterations is defined as following:

$$Error = \sqrt{\left[\frac{w_1(x,t)_j - w_1(x,t)_{j-1}}{w_1(x,t)_j}\right]^2 + \left[\frac{w_2(x,t)_j - w_2(x,t)_{j-1}}{w_2(x,t)_j}\right]^2} \quad (4.23)$$

where $w_1(x,t)_{j-1}$, $w_1(x,t)_j$ are the deflection of the bridge at the front wheel location in the $(j-1)^{\text{th}}$ iteration and $(j)^{\text{th}}$ iteration respectively; $w_2(x,t)_{j-1}$, $w_2(x,t)_j$ are the deflection of the bridge at the rear wheel location in the $(j-1)^{\text{th}}$ iteration and the $(j)^{\text{th}}$ iteration respectively.

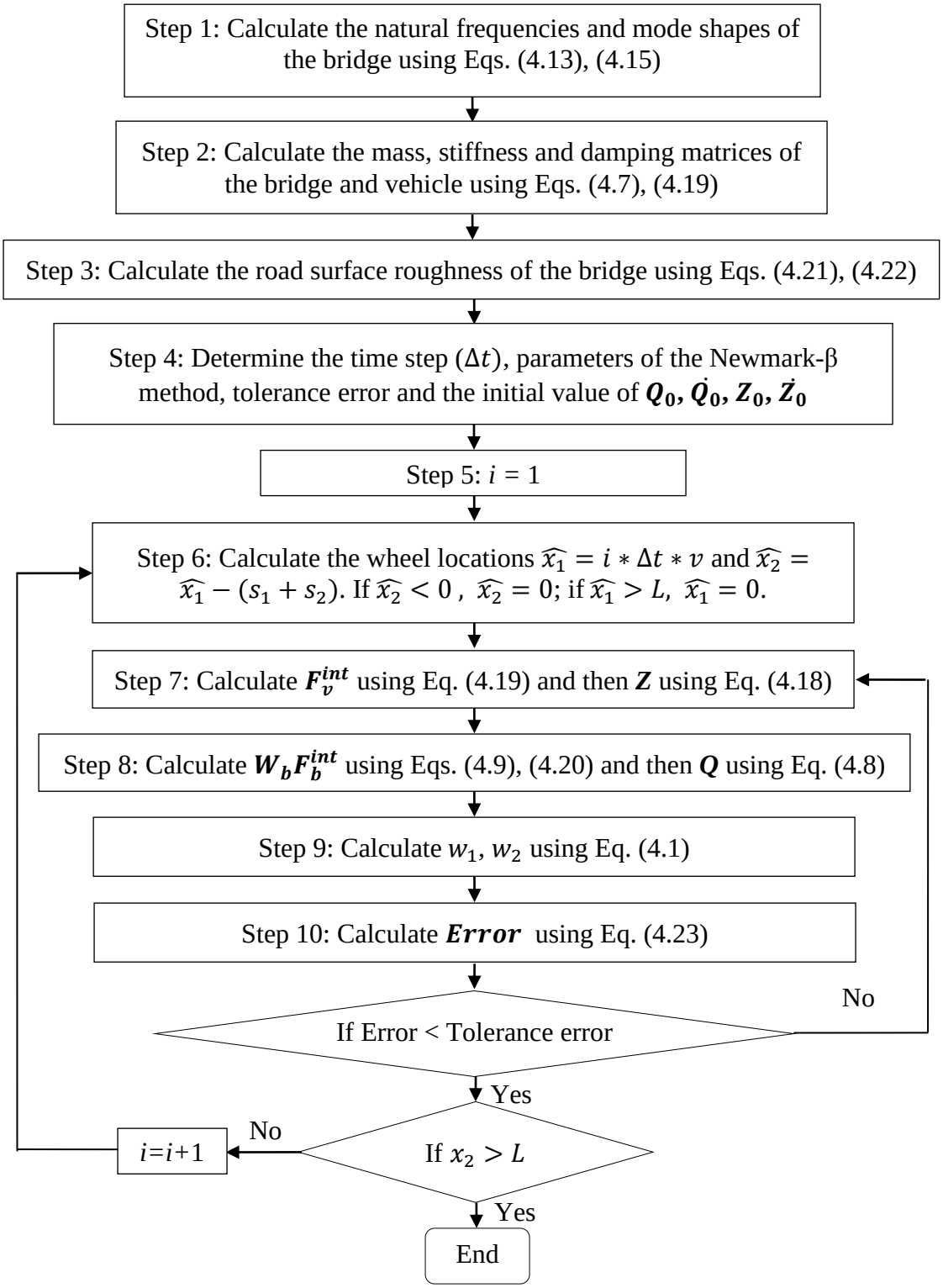

Fig. 4.3. Flow chart of implementation

4.4.2. Verification

A two-span eccentrically prestressed continuous bridge as shown in Fig. 4.1 will be used to verify the bridge model developed in preceding sections. Properties of the bridge are listed as following: overall span length L = 30+30 = 60 m, flexural rigidity EI_g = 5.6×10^9 N·m^2, mass per unit length $\bar{m}$ = 1920 kg/m, axial force P = 8.0×10^6 N, initial moment M_o = 8.8×10^6 N·m and f_c' = 4.14×10^7 N·m^2. Note that the effective rigidity of the bridge EI_e needs to be calculated first according to Eq. (4.17) and it is the one that will be used in the following verification and further simulations.

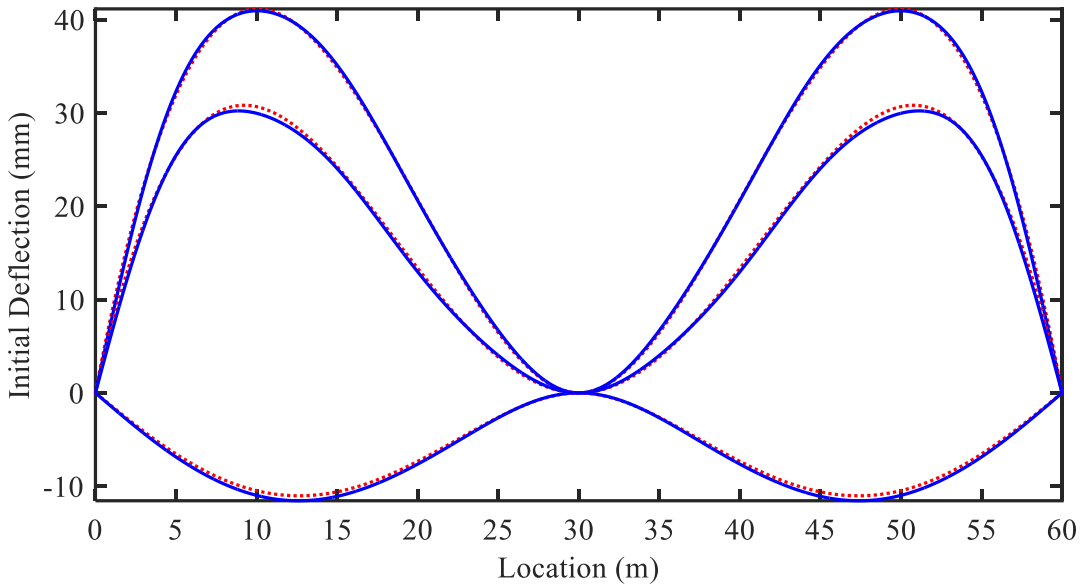

Fig. 4.4. Initial deflection of a two-span continuous eccentrically-prestressed beam
Proposed method; Theoretical result.

The initial deflections of the bridge due to the gravity load and applied prestress have been calculated through Eq. (4.10) and then compared with the theoretical result obtained by solving the classical beam differential equation. The superposition of those two deflections composes the total initial deflection of the bridge. As can be seen from Fig. 4.4, the modal

analysis result and theoretical result get very close to each other, indicating the effectiveness and accuracy of the proposed method.

4.4.3. Study with Half Vehicle Model

Numerical simulations following the algorithm shown in Section 4.4.1 were conducted to investigate the effect of prestress on the dynamic bridge and vehicle responses, considering different amplitudes of prestress force and road surface roughness conditions. The same bridge properties as that in verification part were used through the study. The half vehicle model shown in Fig. 4.2 is adopted in the present study with the vehicle parameters listed as following: m_c = 8500 kg, I_c = 4.5×10^4 kg·m^2, m_f = 300 kg, m_r= 500 kg, k_{s1} = 1.16×10^5 N/m, k_{s2} = 3.73×10^5 N/m, k_{t1} = 7.85×10^5 N/m, k_{t2} = 1.57×10^6 N/m, c_{s1} = 2.5×10^4 N·sec/m, c_{s2} = 3.5×10^4 N·sec/m, c_{t1} = 100 N·sec/m, c_{t2} = 200 N·sec/m.

In this study, a program was coded in Matlab to compute the bridge and vehicle dynamic responses using the Newmark-β method with γ = 0.5 and β = 0.25, which implies a constant average acceleration over a time step with unconditional stability. The first 10 modes of the bridge were used in the calculation with a damping coefficient of 0.02 for all the modes. A time step of 0.0001 sec was selected and the tolerance error between two consecutive iterations was set to be 0.01.

4.4.3.1. Comparison of results with or without using effective rigidity

As stated earlier in Section 4.3.3, the actual flexural rigidity of a prestressed bridge increases with the applied force and can be empirically calculated using Eq. (4.17). The following paragraphs will discuss the difference effective rigidity contributes by comparing results with or without using it.

Table 4.1 lists the natural frequencies of bridges calculated by using gross rigidity (EI_g) and effective rigidity $(EI)_e$. As can be seen, bridge frequencies decrease with the prestress force if (EI_g) is used, in contrast, the adoption of $(EI)_e$ makes the frequencies increase, indicating the gain of flexural stiffness with the prestress force. Although the bridge frequencies change with the prestress force, the amplitude of change is tiny, not large enough to be used for prestress loss identification in practice.

Table 4.1. Natural frequencies of bridges (Hz)

Mode	EI_g				$(EI)_e$			
	0%	60%	80%	100%	0%	60%	80%	100%
1	2.981	2.862	2.821	2.780	2.981	3.161	3.219	3.276
2	4.661	4.573	4.543	4.513	4.661	5.032	5.150	5.265
3	11.923	11.806	11.766	11.727	11.923	12.971	13.302	13.624
4	15.137	15.036	15.002	14.968	15.137	16.511	16.944	17.366
5	26.826	26.710	26.671	26.632	26.826	29.318	30.102	30.867
6	31.692	31.585	31.550	31.514	31.692	34.663	35.599	36.510
7	47.691	47.575	47.536	47.497	47.691	52.203	53.623	55.006
8	54.472	54.363	54.326	54.289	54.472	59.647	61.275	62.860
9	74.518	74.401	74.362	74.323	74.518	81.627	83.863	86.041
10	83.826	83.714	83.676	83.639	83.826	91.841	94.361	96.816

The maximum static and dynamic deflections of the prestressed bridge calculated with gross rigidity (EI_g) and effective rigidity $(EI)_e$ are plotted in Fig. 4.5. It can be observed that the deflection values obtained by (EI_g) are much larger than that for $(EI)_e$, as well as the variation between static and dynamic deflections, which leads to larger impact factors associated with (EI_g) than those corresponding to $(EI)_e$ as shown in Fig. 4.6.

As a result of the excessive deflection and larger impact factor due to (EI_g), an over-conservative prestressed bridge design may result, which necessitates the use of effective rigidity $(EI)_e$ to obtain a practical and economical design. In the following sections, $(EI)_e$ will be used.

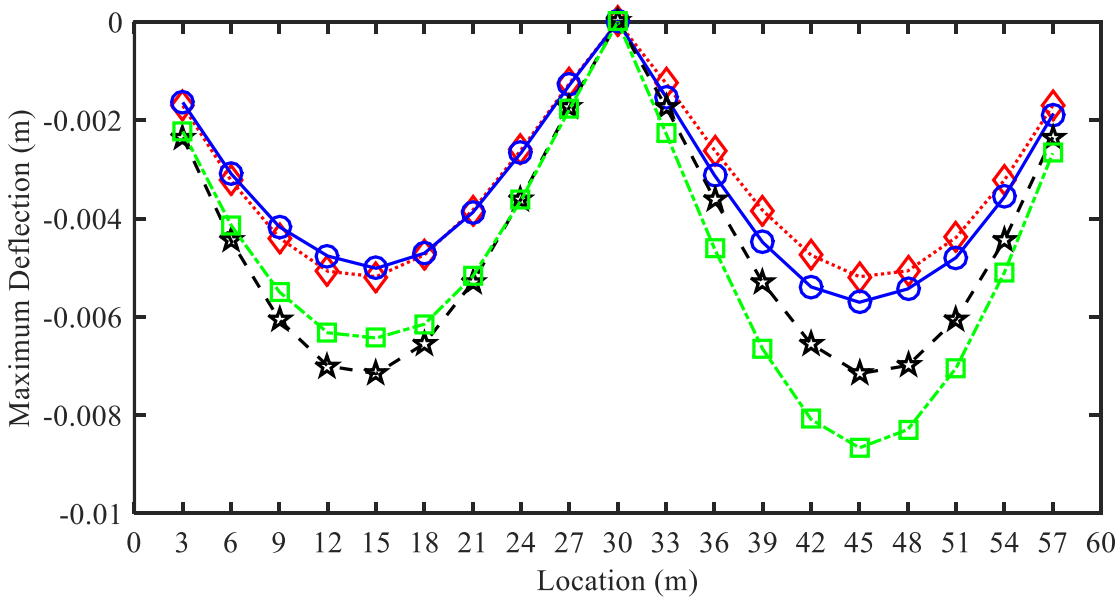

Fig. 4.5. Maximum deflection of the bridge under the moving vehicle load
$(EI)_e$ - Static; $(EI)_e$ - Dynamic; EI_g - Static; EI_g - Dynamic.

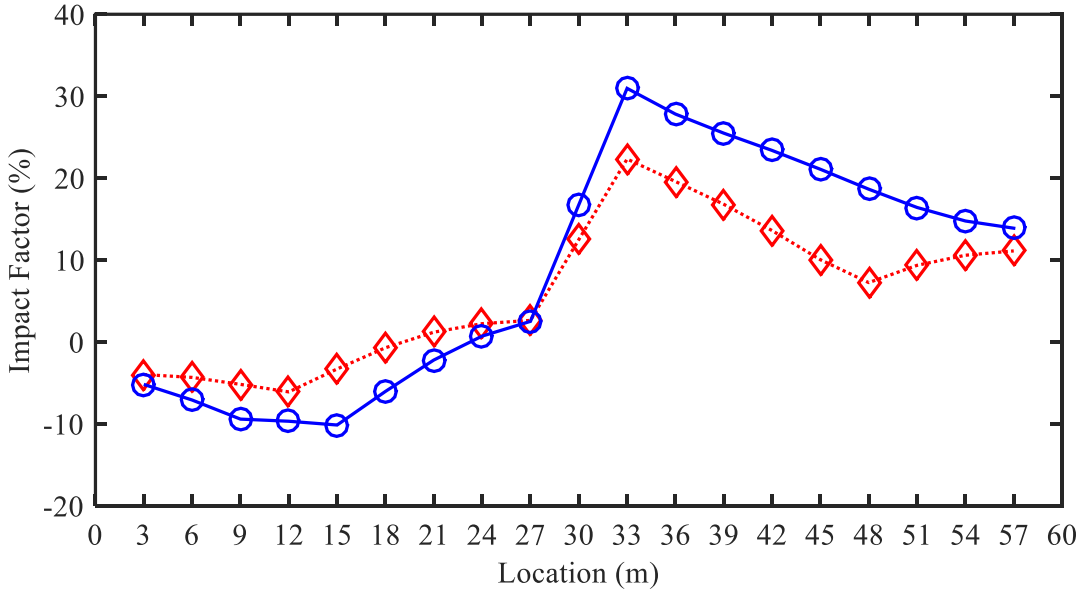

Fig. 4.6. Distribution of impact factor along the bridge
$(EI)_e$; EI_g.

4.4.3.2. Effect of prestress force

Fig. 4.7 shows the impact factor of the bridge subjected to different amplitudes of prestress force and moving vehicle loads. It can be seen that without prestress, the bridge has an impact factor of about 5% to 10% evenly distributed on its two spans, however, under the effect of increasing prestress force, the distribution becomes more and more unbalanced, with higher negative impact factors appearing on the left span of the bridge, the entrance span of the vehicle.

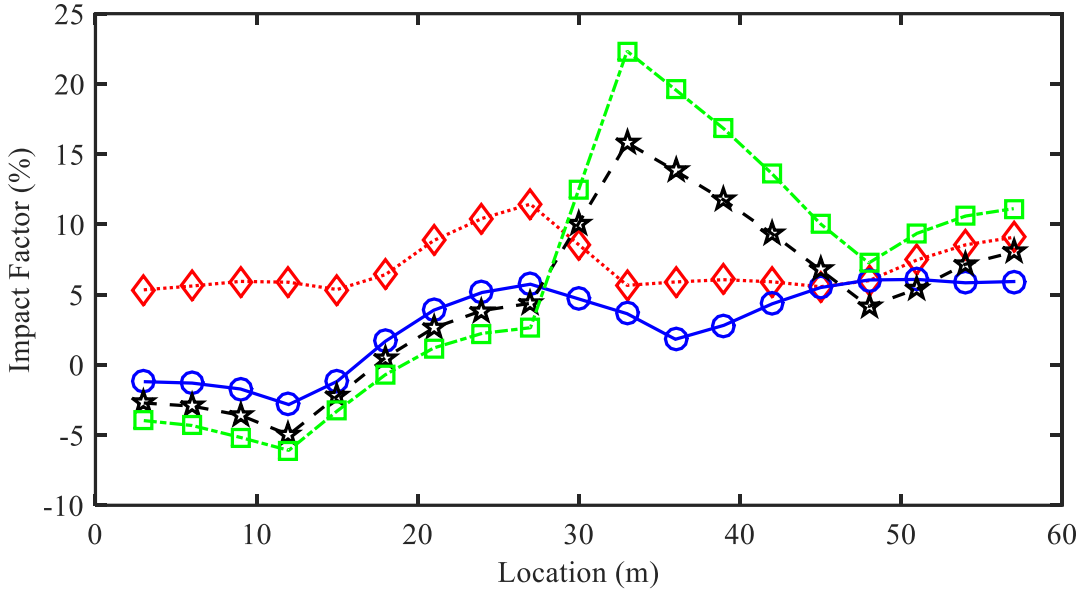

Fig. 4.7. Distribution of impact factor along the bridge
P - 0%; P - 60%; P - 80%; P - 100%.

The time histories of vertical acceleration, front and rear tire force of the vehicle are shown in Figs. 4.8 – 4.10 respectively. From the three figures, one can observe that the vehicle responses travelling on the prestressed bridges share very similar trend with only different amplitudes, and the trend is very different from that for non-prestressed bridge. Furthermore, the amplitude change of vehicle responses closely relates to the amount of prestress force applied on the bridge, which could be a good indicator of the prestress force of the bridge.

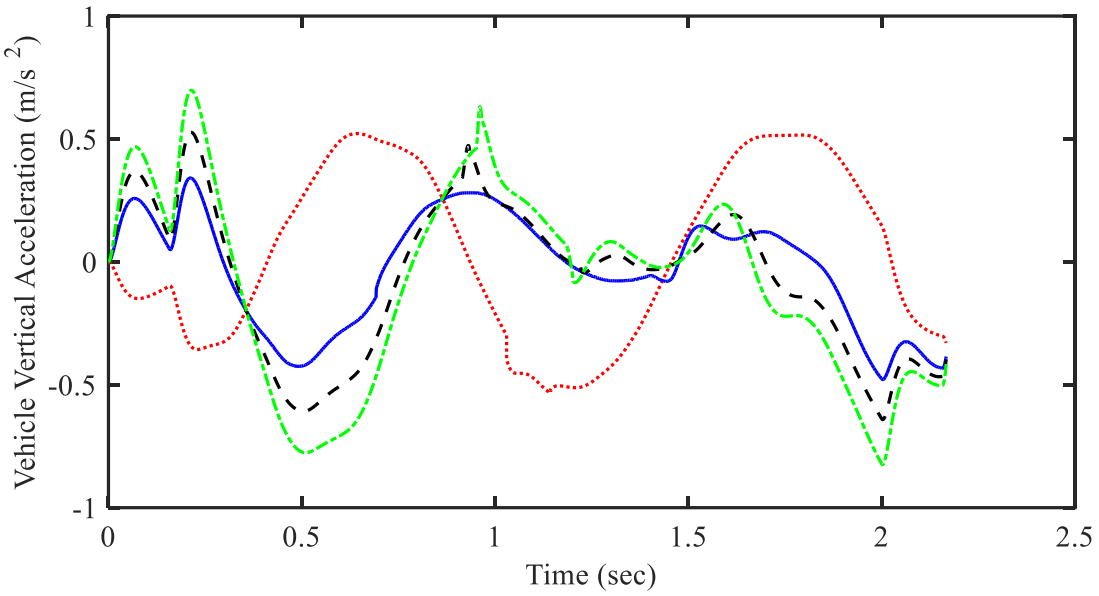

Fig. 4.8. Vertical acceleration of the vehicle

P - 0%; P - 60%; P - 80%; P - 100%

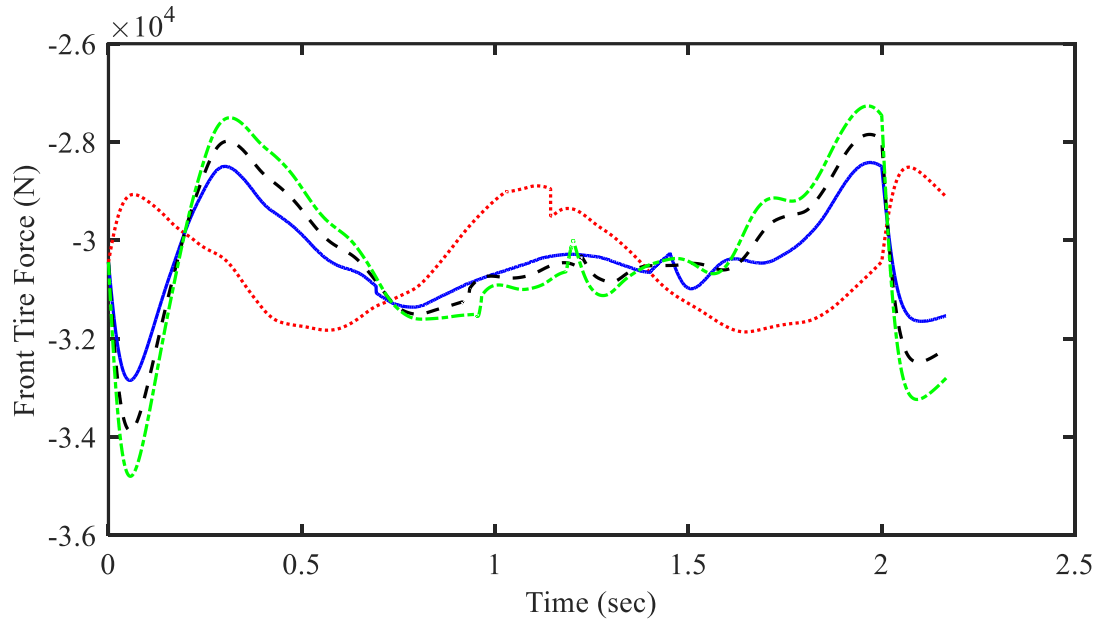

Fig. 4.9. Vehicle front tire force

P - 0%; P - 60%; P - 80%; P - 100%

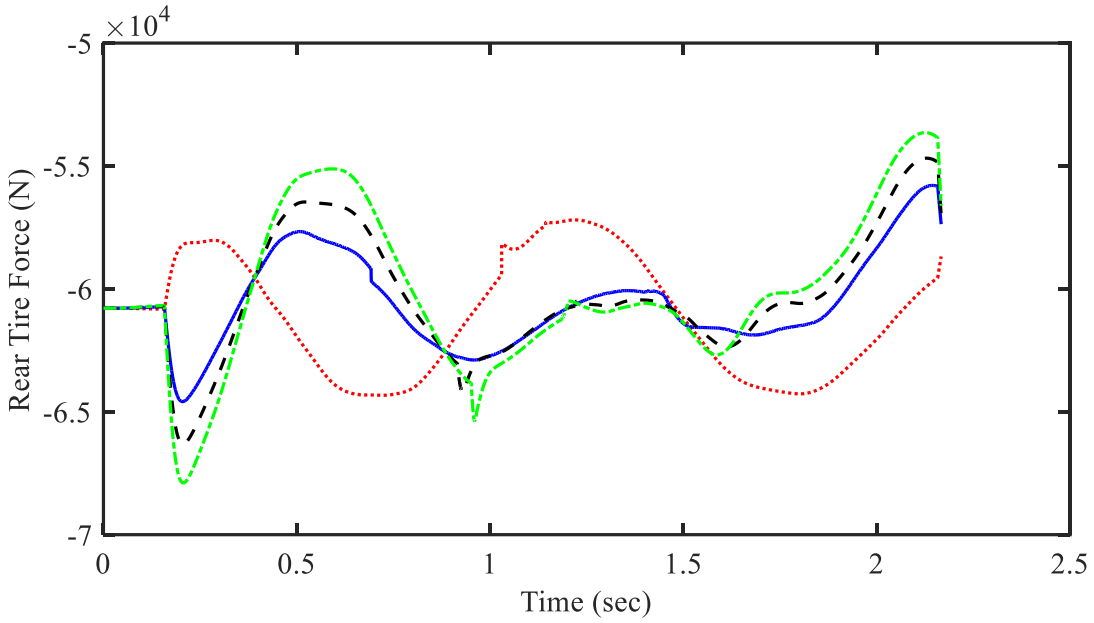

Fig. 4.10. Vehicle rear tire force

P - 0%; P - 60%; P - 80%; P - 100%.

4.4.3.3. Effect of road surface roughness

In the present study, four classes of road surface profile have been used to investigate the effect of surface roughness: Smooth (no roughness), Class A, Class B and Class C. $G_d(n_0)$ in Eq. (21) is a constant dictating the degree of roughness of the road surface, which has a geometric mean of 16×10^{-6} m^3, 64×10^{-6} m^3 and 256×10^{-6} m^3 for Class A, B and C respectively, based on ISO 8608 specifications [25]. Because of the square root shown in Eq. (22), if keeping the other parameters the same except $G_d(n_0)$, a certain relationship exists among the three classes of road profile: $r(x, C)$=2× $r(x, B)$= 4× $r(x, A)$, which means that the amplitude of Class C profile at the same position of x is 2 times larger than Class B and 4 times larger than Class A. Namely, they share the same profile distribution but only different amplitudes. The purpose of doing this is to make the simulation results for different classes of road profile more comparable. Moreover, a constraint of nearly zero value at both ends of the bridge has been

enforced when generating the random surface roughness to ensure a smooth entrance and exit to the bridge for the vehicle, avoiding jump in and jump out.

Figs. 4.11 and 4.12 show the distribution of impact factor of non-prestressed and prestressed bridges under four different road surface roughness profiles respectively. Clear effect of road surface roughness can be observed from Fig. 4.11 for non-prestressed bridge, which is the increase of impact factor due to the higher amplitude of surface roughness. However, with the prestress force, the road roughness effect on impact factor becomes insignificant for prestressed bridge, as can be seen in Fig. 4.12. This can also be observed in Fig. 4.13, which shows the change of impact factor of the non-prestressed and prestressed bridges at the midpoint of two spans with different road surface roughness.

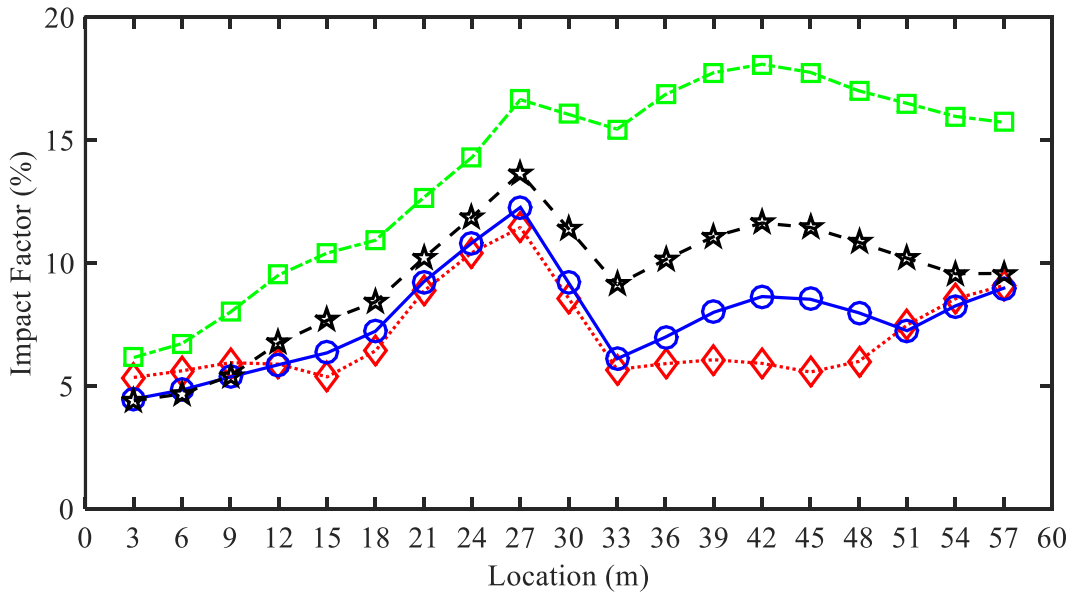

Fig. 4.11. Impact factor of non-prestressed bridge under road surface roughness conditions
Smooth; Class A; Class B; Class C.

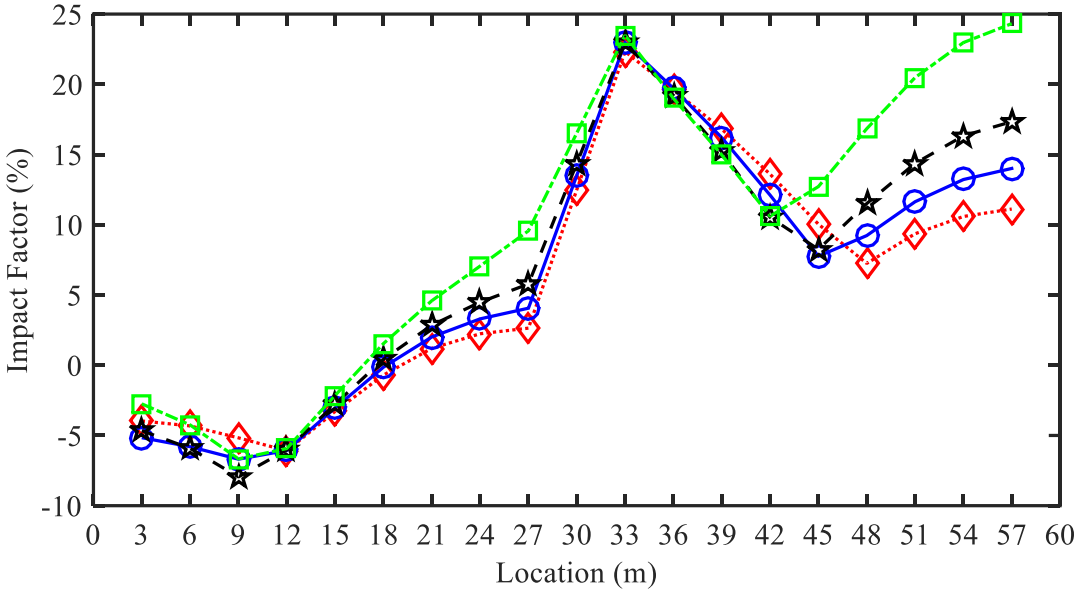

Fig. 4.12. Impact factor of prestressed bridge under road surface roughness conditions
Smooth; Class A; Class B; Class C.

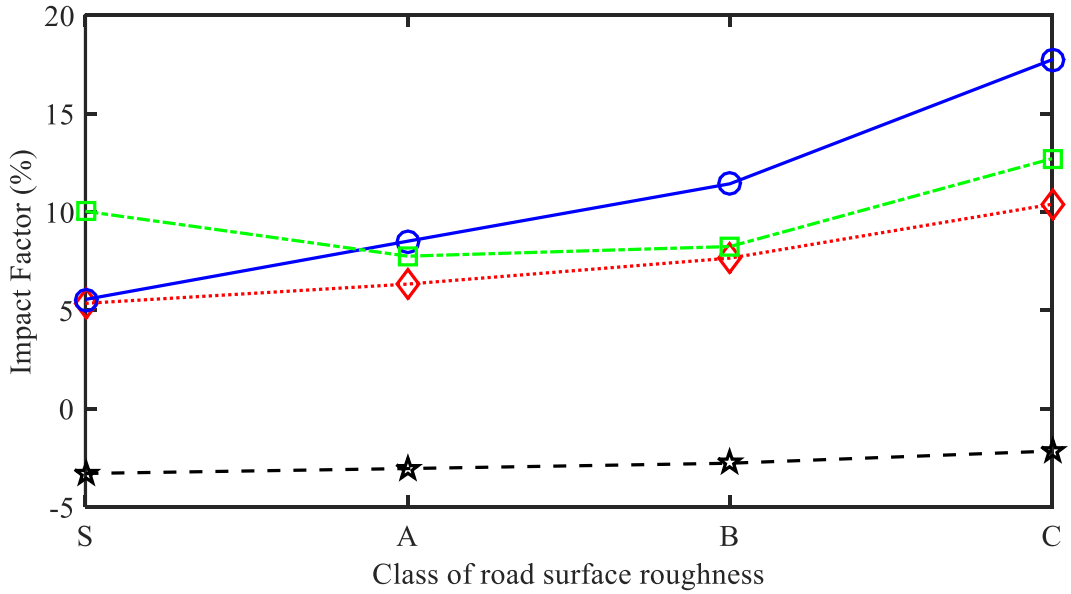

Fig. 4.13. Impact factor of the bridge at the midpoint of two spans
P - 0%, 15 m; P - 0%, 45 m; P -100%, 15 m; P -100%, 45 m.

4.4.3.4. Vehicle response and prestress loss estimation

As stated in the Section 4.4.3.2, without consideration of road surface roughness, the dynamic vehicle responses such as vertical acceleration, front and rear tire forces clearly change

with the prestress force applied on the bridge, which might be used to estimate the prestress loss of the bridge. However, from the practical viewpoint, the bridge deck surface can never be smooth without any roughness. Therefore, bridge vehicle interaction analysis needs to take road surface roughness into account. Since vehicle acceleration is more detectable and easier to monitor than tire forces. In the following sections, emphasis will be placed on acceleration.

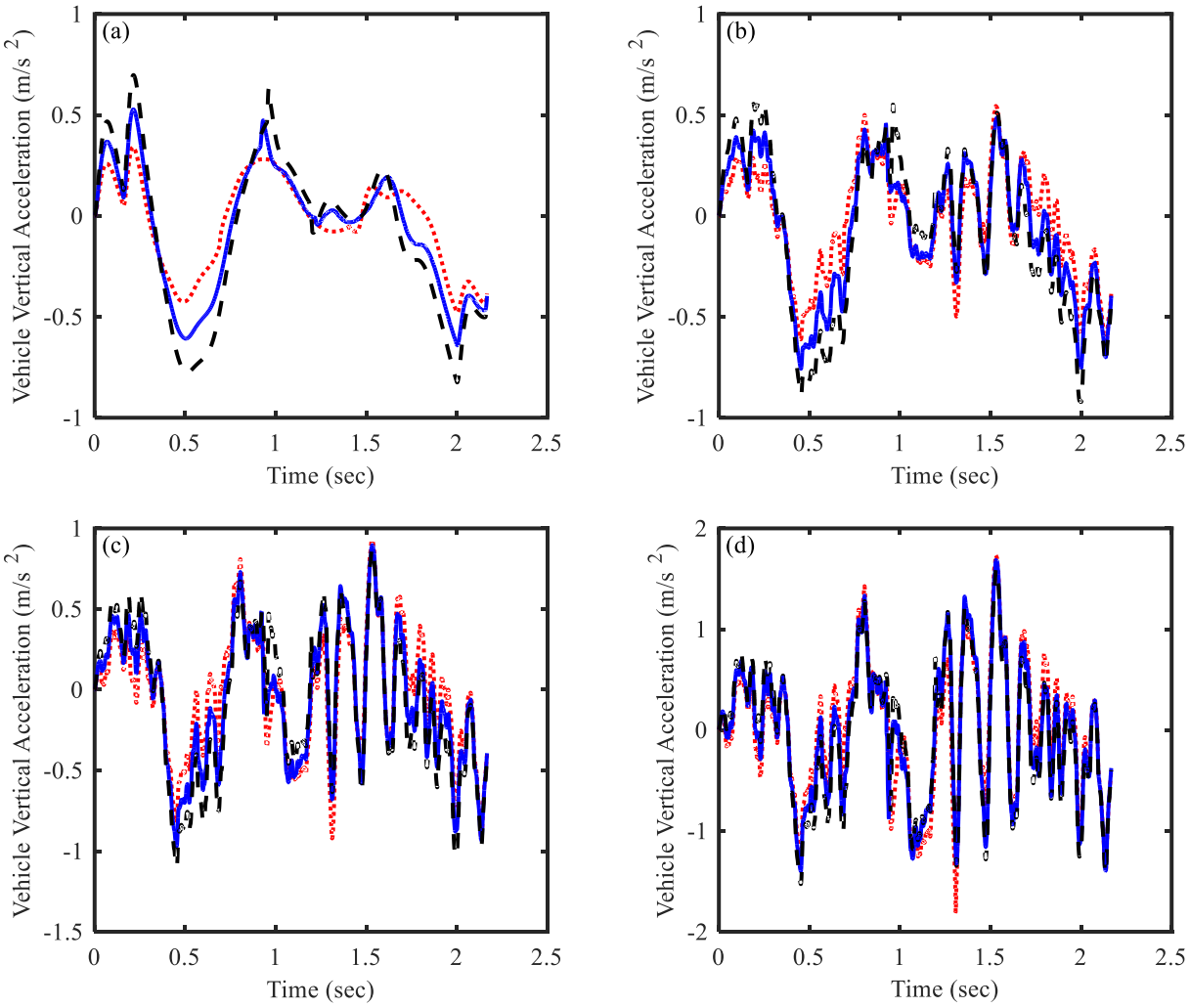

Fig. 4.14. Vehicle vertical acceleration under various prestress forces and road roughness (a) Smooth; (b) Class A; (c) Class B; (d) Class C: ····· P - 60%; ——— P - 80%; – – – – P - 100%.

Fig. 4.14 shows time histories of vehicle vertical acceleration under 60%, 80% and 100% of prestress force for each class of road surface roughness. Vehicle accelerations corresponding

to smooth and Class A road roughness are distinguishable, as can be seen in Fig. 4.14 (a) and (b), while under class B and Class C surface roughness, as shown in Fig. 4.14 (c) and (d), these accelerations get very close to each other, which are unable to identify the prestress loss of the bridge. This also can be observed from Fig. 4.15 that shows the spectrum analysis of the vertical vehicle acceleration in Fig. 4.14. Since it is more convenient to compare vehicle accelerations in frequency domain than in time domain, amplitude spectrums are used in the following sections instead of time histories.

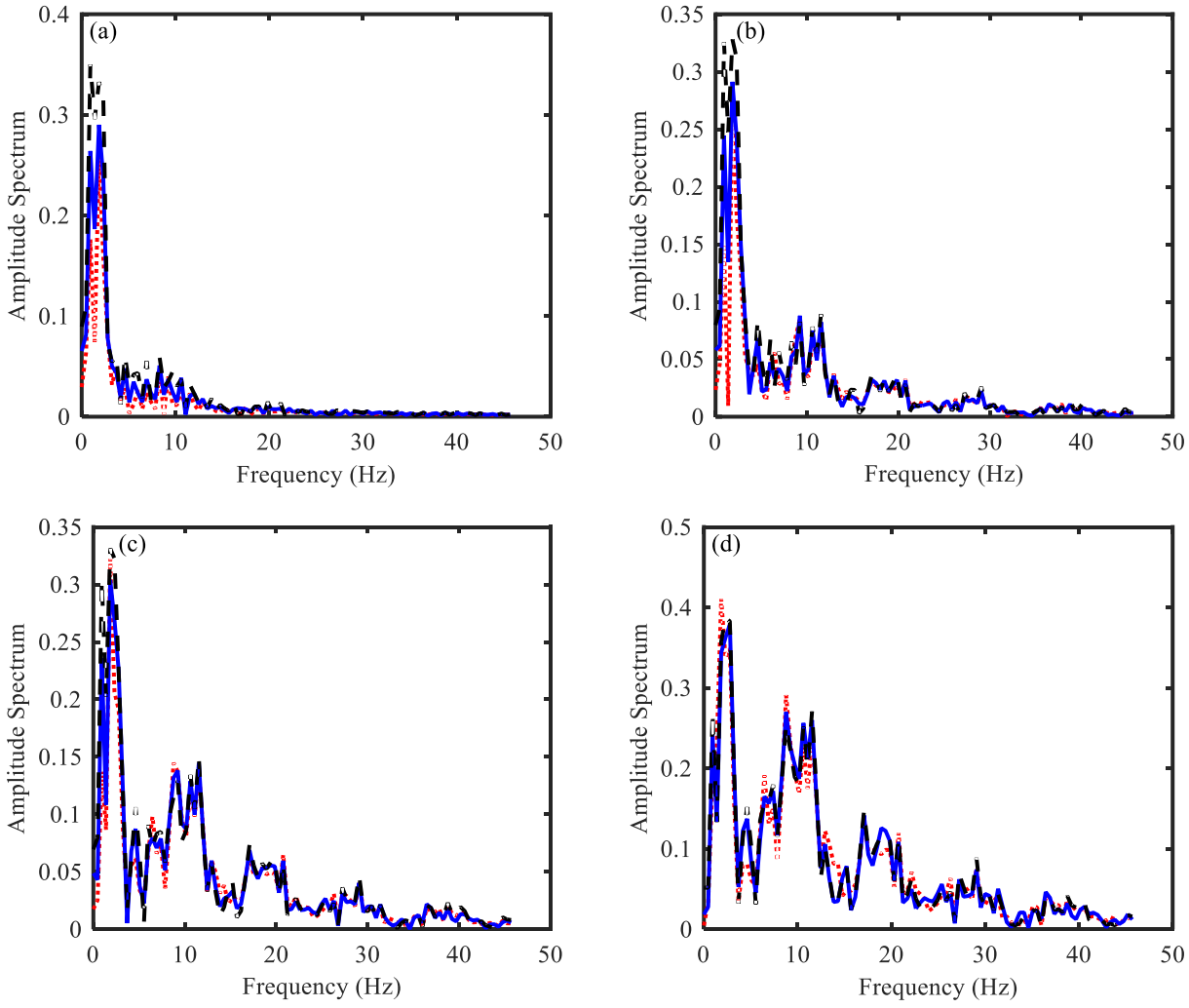

Fig. 4.15. Spectrum analysis of vehicle acceleration under various prestress and road roughness (a) Smooth; (b) Class A; (c) Class B; (d) Class C:
P - 60%; P - 80%; P - 100%.

4.4.4. Study with Quarter Vehicle Model

In the Section of 4.4.3.4, it was noticed that with the road surface becoming rougher, the vehicle accelerations induced were more complicated and closer to each other, which could not be used to identify the prestress loss of the bridge. The reason for that is because the vehicle model used in that section is complex with four degrees of freedom representing a half truck, which makes the vehicle vertical acceleration mixed or contaminated due to road surface roughness.

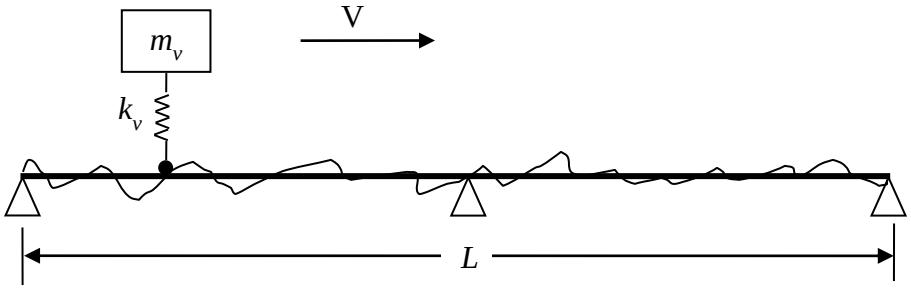

Fig. 4.16. Quarter vehicle traveling on the bridge with surface roughness

To better understand how the vehicle responds to the road roughness and optimize the vehicle parameters to best serve the prestress loss detection, a simple quarter vehicle model as shown in Fig. 4.16 is employed in the study of current section. This model has only one degree of freedom and two parameters of mass m_v and stiffness k_v, which acts like a trailer or compact car travelling on the bridge.

Eight cases with different combinations of vehicle mass and stiffness, as listed in Table 4.2, are investigated in this section. Every two cases like Case 1 and Case 2 share the same natural frequency, with a factor of 10 times between the vehicle mass and stiffness parameters of two cases. Two vehicle speeds of 10 m/s and 30 m/s are considered.

Table 4.2. Properties of quarter vehicles and traveling speed

Case No.	1	2	3	4	5	6	7	8
m_v (kg)	1.0×10^3	1.0×10^4	1.0×10^3	1.0×10^4	1.0×10^3	1.0×10^4	1.0×10^2	1.0×10^3
k_v (N/m)	4.0×10^3	4.0×10^4	4.0×10^4	4.0×10^5	4.0×10^5	4.0×10^6	4.0×10^5	4.0×10^6
f_v (Hz)	**0.32**	**0.32**	1.01	1.01	**3.18**	**3.18**	10.07	10.07
V (m/s)	10							
	30							

Note: $f_v = (\sqrt{k_v/m_v})/(2\pi)$.

Numerical simulations on the interaction between the bridge and quarter vehicles under three different road surface roughness conditions have been conducted and vehicle accelerations were then obtained. Figs. 4.17 - 4.24 show the amplitude spectrum of vehicle acceleration for each case, with subplots of (a), (b) and (c) on the left side of each figure corresponding to the vehicle speed of 10 m/s and the right side for 30 m/s.

The following observations can be obtained from these figures:

- Vehicles with low natural frequencies work better than that with high natural frequencies on bridge prestress loss identification;
- Generally, at low speed of 10 m/s, the vehicles do a better job than they at high speed of 30 m/s;
- With the same natural frequency, the lighter vehicles have a better performance than the heavy ones.

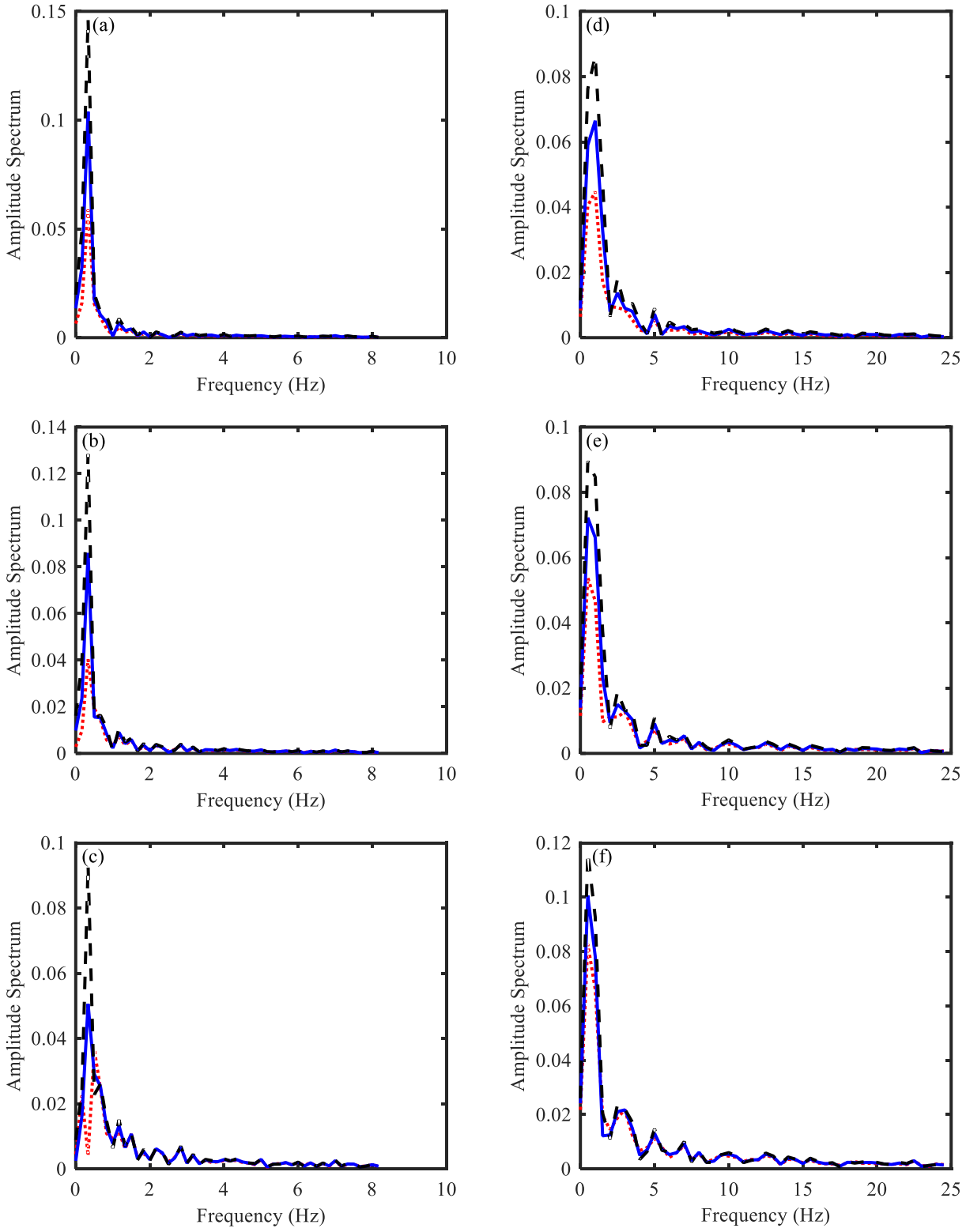

Fig. 4.17. Spectrum analysis of vehicle acceleration (Case 1)
P - 60%; P - 80%; P - 100%.

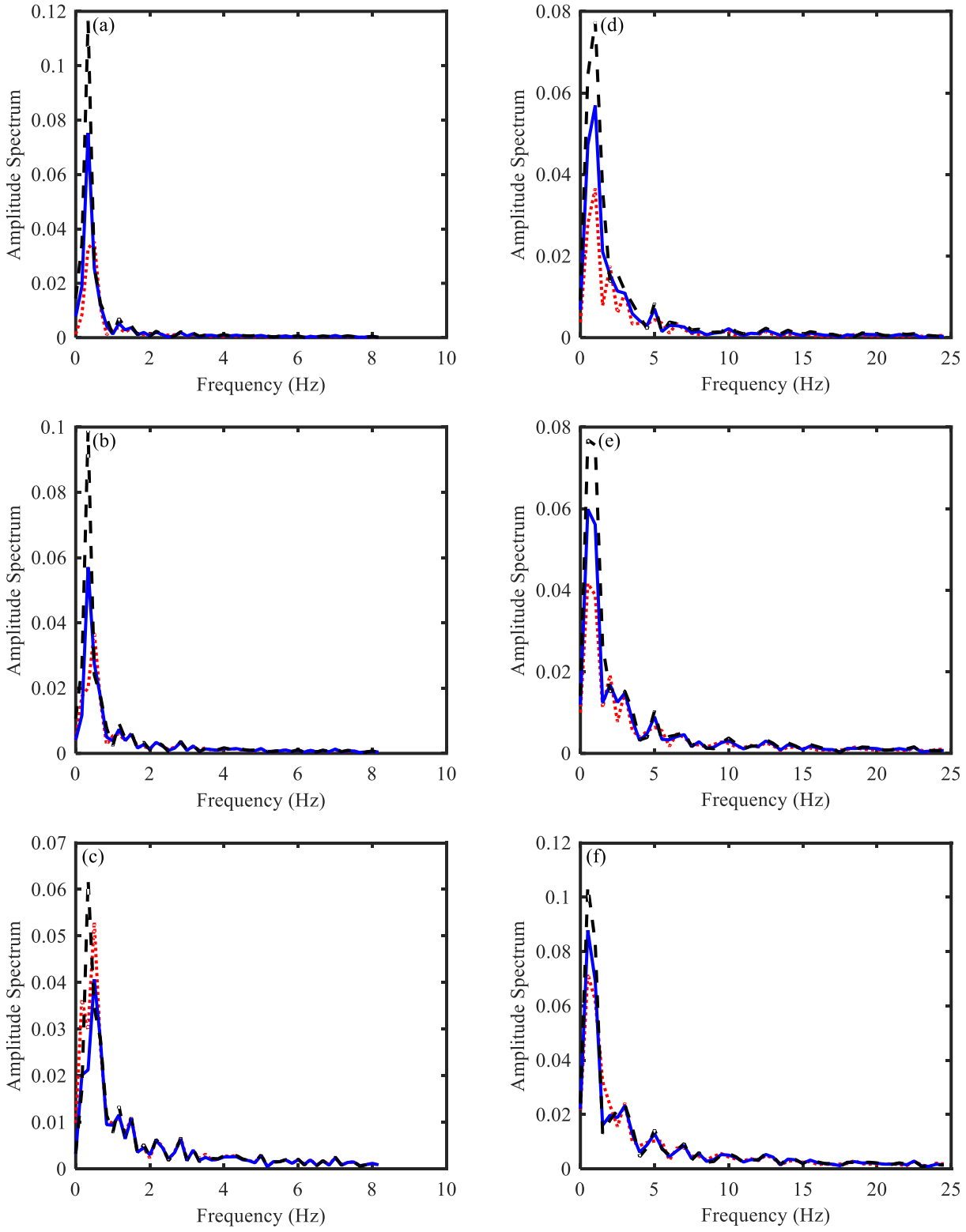

Fig. 4.18. Spectrum analysis of vehicle acceleration (Case 2)
P - 60%; P - 80%; P - 100%.

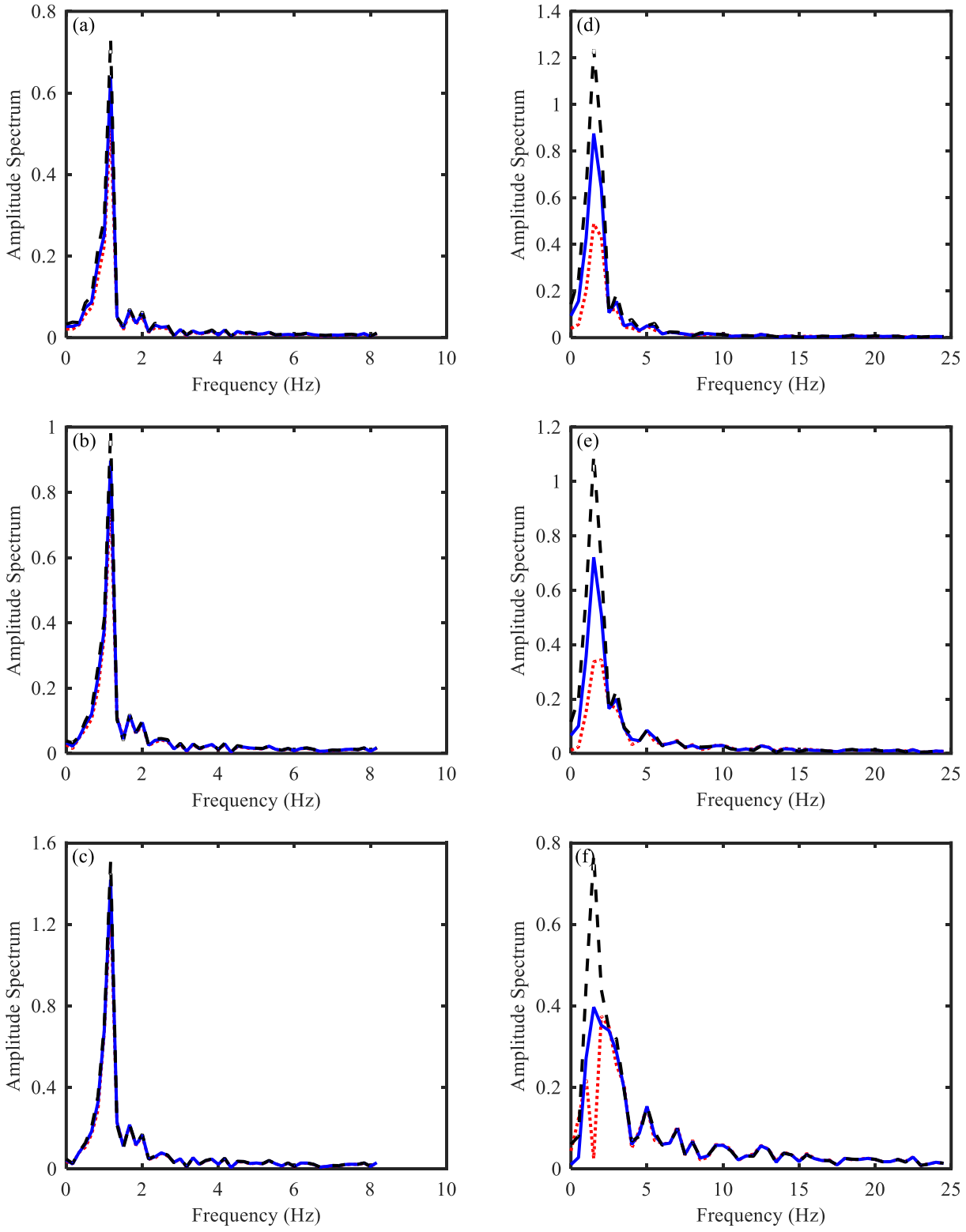

Fig. 4.19. Spectrum analysis of vehicle acceleration (Case 3)
P - 60%; P - 80%; P - 100%.

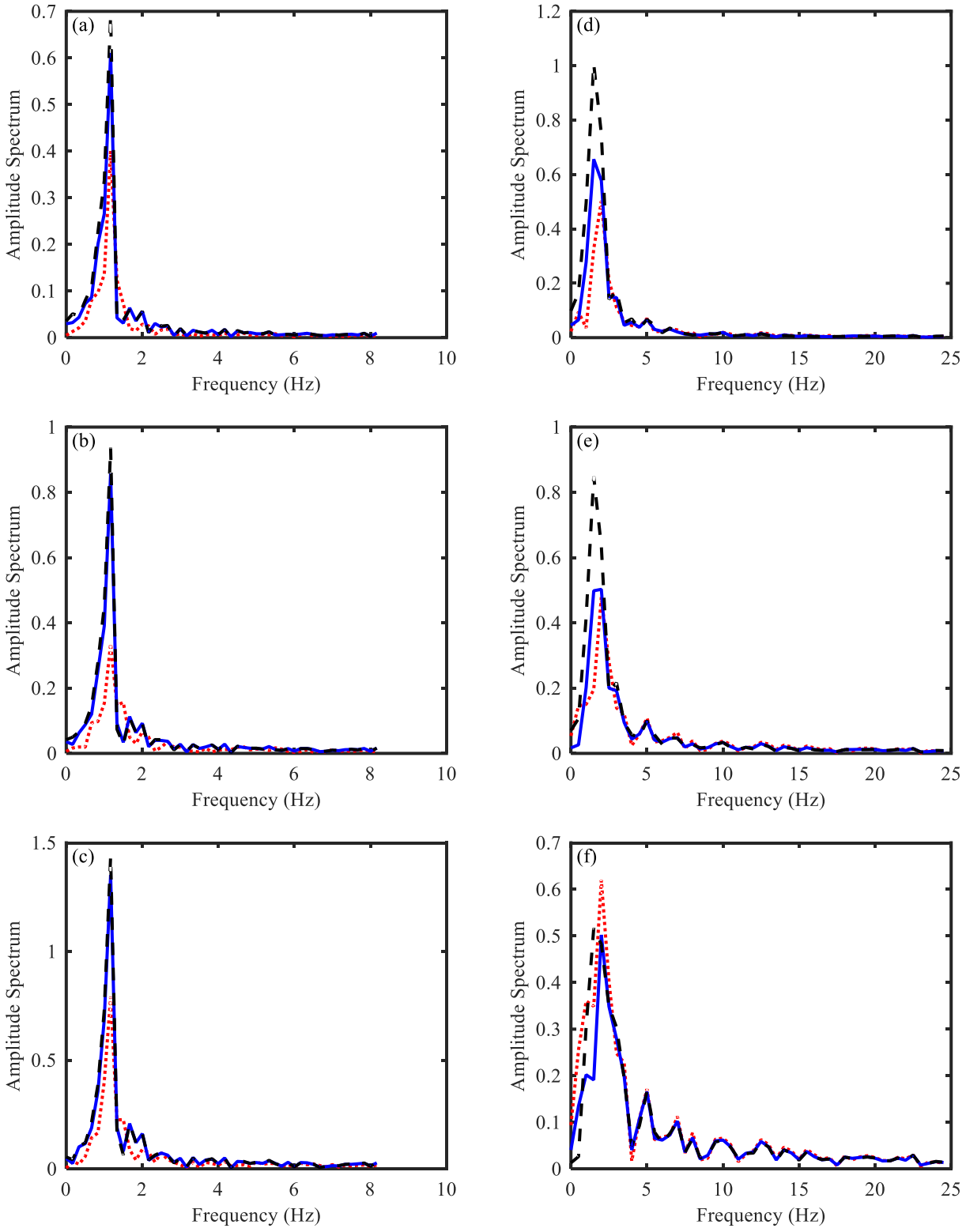

Fig. 4.20. Spectrum analysis of vehicle acceleration (Case 4)
P - 60%; P - 80%; P - 100%.

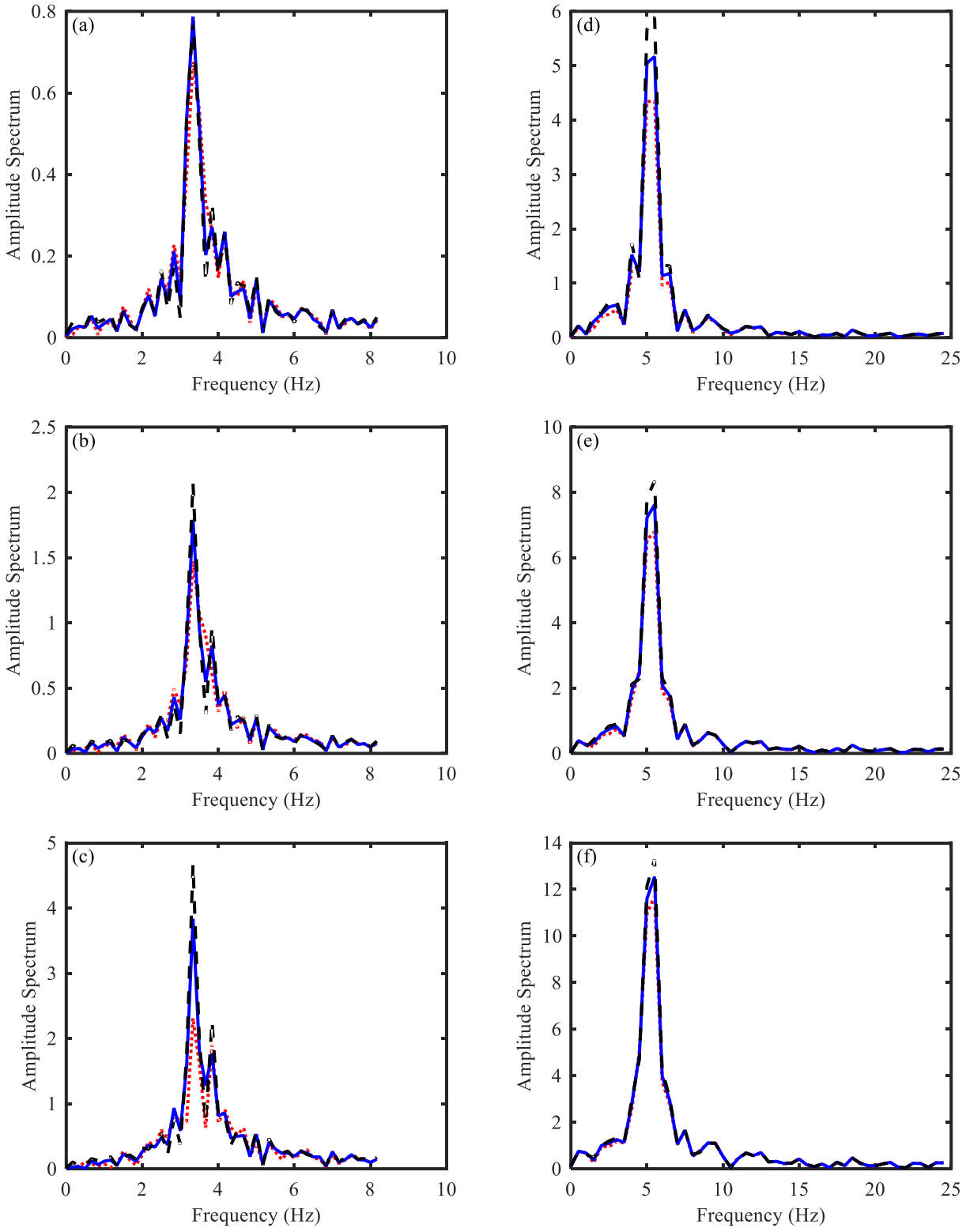

Fig. 4.21. Spectrum analysis of vehicle acceleration (Case 5)
P - 60%; P - 80%; P - 100%.

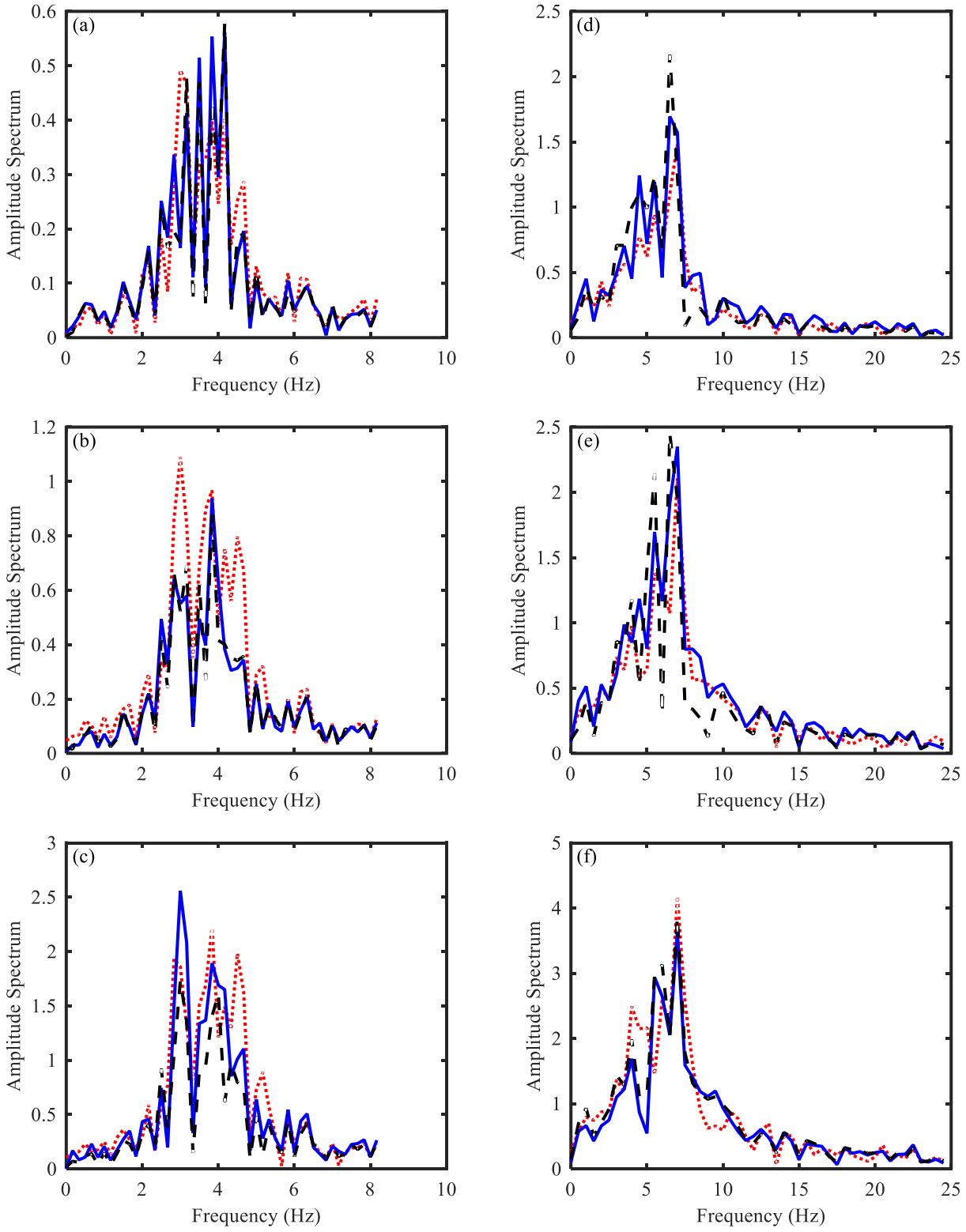

Fig. 4.22. Spectrum analysis of vehicle acceleration (Case 6)
P - 60%; P - 80%; P - 100%.

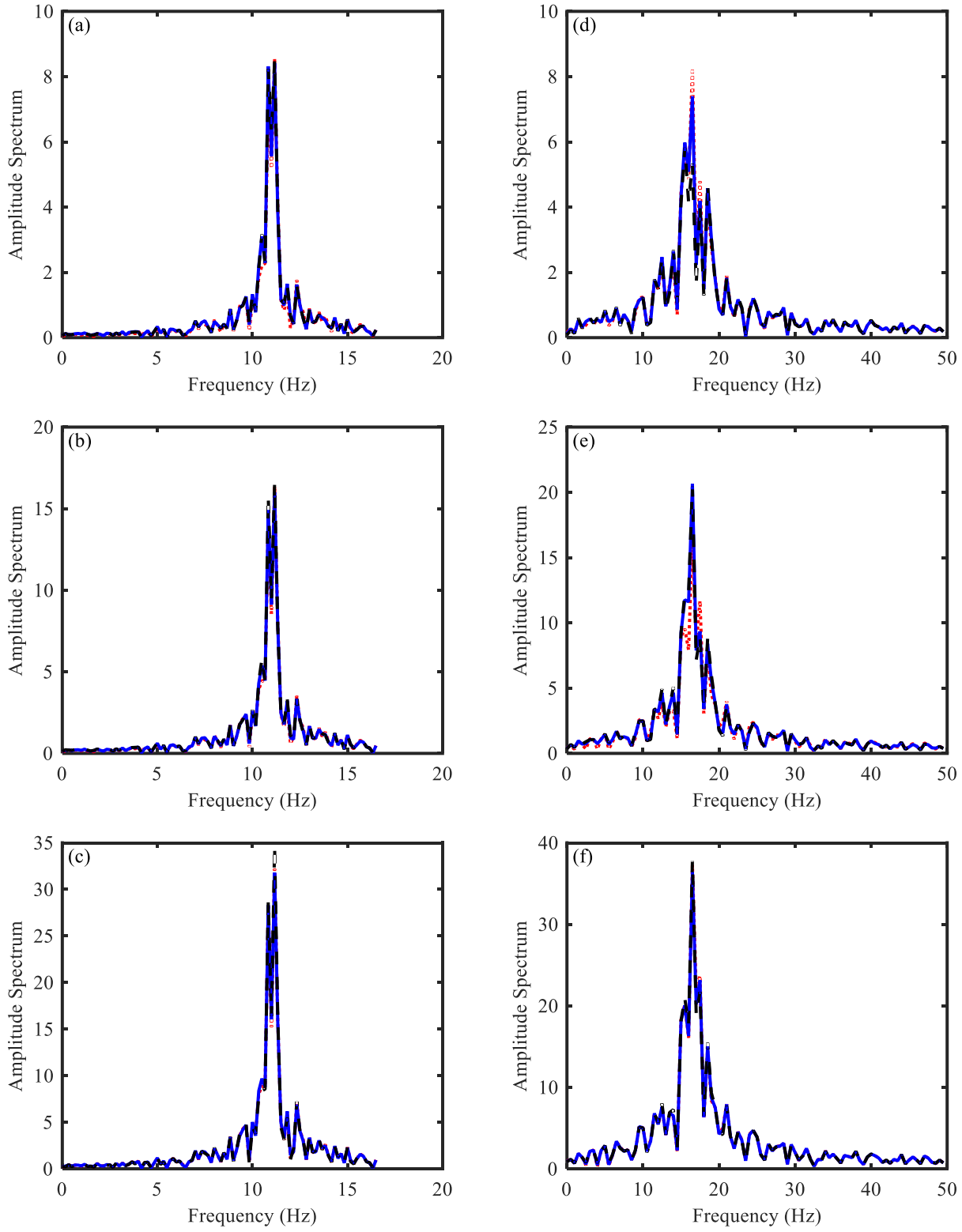

Fig. 4.23. Spectrum analysis of vehicle acceleration (Case 7)
P - 60%; P - 80%; P - 100%.

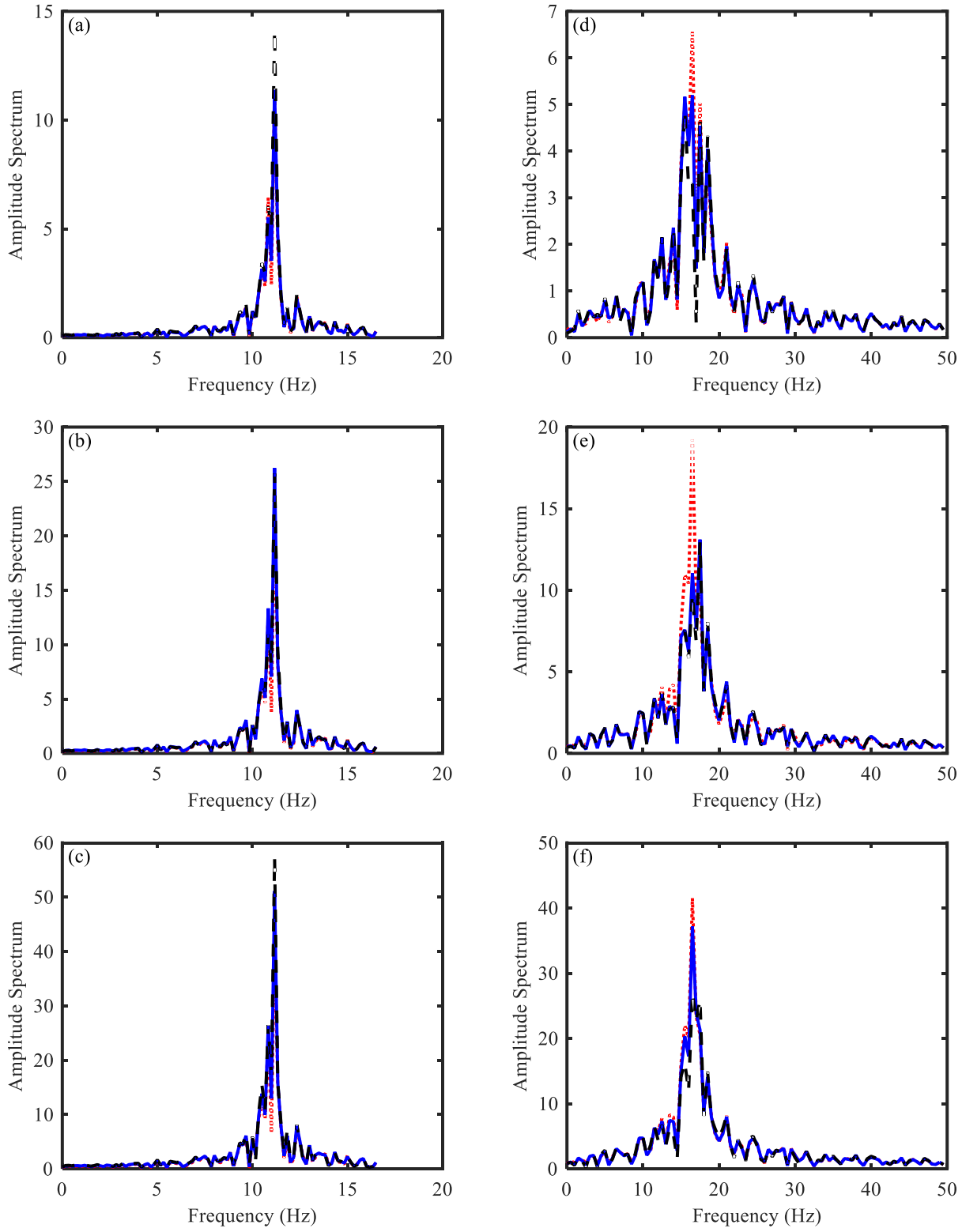

Fig. 4.24. Spectrum analysis of vehicle acceleration (Case 8)
P - 60%; P - 80%; P - 100%.

Table 4.3 summarizes the peaks of amplitude spectrum of vehicle acceleration shown in Figs. 4.17 - 4.24. As can be seen, at the speed of 10 m/s, the corresponding vehicle frequency to the peaks is approximately equal to its natural frequency, however, when the speed increases to 30 m/s, the situation changes and the road surface roughness starts to play an important role.

Table 4.3. Summary of peak values for vehicle acceleration amplitude spectrum

Road surface roughness	Prestress level	Case 1				Case 2			
		10 m/s		30 m/s		10 m/s		30 m/s	
		Hz	Amp	Hz	Amp	Hz	Amp	Hz	Amp
RA	60%	0.33	0.06	1.00	0.04	0.50	0.04	1.00	0.04
	80%	0.33	0.10	1.00	0.07	0.33	0.08	1.00	0.06
	100%	0.33	0.15	1.00	0.09	0.33	0.12	1.00	0.08
RB	60%	0.33	0.04	0.50	0.05	0.50	0.04	0.50	0.04
	80%	0.33	0.09	0.50	0.07	0.33	0.06	0.50	0.06
	100%	0.33	0.13	0.50	0.09	0.33	0.10	0.50	0.08
RC	60%	0.50	0.04	0.50	0.08	0.50	0.05	0.50	0.07
	80%	0.33	0.05	0.50	0.10	0.50	0.04	0.50	0.09
	100%	0.33	0.09	0.50	0.12	0.33	0.06	0.50	0.10
Road surface roughness	Prestress level	Case 3				Case 4			
		10 m/s		30 m/s		10 m/s		30 m/s	
		Hz	Amp	Hz	Amp	Hz	Amp	Hz	Amp
RA	60%	1.17	0.53	1.50	0.49	1.17	0.40	2.00	0.50
	80%	1.17	0.64	1.50	0.88	1.17	0.61	1.50	0.66
	100%	1.17	0.73	1.50	1.24	1.17	0.69	1.50	1.01
RB	60%	1.17	0.79	2.00	0.34	1.17	0.34	2.00	0.48
	80%	1.17	0.90	1.50	0.72	1.17	0.86	2.00	0.50
	100%	1.17	0.99	1.50	1.10	1.17	0.94	1.50	0.85
RC	60%	1.17	1.32	2.00	0.37	1.17	0.79	2.00	0.62
	80%	1.17	1.42	1.50	0.40	1.17	1.35	2.00	0.50
	100%	1.17	1.51	1.50	0.77	1.17	1.44	1.50	0.52

Table 4.3. Summary of peak values for vehicle acceleration amplitude spectrum (Cont.)

Road surface roughness	Prestress level	Case 5				Case 6			
		10 m/s		30 m/s		10 m/s		30 m/s	
		Hz	Amp	Hz	Amp	Hz	Amp	Hz	Amp
RA	60%	3.33	0.68	5.50	4.35	3.00	0.49	7.00	1.49
	80%	3.33	0.79	5.50	5.17	4.17	0.56	6.50	1.70
	100%	3.33	0.78	5.50	5.90	4.17	0.58	6.50	2.17
RB	60%	3.33	1.47	5.50	6.80	3.00	1.09	7.00	2.11
	80%	3.33	1.79	5.50	7.62	3.83	0.94	7.00	2.35
	100%	3.33	2.07	5.50	8.35	3.83	0.89	6.50	2.45
RC	60%	3.33	2.31	5.50	11.70	3.83	2.22	7.00	4.18
	80%	3.33	3.83	5.50	12.55	3.00	2.56	7.00	3.64
	100%	3.33	4.67	5.50	13.28	3.00	1.73	7.00	3.86
Road surface roughness	Prestress level	Case 7				Case 8			
		10 m/s		30 m/s		10 m/s		30 m/s	
		Hz	Amp	Hz	Amp	Hz	Amp	Hz	Amp
RA	60%	11.17	8.54	16.50	8.25	11.17	11.28	16.50	6.58
	80%	11.17	8.41	16.50	7.40	11.17	11.39	16.50	5.20
	100%	11.17	8.48	15.50	5.82	11.17	14.12	15.50	4.86
RB	60%	11.17	16.35	16.50	16.60	11.17	22.03	16.50	19.24
	80%	11.17	16.01	16.50	20.66	11.17	26.24	17.50	13.11
	100%	11.17	16.52	16.50	20.43	11.17	25.73	17.50	12.92
RC	60%	11.17	32.20	16.50	37.27	11.17	43.44	16.50	41.48
	80%	11.17	31.80	16.50	36.45	11.17	51.12	16.50	37.21
	100%	11.17	34.59	16.50	37.81	11.17	57.30	16.50	27.00

Fig. 4.25 shows time histories of the vehicle acceleration traveling on the 100% prestressed bridge for the Case 1, 3, 5 and 8 at the speed of 30 m/s. As shown in Table 4.2, these four cases share the same vehicle mass but different stiffness, possessing a vehicle frequency of 0.32 Hz, 1.01 Hz, 3.18 Hz and 10.07 Hz respectively. It can be observed from Fig. 4.25 that the higher the vehicle frequency, the larger the vehicle acceleration.

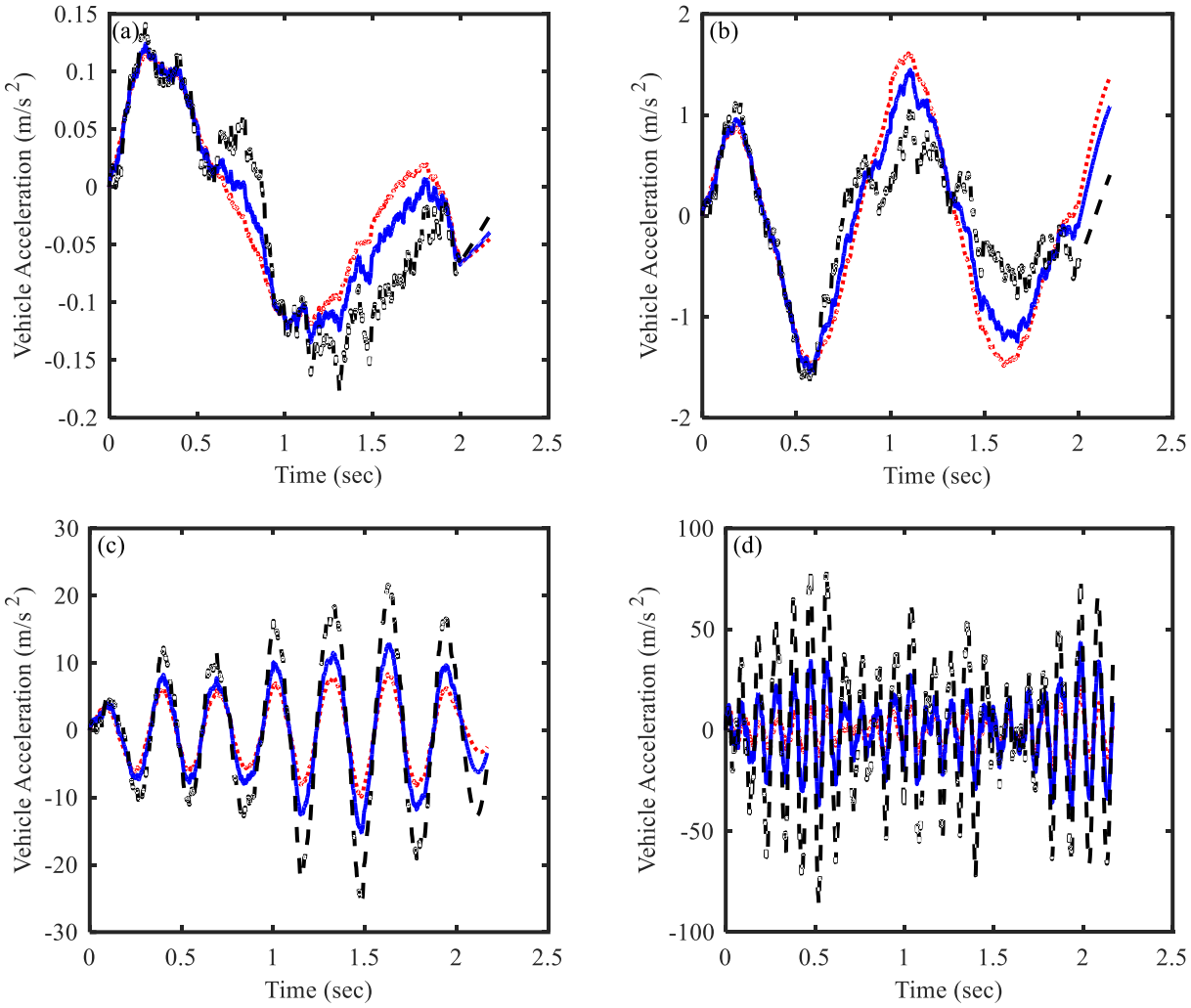

Fig. 4.25. Acceleration of the vehicle under different road surface profiles
(a) Case 1; (b) Case 3; (c) Case 5; (d) Case 8;
Class A; Class B; Class C.

The variation of acceleration due to the road surface roughness also becomes larger and more apparent. At the frequency of 10.07 Hz, the accelerations are dominated by the road roughness effect, which results in the failure of prestress loss identification shown in Fig. 4.23 and Fig. 4.24. At low frequencies, the vehicle acceleration can be more sensitive to the change of prestress force or the initial deflection of the bridge caused by prestress force and gravity load as shown in Fig. 4.26. The lines in Fig. 4.25(a) possess a shape similar to that in Fig. 4.26, indicating at the low frequency of 0.32 Hz, vehicle accelerations are more affected by the bridge

initial deflection as shown in Fig. 4.26 rather than the road surface roughness plotted in Fig. 4.27. Therefore, it is better for a vehicle to possess a low frequency to capture more bridge information instead of road roughness to conduct the prestress loss identification. Also, traveling at low speeds helps the vehicle sense the bridge initial deflection and attenuates the influence from road surface roughness.

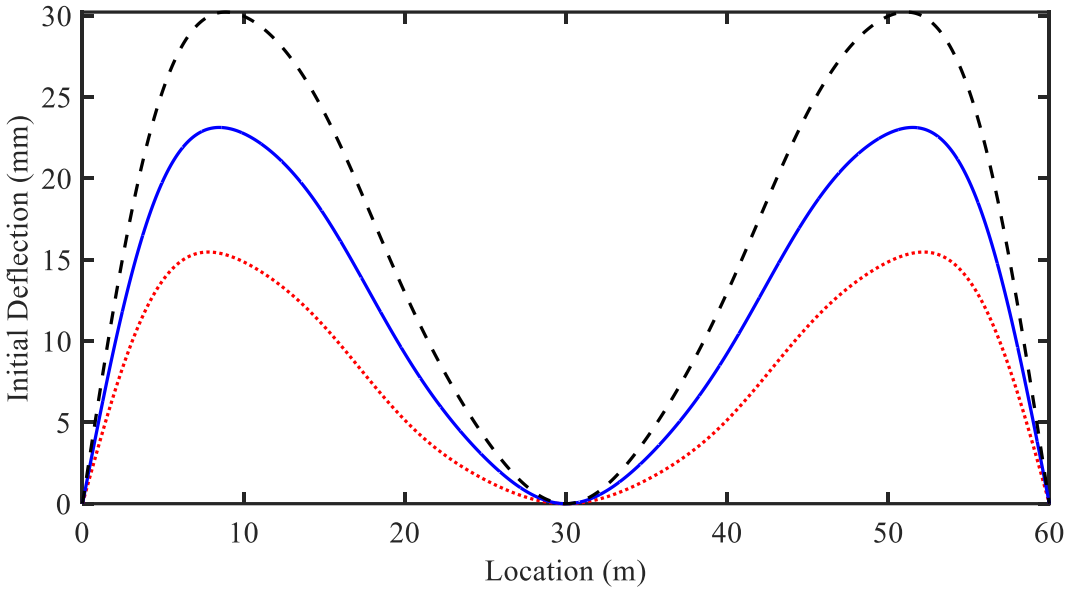

Fig. 4.26. Initial deflection of the bridge under prestress force and gravity load
P - 60%; P - 80%; P - 100%.

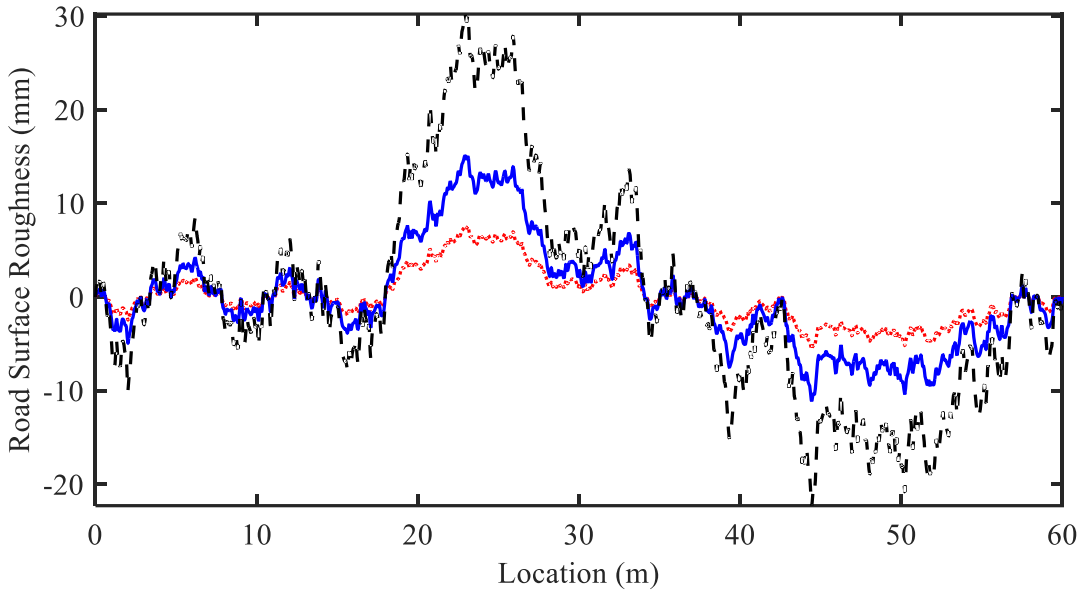

Fig. 4.27. Road surface roughness profiles
Class A; Class B; Class C.

For the vehicle traveling on the prestressed bridge, its vibration can be considered to be subjected to three excitation sources: bridge initial deflection (Fig. 4.26), road surface roughness (Fig. 4.27) and bridge vibration. In some ways, bridge initial deflection can be regarded as a special road surface roughness, which can be predicted or calculated. The first two sources naturally exist no matter whether there are vehicles on the bridge or not, while bridge vibration starts at the time of the vehicle entering the bridge and get affected by the first two sources. These three sources work together to excite the vehicle in a dynamic and time-dependent way when the vehicle is traveling on the bridge.

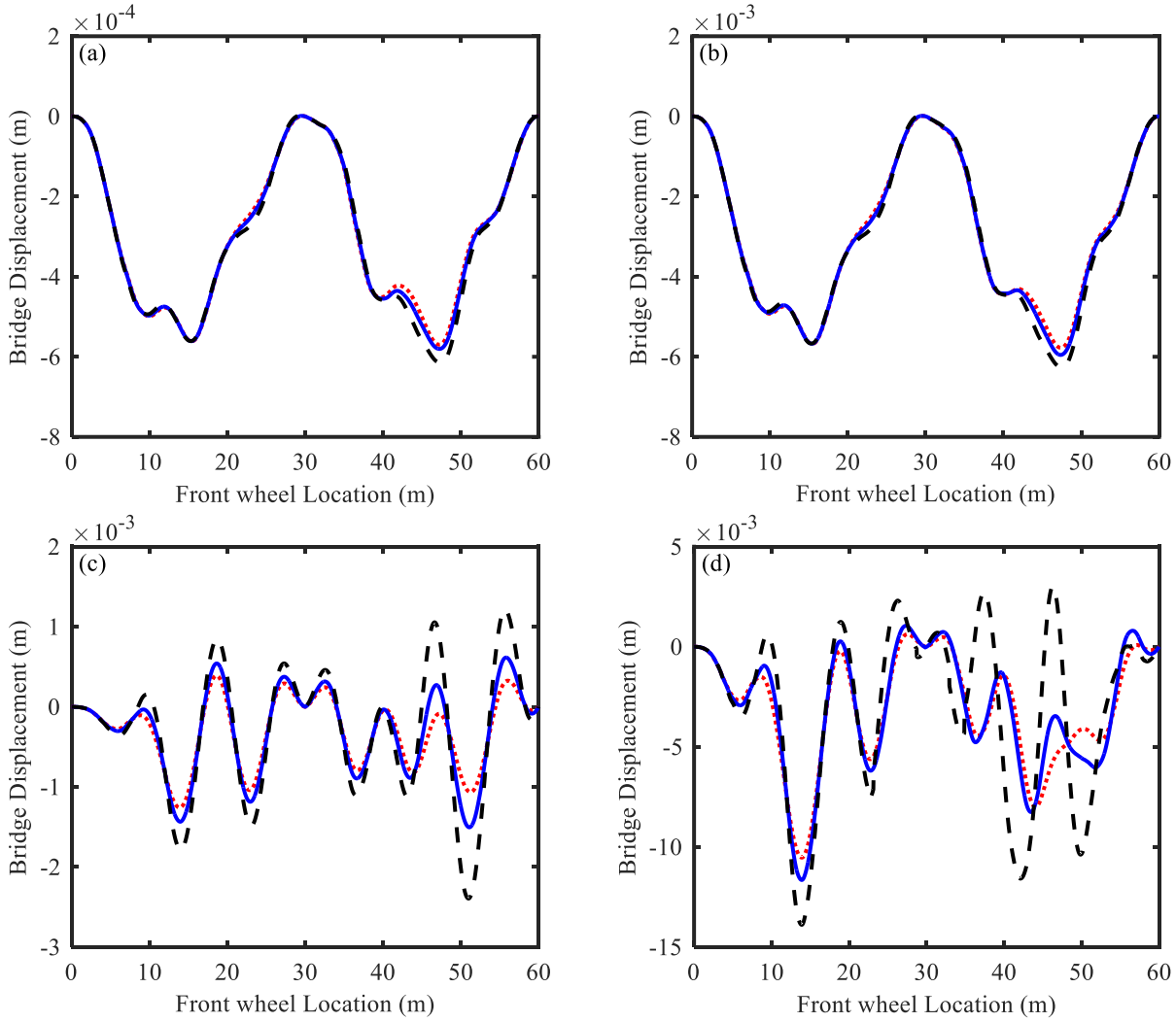

Fig. 4.28. Bridge displacement at the vehicle tire location
(a) Case 3; (b) Case 4; (c) Case 5; (d) Case 6;
Class A; Class B; Class C.

Fig. 4.28 shows the displacement of the 100% prestressed bridge at the vehicle tire location for the Case 3, 4, 5 and 6 for the vehicle speed of 30 m/s. First, the displacements in Fig. 4.28(b) are actually ten times larger than that in Fig. 4.28(a), corresponding to the vehicle mass in Case 4 ten times larger than that in Case 3. Second, for the same vehicle mass, the bridge displacements in Fig. 4.28 (c) and (d) are much larger than that in Fig. 4.28(a) and (b), for which the reason is that vehicle frequency of 3.18 Hz for Case 4 and 5 is very close to the bridge first natural frequency of 3.276 Hz and resonance may be induced. Third, since the bridge

displacements in Fig. 4.28(a) and (c) are relatively small compared with the bridge initial deflection shown in Fig. 4.26, the excitation the vehicle obtains from the bridge vibration is limited so that the bridge prestress loss can be identified as shown in Fig. 4.19 and 4.21. In opposite, the displacements in Fig. 4.28(b) and (d) are so large that the vehicle gets too much excitation from the bridge vibration instead of the bridge initial deflection, which leads to the failure of prestress loss detection as shown in Fig. 4.20 and 4.22. Thus, even with the same frequency, the lighter vehicle will be better in detecting the prestress loss comparing to the heavier vehicles.

4.5. Summary

In the study of this chapter, equation of the motion for the bridge has been modified to take the gravity load into account to get a more accurate initial deflection of the bridge. Also, the effective rigidity of the bridge has been adopted in the research. Both half and quarter vehicle models have been used in the study to investigate the prestress effect and further estimate the prestress loss of the bridge. The following conclusions are reached:

- With the increase of prestress force, the distribution of impact factor along the bridge becomes more unbalanced and higher negative impact factors results at the entrance span of the vehicle;
- With the prestress force, the road surface roughness effect on impact factors becomes insignificant for prestressed bridge;
- Light, low-frequency vehicles moving at low speeds have a better performance in detecting the bridge prestress loss than the heavy, high-frequency vehicles with high speeds.

4.6. References

[1] US Department of Transportation, Federal Highway Administration 2013 Annual Materials Report on New Bridge Construction and Bridge Rehabilitation (2009-2010) National Bridge Inventory (NBI), http://fhwa.dot.gov/bridge/nbi/matreport2011.cfm.

[2] US Department of Transportation, Federal Highway Administration 2013 Material Type of Structure by State National Bridge Inventory (NBI), http://fhwa.dot.gov/bridge/material.cfm.

[3] Ahlborn, T. M., Shield, C. K., & French, C. W. (1997). Full-scale testing of prestressed concrete bridge girders. *Experimental Techniques*, *21*(1), 33-35.

[4] Kim, J. T., Yun, C. B., Ryu, Y. S., & Cho, H. M. (2004). Identification of prestress-loss in PSC beams using modal information. *Structural Engineering and Mechanics*, *17*(3-4), 467-482.

[5] Kim, J. T., Park, J. H., Hong, D. S., Cho, H. M., Na, W. B., & Yi, J. H. (2009). Vibration and impedance monitoring for prestress-loss prediction in PSC girder bridges. *Smart Structures and Systems*, *5*(1), 81-94.

[6] Lu, Z. R., & Law, S. S. (2006). Identification of prestress force from measured structural responses. *Mechanical Systems and Signal Processing*, *20*(8), 2186-2199.

[7] Chen, R. H., & Wissawapaisal, K. (2002). An ultrasonic method for measuring tensile forces in a seven-wire prestressing strand. *Quantitative Nondestructive Evaluation*, *615*(1), 1295-1302.

[8] Beard, M. D., Lowe, M. J. S., & Cawley, P. (2003). Ultrasonic guided waves for inspection of grouted tendons and bolts. *Journal of Materials in Civil Engineering*, *15*(3), 212-218.

[9] Nucera, C., & di Scalea, F. L. (2011). Monitoring load levels in multi-wire strands by nonlinear ultrasonic waves. *Structural Health Monitoring*, *10*(6), 617-629.

[10] Bartoli, I., Salamone, S., Phillips, R., Lanza di Scalea, F., & Sikorsky, C. S. (2011). Use of interwire ultrasonic leakage to quantify loss of prestress in multiwire tendons. *Journal of Engineering Mechanics*, *137*(5), 324-333.

[11] Gao, J., Shi, B., Zhang, W., & Zhu, H. (2006). Monitoring the stress of the post-tensioning cable using fiber optic distributed strain sensor. *Measurement*, *39*(5), 420-428.

[12] Zhou, Z., He, J., Chen, G., & Ou, J. (2009). A smart steel strand for the evaluation of prestress loss distribution in post-tensioned concrete structures. *Journal of Intelligent Material Systems and Structures*, *20*(16), 1901-1912.

[13] Lan, C., Zhou, Z., & Ou, J. (2012). Full-scale prestress loss monitoring of damaged RC structures using distributed optical fiber sensing technology. *Sensors*, *12*(5), 5380-5394.

[14] Lan, C., Zhou, Z., & Ou, J. (2014). Monitoring of structural prestress loss in RC beams by inner distributed Brillouin and fiber Bragg grating sensors on a single optical fiber. *Structural Control and Health Monitoring*, *21*(3), 317-330.

[15] Abdel-Jaber, H., & Glisic, B. (2014). A method for the on-site determination of prestressing forces using long-gauge fiber optic strain sensors. *Smart Materials and Structures*, *23*(7), 075004.

[16] Wang, C., & Cheng, L. (2014). Use of fiber Bragg grating sensors for monitoring concrete structures with prestressed near-surface mounted carbon fiber–reinforced polymer strips. *Journal of Intelligent Material Systems and Structures*, *25*(2), 164-173.

[17] Yang, Y. B., Lin, C. W., & Yau, J. D. (2004). Extracting bridge frequencies from the dynamic response of a passing vehicle. *Journal of Sound and Vibration*, *272*(3), 471-493.

[18] Lin, C. W., & Yang, Y. B. (2005). Use of a passing vehicle to scan the fundamental bridge frequencies: An experimental verification. *Engineering Structures*, *27*(13), 1865-1878.

[19] Yang, Y. B., & Chang, K. C. (2009). Extraction of bridge frequencies from the dynamic response of a passing vehicle enhanced by the EMD technique. *Journal of sound and vibration*, *322*(4), 718-739.

[20] Yang, Y. B., & Chang, K. C. (2009). Extracting the bridge frequencies indirectly from a passing vehicle: Parametric study. *Engineering Structures*, *31*(10), 2448-2459.

[21] González, A., OBrien, E. J., & McGetrick, P. J. (2012). Identification of damping in a bridge using a moving instrumented vehicle. *Journal of Sound and Vibration*, *331*(18), 4115-4131.

[22] Malekjafarian, A., & OBrien, E. J. (2014). Identification of bridge mode shapes using short time frequency domain decomposition of the responses measured in a passing vehicle. *Engineering Structures*, *81*, 386-397.

[23] Saiidi, M., Douglas, B., & Feng, S. (1994). Prestress force effect on vibration frequency of concrete bridges. *Journal of structural Engineering*, *120*(7), 2233-2241.

[24] Zhou, D. (1994). Eigenfrequencies of line supported rectangular plates. *International Journal of Solids and Structures*, *31*(3), 347-358.

[25] International Organization for Standardization (ISO). Mechanical vibration-road surface profiles-reporting of measured data. ISO 8068: 1995 (E), ISO. Geneva, 1995.

[26] Zhu, X. Q., & Law, S. S. (2002). Dynamic load on continuous multi-lane bridge deck from moving vehicles. *Journal of Sound and Vibration*, *251*(4), 697-716.

CHAPTER 5. CONCLUSIONS AND FUTURE WORK

5.1. Conclusions

This study focus on the interaction between vehicles and the bridges subjected to prestress force and foundation settlement. Using modal superposition technique and the principle of virtual works, new bridge-vehicle interaction models have been developed to account for the effects of prestress and foundation settlement. Based on the created models and interaction analysis performed, the following conclusions can be drawn:

- The effect of prestress force on the natural frequencies of the bridge is so tiny that it is impractical to detect the change of prestress through the bridge frequency.
- Single-span bridges are more susceptible to the prestress than multi-span continuous bridges in the form of impact factors and maximum vertical vehicle accelerations.
- Prestress has a significant effect on the maximum vertical acceleration of vehicles, which may provide a good index for detecting the change of prestress.
- Eccentricity is an important component of the prestress in the bridge and the initial moment induced is a controlling factor of the bridge-vehicle interaction response.
- The later-entered vehicle on the prestressed bridge will largely reduce the maximum vertical acceleration of the vehicles ahead of it.
- With the increase of prestress force, the distribution of impact factor along the bridge becomes more unbalanced and higher negative impact factors results at the entrance span of the vehicle.
- Under the influence of prestress force, the road surface roughness effect on impact factors becomes insignificant for prestressed bridge.

- Foundation settlement may have adverse or beneficial effects on impact factors of different span of the bridge, depending on the settlement mode.
- Vehicle responses are more vulnerable to the settlement that may result in a poor riding quality.
- The effect of foundation settlement on impact factors increases with the vehicle speed and becomes significant at the high speeds.
- Road surface roughness has considerable effect on the impact factors and may couple with the settlement to aggregate the overall effect.
- Impact factors of simply-supported bridges are more susceptible to the foundation settlement.
- Light, low-frequency vehicles moving at low speeds have a better performance in detecting the bridge prestress loss than the heavy, high-frequency vehicles with high speeds.

5.2. Future Work

Further research is necessary in order to improve the developed model and experimental tests are needed to validate the proposed drive-by prestress loss identification method. Some suggestions for future study are discussed below.

- To study the difference between pre-tensioned and post-tensioned concrete bridges subjected to vehicular loading, prestress loss and foundation settlement;
- To investigate the effect of non-straight prestress tendon profile in the concrete on bridge vehicle interaction;
- To extend the proposed bridge vehicle interaction model into three dimensions to consider more complex prestress loss and foundation settlement cases;

- To analyze the combined effect of approach span faulting and support settlement on dynamic bridge and vehicle responses;
- To conduct further optimization of vehicle parameters and experimental validation of drive-by prestress loss identification.